Dissertation

zur Erlangung des Grades des
Doktors der Naturwissenschaften
der Naturwissenschaftlich-Technischen Fakultät der

Universität des Saarlandes

Shortcuts to Quantum Advantage in the NISQ Era

Saarbrücken, 2024

Gino Bishop

Tag des Kolloquiums:	16.05.2025
Dekan:	Prof. Dr.-Ing. Dirk Bähre
Berichterstatter:	Prof. Dr. Frank K. Wilhelm-Mauch Prof. Dr. Vivien Kendon Prof. Dr. Peter Orth
Akademisches Mitglied:	Dr. habil. Philipp Hövel
Vorsitz:	Prof. Dr. Giovanna Morigi

Abstract

Quantum computing holds the promise of addressing some particularly difficult problems that are out of reach for classical computers, such as simulating many interacting quantum particles. Instead of laboriously calculating the evolution of each particle, quantum computers turn the problem itself into the computational system, allowing qubit dynamics to mirror particle interactions. Calculating electron correlations through the Green's function, which demands exponential classical memory, becomes feasible in reasonable time with a novel quantum algorithm based on linear response theory. This method, with two-qubit gate scaling akin to the Hadamard test, goes beyond traditional mappings like Jordan-Wigner, proving powerful for two-dimensional systems burdened by long Pauli strings. We also contextualize its application to the exploration of the phase diagram of correlated electrons.

Another challenging area is combinatorial optimization, for which some problems are representable in terms of Ising problems. The ground state spin configuration to the Ising problem can be found via quantum annealing for which the minimum energy gap between the lowest energy states limits the evolution rate. Our approach optimizes annealing schedules to accelerate solution times for arbitrary Ising problems that can be mapped to the Lechner-Hauke-Zoller architecture. We achieve an average speed-up by a factor of $\sim$3.5 in reaching a ground state fidelity of 90%.

Zusammenfassung

Quantencomputing verspricht, einige der Probleme zu lösen, die aufgrund von begrenztem Rechenspeicher für klassische Computer unzugänglich sind. Ein Beispiel ist die Simulation vieler wechselwirkender Quantenteilchen. Anstatt aufwendig die Evolution einzelner Teilchen zu berechnen, werden diese in Form von Qubits Bestandteil des Rechensystems; die Interaktionen zwischen den Teilchen werden durch die Dynamik der Qubits nachgebildet. Die Berechnung von Elektronenkorrelationen über die Green'sche Funktion wird durch einen neuartigen Quantenalgorithmus auf Basis linearer Antwortfunktionen möglich. Unser Verfahren skaliert vergleichbar mit dem Hadamard-Test in Bezug auf Zwei-Qubit Gatter und kann adaptiert werden für zweidimensionale Systeme, für welche nicht-lokale Transformationen über Jordan-Wigner hinaus vorteilhaft sind. Zudem stellen wir den Einsatz des Algorithmus in den Kontext der Ermittlung des Phasendiagramms korrelierter Elektronen.

Ein weiteres anspruchsvolles Gebiet sind kombinatorische Optimierungsprobleme, die als Ising-Probleme formuliert werden können. Die Grundzustandskonfiguration solcher Systeme kann mittels Quanten-Annealing gefunden werden, wobei die minimale Energiedifferenz zwischen den niedrigsten Energiezuständen die Evolutionsgeschwindigkeit begrenzt. Unser Ansatz optimiert den Treiber zur Beschleunigung von Annealing Zeiten für beliebige Ising-Probleme, welche in der Lechner-Hauke-Zoller Architektur abgebildet werden können. Die Zeit, die man benötigt um mit einer Wahrscheinlichkeit von 90% den Grundzustand zu finden, wird durchschnittlich um den Faktor ~3.5 reduziert.

List of Publications

Formulations, figures and equations will be replicated in all parts and chapters.

Quantum algorithm for Green's-function measurements in the Fermi-Hubbard model
Gino Bishop, Dmitry Bagrets, Frank K. Wilhelm
Phys. Rev. A **111**, 062610 — Published June 9th, 2025
Appears here as Part I.

A Set of Annealing Protocols for Optimized System Dynamics and Classification of Fully Connected Spin Glass Problems
Gino Bishop, Simone Montangero, Frank K. Wilhelm
Independent extension to the Master's thesis
arXiv:2310.10442 — Submitted on October 16th, 2023
Appears here as Part II.

Acknowledgements

In appreciation of the generous support from Mercedes-Benz AG, I am grateful for the funding, resources and network of expertise, that contributed to the development of this thesis. For the years at Mercedes-Benz AG, I would like to thank my former supervisor Dr. Martin Frey, who took me under his wings in times of turbulences. Likewise, Dr. Ernst Richter and Dr. Markus Leder treated me with friendly collegiality, easing the path for corporate inclusion.

I thank my supervisor Prof. Frank Wilhelm-Mauch for the benevolence and can-do attitude towards his students. Throughout the time of the dissertation, I felt a great sense of autonomy and ownership.

Additionally, I would like to acknowledge Dr. Dmitry Bagrets, a respected and knowledgable asset in our group. His input was essential to the quality of this work.

Furthermore, I like to mention Dr. David Headley, Dr. Thorge Müller, Clemens Possel and Aditya Kela. They have supported the progress of this work in various ways.

Table of Contents

Preface

Part I: Simulation of correlated electrons

Synthesis

List of Figures

List of Tables

Glossary of Acronyms

FHM Fermi-Hubbard model

GCP grand canonical potential

GF Green's function

JW Jordan-Wigner

LHZ Lechner-Hauke-Zoller

NISQ noisy intermediate-scale quantum

VCA variational cluster approach

VHA variational Hamiltonian ansatz

Preface

Quantum Computing in the NISQ era

If we were able to harness quantum computers effectively, they hold the promise of solving some classically intractable problems efficiently. Traditionally, information is stored in bits, which represent one of two possible states, 0 and 1. In contrast, quantum computers are based on the principles of quantum mechanics, operating beyond binary logic.

The building block of quantum computers is the qubit, acting as the quantum analogue to the classical bit. Until measured, qubits remain in a superposition of states 0 and 1, which is one of the mechanism contributing to massive speed-ups in computation. The state space in which qubits exist, the Hilbert space, is of dimension 2^n for n qubits. From a classical perspective, this signifies a doubling in memory for each additional qubit. By design, an n-qubit register can represent a superposition over all 2^n classical bit strings. This is important when it comes to encoding entangled states. Entanglement is an intrinsic feature of quantum systems and necessary for quantum speed-ups over classical algorithms. In first approximation, entanglement implies the dependence of one qubit state onto another qubit state, creating a correlation between them.

Entangled states cannot be expressed as products of individual states. For such product states, the memory requirement scales linearly with the number of qubits, e. g., $2n$ complex numbers can represent the product state of n qubits. However, accounting for entangled states typically means that we need to classically store all 2^n complex numbers. By construction, the number of required qubits remains the same. Here, quantum computers demonstrate a key advantage over classical computers. Superposition enables a quantum state to represent a coherent linear combination of configurations, where each configuration is associated with a complex probability amplitude. Any operation on that quantum state affects all probability amplitudes. If that quantum state is also entangled, then those operations can be used to exploit correlations between subsystems and enable constructive or destructive interference between probability amplitudes. While constructive interference leads to desired configurations becoming more probable as solutions to a problem, destructive interference suppresses unwanted solutions.

This comes in handy especially if we were to simulate correlated quantum states, as can be found in many-body systems. Electrons typically repel each other, which makes a quantitative description of many electrons interacting with each other cumbersome. Quantum computers can mimic the behavior of such systems in a natural way without the need to employ an exponential amount of computational resources. Advanced materials rely on the investigation, understanding and utilization of such systems. Engineering high-temperature superconducting materials is to this day an aspirational goal, which could lead to many useful applications. Even better if we were able to deliberately turn on and off such features within the same material, enabling a switch from superconducting to Mott-insulating phases (a material that behaves as an insulator due to strong electron-electron interactions, even though classical band theory would predict it to be conducting), and vice versa.

For such correlated systems, the Green's function (GF) [1] plays a significant role. It can be seen as the propagator for many-body systems, containing information on correlations and quasi-particle excitations such as Cooper pairing. Thus, at the starting point of many-body studies involving complex particle interplays leading to exotic phases, evaluating the GF is paramount. We show how to accurately evaluate the GF for small cluster systems on a quantum computer, and how to extrapolate the results to larger systems. Put differently, we showcase how many-body systems can be solved with a relatively small quantum chip.

In a different context, the superposition principle together with the ability of quantum particles to tunnel through thin barriers can be leveraged. Some combinatorial optimization problems [2] can potentially benefit from these quantum features as they can be addressed by mapping them onto physical Ising models. The solution to these problems is the ground state configuration of spins. The configuration space maps a given configuration of spins onto an energy landscape. Depending on the problem to solve, these landscapes can take on arbitrary forms and classical optimization algorithms, such as Monte-Carlo algorithms, can get stuck in local minima.

Quantum annealing, yet a different form of quantum computation, enables a system to escape such local minima. On the one hand, the superposition of configurations leads to an effective parallel scouting for the optimal solution, for which energetically lower configurations will be favored. On the other hand, the global state can tunnel through energy barriers, that separate local minima. To this day, it is still an open question as to whether or not quantum annealing can efficiently solve combinatorial optimization problems. If it does, however, it will be attributed to these two features.

The landmark paper on quantum supremacy [3] has sparked great interest in the research field of quantum computation, which has now advanced to a playground for sophisticated hardware and algorithms. Before we get too excited, we need to acknowledge that currently we exist in what is called the noisy intermediate-scale quantum (NISQ) era [4], implying error prone machines. There are a handful of physical implementations of qubits; each comes with its advantages and disadvantages. A large portion of today's research evolves around superconducting qubits [5], e. g., how to make them more robust against any disturbance from the outside world. There are many endeavors to dampen the impact of imperfect machines, both on hardware and software fronts.

This thesis puts emphasis on quantum algorithms, while acknowledging hardware constraints. To that end, we explore shortcuts to quantum advantage, that can be achieved today. Academically, quantum advantage refers to the idea of solving classically intractable problems in a reasonable time with quantum hardware. Although first demonstrations towards quantum advantage were presented, a generalization to a broader range of problems is still an aspirational goal of the research community. Shortcuts to quantum advantage leverage existing, physically motivated techniques. Abstract problems are mapped to physical quantum systems that can evolve, be controlled and measured. Thus, classical calculations gradually shift towards an assisting function such as stabilizing measurement outcomes or updating variational parameters.

0 Elements of quantum computation

The reader is provided with a repository of concepts, which are fundamental to the development of this work.

0.1 Quantum Bits

Quantum computers do not work with bits, but their quantum counterpart: the qubit. While bits take on only the binary values 0 and 1, a qubit, which is a shorthand notation for quantum bit, is a construct with assigned probability amplitudes to the computational basis states $|0\rangle$ and $|1\rangle$. In theory, these amplitudes stay alive as long as the qubit is not measured. This turns out to be a huge advantage as it is possible to store working memory of the largest supercomputers today in a quantum chip consisting of merely a couple dozen qubits. Mathematically, a state of a qubit $|\Phi\rangle$ is defined via

$$|\Psi\rangle = \alpha|0\rangle + \beta|1\rangle = \begin{pmatrix}\alpha\\ \beta\end{pmatrix}. \tag{0.1}$$

Here, α and β are probability amplitudes associated with the states $|0\rangle$ and $|1\rangle$, respectively. By virtue of being probability amplitudes, their squared values must add up to one, i. e., $|\alpha|^2+|\beta|^2= 1$.

An alternative way of representing the state of a qubit is via the density matrix $\hat{\rho}$. In its most general form, the density matrix is defined as

$$\hat{\rho} = \sum_i p_i |\Psi_i\rangle\langle\Psi_i|, \tag{0.2}$$

where p_i denote the weights of distinct quantum states $|\Psi_i\rangle$. While a system that cannot be reduced to a single projector is called a mixed state, a pure state consists only of a single quantum state, collapsing the sum to $\hat{\rho} = |\Psi_i\rangle\langle\Psi_i|$. Hence, tracing over the squared density matrix in a pure state gives one, whereas if the state is mixed, then the trace is smaller than one. We can make use of the Bloch sphere representation, Fig. 0.1, $|\Psi\rangle = \cos\left(\frac{\theta}{2}\right)|0\rangle + e^{-i\Phi}\sin\left(\frac{\theta}{2}\right)|1\rangle$ with angles $\theta \in [0, \pi], \Phi \in [0, 2\pi)$ being the latitude and longitude on the sphere, respectively. A qubit in equal superposition is achieved for $\theta = \pi/2$ (or likewise $\theta = 3\pi/2$), i. e.,

$$|\Psi\rangle = (|0\rangle + e^{-i\Phi}|1\rangle)/\sqrt{2}, \tag{0.3}$$

where we call Φ the relative phase between the basis states. Although not an observable in the traditional sense (it cannot be measured directly, but it has measurable effects on

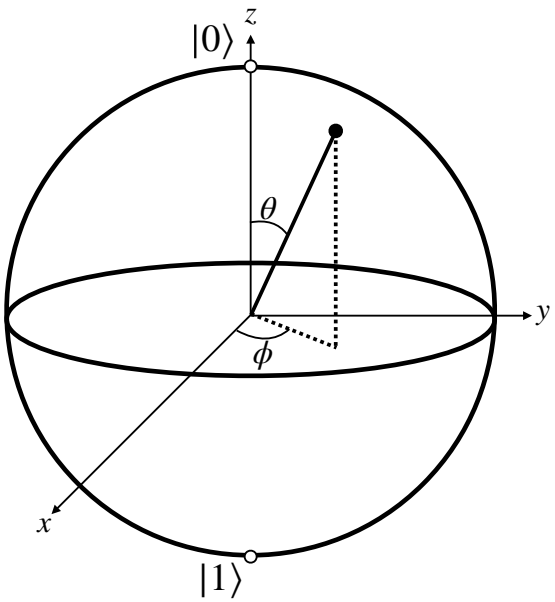

Figure 0.1: The Bloch sphere represents the state space of a single qubit. The angles θ and Φ fully describe a pure quantum state. Mixed states are points inside the sphere.

interference phenomena), this phase is key to exploiting interference and superposition in quantum demonstrations. Operations on qubits then correspond to rotations of that sphere with respect to θ and Φ. Pure quantum states correspond to a point on the surface of the sphere. Mixed states however are points inside the sphere.

Transformation of such states is possible via unitary operations $\hat{U}$. These are 2×2 matrices with $\hat{U}^\dagger \hat{U} = \hat{U}\hat{U}^\dagger = \mathbb{I}$ that preserve the norm of a quantum state. For instance, the dynamics of a quantum system are governed by the time-dependent Schrödinger equation

$$i\hbar \frac{\mathrm{d}}{\mathrm{d}t} |\Psi(t)\rangle = H|\Psi(t)\rangle, \tag{0.4}$$

where $\hat{H}$ is called the Hamiltonian, representing the energy of the system, and $\hbar$ is the reduced Planck's constant. The solution to the time-dependent Schrödinger equation is the the time-evolution operator, which evolves a quantum system from time t' to time t is given by

$$\hat{U}(t, t') = e^{-\frac{i}{\hbar} H(t-t')}, \tag{0.5}$$

i. e., $\hat{U}|\Psi(t')\rangle = |\Psi(t)\rangle$. For a system with a time-independent Hamiltonian (implying energy conservation), the time-dependent Schrödinger equation admits separable solutions whose spatial part satisfies the time-independent Schrödinger equation

$$\hat{H}|\Psi\rangle = E|\Psi\rangle. \tag{0.6}$$

The time-independent Schrödinger equation is hence an eigenvalue equation, where $|\Psi\rangle$ is an eigenstate to the Hamilton operator $\hat{H}$, for which the eigenvalue is the energy E. The lowest energy eigenvalue is called the ground state energy, and the corresponding eigenstate

is called the ground state. The eigenstate with the next highest energy is called the first excited state. Many problems for which quantum computers are employed seek the ground state configuration of a quantum system, for which classical diagonalization is not feasible in reasonable time due to the size of the system and thereby due to classical memory limitations.

0.2 Quantum processing units and emulators

The system in which qubits live is the quantum processing unit (QPU). We face major challenges in the engineering thereof [6]. For instance, even slight mistakes in the production process can render a superconducting quantum chip useless. One of the metrics that is steadily increased is the number of qubits on a chip. More qubits mean more computational power, but they come with their own set of challenges, too. Given the limited space of quantum chips, crosstalk [7], i. e., the unwanted interaction between qubits due to close proximity amongst each other, is one of the challenges that need to be considered. Another challenge is the engineering of connection lines between the qubits. Clever ways of arranging qubits into a qubit layout are needed to address these challenges. Likewise, given a qubit layout, quantum algorithms need to be adjusted such that they target qubits that resemble high connectivity and low error rates.

Maintaining quantum computers is high effort, and that is why a reasonable testbed for algorithms are quantum emulators. As the name suggests, a quantum chip is emulated by classical hardware and is then used to demonstrate what could be expected, if a problem was to be solved on actual quantum hardware. On the other hand, quantum simulators physically mimic a quantum device in terms of qubit layout, interconnectivity, error rates for certain operations, execution time of those operations and lastly coherence times. While emulators are often implemented on CPUs, simulators are mainly implemented as QPUs.

To that end, simulators come with specifications, that gives the user an idea of the types of algorithms, that can be run on a quantum computer. The most prominent ones are gate errors as well as T_1 and T_2 times, referred to as the relaxation time and dephasing time, respectively. While T_1 indicates how long it takes the qubit to return to thermal equilibrium with the environment, T_2 gives an upper limit on how long a qubit can remain coherent, i. e., how long the state of a qubit can be described by the time-dependent Schrödinger equation. Not to forget the execution time of given gates, which in accumulation shall stay well below T_2 to guarantee for coherent calculations.

0.3 Gate-based quantum computation

In order to perform calculations on quantum hardware, one needs to perform operations on qubits. One way to perform such operations is in form of quantum gates. The latter are capable of rotating qubits in the Bloch sphere, Fig. 0.1, altering their states. Quantum algorithms can be described by a sequence of quantum gates acting on qubits. These gates

are different in their implementation, purpose, execution speed and accuracy. Often, one can combine several basic gates into more complicated gates, that serve very specific tasks. Depending on the technical nature of the quantum computation platform, a realization of quantum gates can take different forms. For instance, if we were to look at superconducting qubits, then carefully designed microwave pulses are responsible for qubit rotations.

0.3.1 Elementary gate operations and universal quantum computation

Universal quantum computing is the ability to approximate any unitary transformation to arbitrary precision using a finite set of natively available quantum gates. Information is manipulated via operations in form of qubit rotations. In a gate based quantum computing approach, the sequence of operations applied to a register of qubits is called a quantum circuit. The register itself can be understood as the computation platform, as it encompasses all the qubits drafted for the execution of a given task. Many gates target only one qubit. We call them single-qubit gates. Such gates typically have a short execution time and generate fewer errors per operation, than multi-qubit gates. These gates target two or more qubits simultaneously and thereby are capable of generating entanglement. Multi-qubit gates take significantly longer execution time, and the errors dominate over single-qubit operation errors. As such, it is more often than not advisable to reduce the number of multi-qubit operations to improve the quality of results.

0.3.2 Jordan-Wigner mapping and Majorana fermions

Assume we wish to investigate fermion systems, say a group of electrons in a confined region. Not only do electrons repel each other. By virtue of being fermions, they obey to the Pauli exclusion principle; it states that no two fermions can occupy the same quantum state in a given quantum system at the same time. Hence, we need to find a way to map the physics of such particles onto the computational elements, the qubits, such that synchronized qubits behave as if they were fermions. Pauli exclusion or repulsion is encoded in the states of the qubits, which can be read out to extract the fermionic properties one wishes to study.

For the study of time-dependent correlators, fermionic operators can be represented by Hermitian Majorana operators. The latter obey to the anti-commutation relations (see Eqs. (0.7) and (0.8) below) as well and can be subject to the Jordan-Wigner (JW) transformation.

0.3.2.1 Jordan-Wigner mapping

The JW mapping [8] is the simplest, straight forward mapping from fermionic operators to qubit operators, imposing fermionic behavior onto how qubits react to specific operations. For instance, the wave function associated with two fermions changes its sign, if two fermions are being exchanged, cf. Eq. (0.7). Moreover, two fermions are not allowed to occupy the same quantum state simultaneously, known as the Pauli exclusion principle,

cf. Eq. (0.8). Consequently, qubit algebra obeys to the anti-commutation relations. The mathematical formulation of stated fermion behavior reads

$$\{c_i, c_j^\dagger\} = c_i c_j^\dagger + c_j^\dagger c_i = \delta_{ij}, \tag{0.7}$$

and

$$\begin{aligned} \{c_i, c_j\} &= c_i c_j + c_j c_i = 0, \\ \{c_i^\dagger, c_j^\dagger\} &= c_i^\dagger c_j^\dagger + c_j^\dagger c_i^\dagger = 0, \end{aligned} \tag{0.8}$$

where $c_i, c_i^\dagger$ are the fermionic annihilation and creation operators, respectively. The JW mapping is one of the simplest ways to map fermionic creation and annihilation operators onto Pauli matrices, that satisfy the above anti-commutation relations Eqs. (0.7) and (0.8). This transformation is achieved via

$$\begin{aligned} c_i &= \Big(\prod_{k=1}^{i-1} \sigma_k^z\Big)\sigma_i^-, \\ c_i^\dagger &= \Big(\prod_{k=1}^{i-1} \sigma_k^z\Big)\sigma_i^+, \end{aligned} \tag{0.9}$$

where $\sigma_i^- = (\sigma_i^x - i\sigma_i^y)/2$ is the spin-lowering operator and $\sigma_i^+ = (\sigma_i^x + i\sigma_i^y)/2$ is the spin-raising operator. The string of σ^z matrices acts on qubits with index $k = 1, 2, \cdots, j-1$, i. e., on all qubits that come before the target qubit j.

0.3.2.2 Majorana fermions

Majorana fermions are distinctive fermions as they are their own anti-particles. They can be written as $x_{i\sigma} = c_{i\sigma} + c_{i\sigma}^\dagger$ and $y_{i\sigma} = i(c_{i\sigma} - c_{i\sigma}^\dagger)$. In topological quantum computers, two spatially separated Majorana fermions combine to a highly robust qubit.

Importantly, single Majorana operators are, in stark contrast to single fermion operators, Hermitian. Per definition, they square to identity $x_{i\sigma}^2 = 1$, which implies that they are their own inverses and consequently unitary. This renders them suitable for an evaluation of correlators of the form $\langle c_i^{(\dagger)}(\tau > 0) c_j^{(\dagger)}(\tau = 0)\rangle$. Thereby, they are a powerful tool to study correlated systems on gate based quantum computing platforms.

0.4 Applied Quantum Error Mitigation

As long as quantum computers remain prone to errors, we need routes how to increase the quality of results. To that end, we distinguish between error mitigation and error correction. Error mitigation [9] effectively decreases the noise stemming from quantum machines; error correction [10] removes that noise up to small, yet non-zero error target at the expense of a

large qubit overhead. As of today, error correction remains an engineering challenge, albeit recent works [11] showcase significant progress on the road towards error corrected qubits. Here, we will put our focus on error mitigation schemes, which are relatively simple to implement and harness. Specifically, we will outline four techniques, that will reappear in this thesis later on, as they were utilized to raise the fidelity of our computations.

0.4.1 Dynamical decoupling

Dynamical decoupling (DD) is a quantum control technique employed to mitigate decoherence, particularly on idle qubits during quantum computations. The core idea behind DD is to suppress the effects of slow, quasi-static noise that typically arise from low-frequency environmental fluctuations by systematically decoupling the qubit from its environment through carefully timed control pulses.

In practice, DD involves applying sequences of Pauli gates, such as repeated applications of X, Z, or combinations like $XYXY$, to idle qubits. These sequences are engineered so that the net effect of environmental interactions, particularly those that induce phase-flip (dephasing) or bit-flip errors, averages out over time. The choice of gate types and the structure of the sequence depend on the dominant noise sources and the spectral characteristics of the environment. In essence, DD restores coherence by enforcing a controlled evolution that aligns with the unitary dynamics prescribed by the Schrödinger equation, thereby counteracting unwanted environmental perturbations.

0.4.2 Zero-noise extrapolation

Zero-noise extrapolation (ZNE) [12] is a noise mitigation technique that embraces inherent noisiness by systemically amplifying the noise in a quantum circuit, thereby enabling a systematic extrapolation to the zero-noise limit. The standard approach to ZNE involves augmenting the circuit with additional noisy operations, typically by inserting redundant two-qubit gates such as controlled-NOT (CNOT) or controlled-Z (CZ) gates. These gates function by flipping (CNOT) or entangling (CZ) the target qubit conditional on the control qubit being in the $|1\rangle$ state. From this point forward, we refer to these simply as CNOT or CZ gates, respectively.

Importantly, applying a pair of consecutive CNOT gates on the same qubits theoretically implements the identity operation, leaving the quantum state unchanged. However, in practice, each physical gate introduces some level of noise. ZNE leverages this by deliberately introducing such redundant gates to scale the overall noise level in the circuit by a factor f. For instance, an extrapolation factor of $f = 3$ corresponds to replacing each CNOT with three sequential CNOTs. Typical values used in experiments include $f = 1$ (no noise amplification), $f = 3$, and $f = 5$. After executing the circuit at various noise amplification levels, one can perform an extrapolation (commonly linear, polynomial, or exponential depending on the circuit's depth) to estimate the observable of interest in the ideal zero-noise limit.

Shallow circuits often admit accurate linear extrapolations, whereas deeper circuits require higher-order fitting models due to the compounded effects of noise.

0.4.3 Pauli twirling

Pauli twirling is a technique used in quantum error mitigation to approximate an arbitrary noise channel by a stochastic Pauli channel, simplifying modeling and error mitigation.

The implementation involves inserting randomly chosen Pauli gates before and after two-qubit Clifford gates (typically CNOT or CZ gates) as follows. For a given two-qubit gate U, one applies a gate sequence of the form $P_1 \otimes P_2 \cdot U \cdot P_1' \otimes P_2'$, where the Pauli gates P_i, P_i' are selected such that the overall transformation is equivalent to U. This preserves the logical action of the quantum circuit while randomizing coherent error contributions. This randomized gate dressing is performed across an ensemble of equivalent quantum circuits: each of them is structurally distinct in terms of gate composition, but operationally identical in the ideal, noiseless setting. Measurements from these randomized circuits are then averaged to produce a final result.

0.4.4 Measurement error mitigation

Readout error mitigation aims to reduce errors in measurements of bit strings. In its standard form, one prepares the computational states of a given system size and measures the frequency of associated bit strings. Looking at just one qubit for demonstration purposes, we write the conditional probabilities into a calibration matrix M of the form

$$M = \begin{pmatrix} P(0|0) & P(0|1) \\ P(1|0) & P(1|1) \end{pmatrix}. \tag{0.10}$$

The elements $P(m|n)$, with $m, n \in \{0, 1\}$, are the probabilities of measuring the qubit in state m, if we have prepared the qubit in state n. This matrix is then inverted and applied to the experimental readout results.

0.5 Quantum annealing

Quantum annealing [13–16] is a technique used for finding a target eigenstate of a given Hamiltonian. In the context of quantum computing, combinatorial problems (prominent examples are the traveling salesman problem [17] and the maximum cut problem [18]) can be cast into the form of a transverse-field Ising model [19], where the goal is to find the minimum energy configuration of spins. There is no known classical polynomial-time algorithm that can solve either the maximum cut or the traveling salesman problem.

0.5.1 Combinatorial optimization problems

Combinatorial optimization is an area of mathematics that seeks to find an optimal solution from the set of possible solutions. The optimal solution is such that it minimizes a given objective function associated with a given problem. This is done by introducing optimization parameters, that are updated according to a metric representing the goodness of the corresponding solution. One famous example is that of the traveling salesman, who needs to travel to different locations efficiently, i. e., seeks the shortest path possible to visit N cities exactly once and end up at the starting city. The stated problem belongs to the complexity class NP-hard; its decision variant belongs to NP-complete. Similar to the quantum mechanical Hilbert space, which doubles with the introduction with each successive spin, any additional vertex representing a city increases the number of possible solutions. For the traveling salesman problem, the number of possible ways is $(N-1)!$. Those types of problems can be cast into the form of a transverse-field Ising model. In its general form, such a problem reads

$$H = -\sum_{\langle i,j \rangle} J_{i,j}\sigma_i^z\sigma_j^z - \sum_i h_i\sigma_i^x, \tag{0.11}$$

for which the first part corresponds to the Ising term, with the interaction matrix J representing the coupling between spins, and the second with h_i being local fields acting on spin i is the transverse-field term, enabling spin flips. The original combinatorial optimization problem is encoded in the couplings between spins, such that the best solution is the lowest energy eigenstate to the Ising term. One way to solve such problems is quantum annealing, a method that uses quantum mechanics to explore the solution space of combinatorial optimization problems by exploiting superposition and quantum tunneling. Going full circle, when the optimal solution is finally found, it is mapped back to the solution to the original, combinatorial optimization problem.

0.5.2 Adiabatic quantum annealing

In quantum annealing, the transverse-field Ising model defines a time-dependent Hamiltonian that interpolates between a transverse-field driver and a problem Hamiltonian $\hat{H}_p$, whose ground state $|\Phi_p\rangle$ encodes the solution to the optimization problem. Typically, one performs a population transfer between two quantum states $|\Phi_i\rangle, |\Phi_p\rangle$, where $|\Phi_i\rangle$ is the lowest energy eigenstate of $\hat{H}_i$, via the annealing protocols $A(\tau), B(\tau)$ as $\hat{H}(\tau) = A(\tau)\hat{H}_i + B(\tau)\hat{H}_p$, with $\tau = t/T \in [0,1]$. In *adiabatic* quantum annealing [20–22] the population of the instantaneous ground state at any time τ stays constant, given the minimum instantaneous energy gap $\min_\tau \Delta E(\tau) = \min_\tau |\epsilon_m(\tau) - \epsilon_n(\tau)| \equiv \Delta E$ between the two lowest instantaneous eigenstates $|m(\tau)\rangle, |n(\tau)\rangle$ is non-zero at all times. The drawback is its slowness, as the adiabatic condition [14]

$$T \gg \max_{\tau\in[0,1]} \frac{|\langle m(\tau)|\partial_\tau \hat{H}(\tau)|n(\tau)\rangle|}{\Delta E^2} \tag{0.12}$$

states that experimental time T scales at best as $O(\Delta E^{-2})$. The default schedule is more often than not a linear ramp, e. g., $A(\tau) = 1 - \tau$ and $B(\tau) = \tau$, which is convenient as such choice enables the complete transfer from $\hat{H}_i$ to $\hat{H}_p$. Optimal adiabatic ramps [23] have a slightly different shape. As linear ramps show no bias towards system dynamics with respect to suspected energy gaps, optimal adiabatic schedules are typically slower in close proximity to the minimum gap, however allow for faster evolution at a distance from the gap as compared to linear ramps. Yet, due to the slowness in adiabaticity, the protocols $A(\tau), B(\tau)$ are often subject to more complex adaptations, providing a faster route to achieve results similar to adiabatic annealing [24].

0.5.3 Shortcuts to adiabaticity

Shortcuts to adiabaticity [25] include counterdiabatic driving protocols [26], that prevent the system from leaping onto higher energy states. Another, more recent approach encompasses the suppression of errors stemming from decoherence and diabatic transitions [27]. Alternatively, optimal control theory [28, 29] can be used to allow (and enforce) leaps to higher energy levels, whereby large overlap between simulated or experimental quantum state with the analytic ground state can be achieved even in a non-adiabatic regime. Consequently, recent studies include the automation process of designing annealing protocols [30] as well as optimizing them based on ground state fidelities [31], [32]. Lastly, not to forget the recent experiment on a D-Wave annealing device [33] giving proof of the scaling behavior of kinks within the Kibble-Zurek [34] framework for both open and closed quantum systems.

Part I

Simulation of correlated electrons

This part has been published as "Gino Bishop, Dmitry Bagrets and Frank K. Wilhelm, *Quantum algorithm for Green's-function measurements in the Fermi-Hubbard model*, Phys. Rev. A **111**, 062610" by the American Physical Society under the terms of the Creative Commons Attribution 4.0 International license. https://doi.org/10.1103/PhysRevA.111.062610. Text and software were written by G. Bishop. The design of quantum circuits was done in close collaboration by G. Bishop and D. Bagrets. The extension of the direct measurement scheme to the bosonization framework was conducted by D. Bagrets and is not laid out in this thesis.

Overview

In many-body physics, interactions and collective effects are central to the intricacy of phase diagrams observed in correlated systems. Under certain conditions, those systems can exhibit high-temperature superconductivity, i. e., a state of matter at which electric current flows without resistance, while tuning the same system can just as well yield a Mott-insulator, i. e., an insulating state induced by electron-electron interactions. Electrons, naturally correlated due to their repulsive forces amongst each other, promote the emergence of exotic phenomena. Advanced materials that can be tuned deliberately to induce superconducting or insulating phases need to be engineered so that quantum effects responsible for the desired properties can manifest. The superconducting phase emerges around the critical point controlled by doping. At lower doping level the Mott insulating phase re-emerges, at high doping one obtains the Fermi-liquid phase (, i. e., ordinary metal). Investigation of such systems and under which conditions certain phenomena arise is thus not only an academic, but a practical problem to solve [35].

The Fermi-Hubbard model (FHM) comprehensively describes the behavior of correlated electrons in a lattice, and is formally introduced in Ch. 1. Electrons are assigned a kinetic energy that allows them to hop to nearest neighbor sites. The sites themselves can be thought of as two orbitals, where each of them can contain an electron, with the spin anti-aligned as per Pauli exclusion principle. Additionally, the model introduces a repulsive force onto electrons, given two electrons occupy the same site. The competition between kinetic energy terms allowing electrons to propagate through a lattice and the repulsive forces amongst them leads to long range effects.

Real-world problems and the vast number of electrons associated with them render exact diagonalization infeasible. A more practical way of solving such systems is by means of the retarded GF. From the Lehmann representation, we obtain the analytic form

$$G^R_{m,n}(\omega) = \sum_k \left(\frac{\langle \Psi_0 | c_m | \Psi_k \rangle \langle \Psi_k | c_n^\dagger | \Psi_0 \rangle}{\omega - (E_k - E_0) + i\eta} - \frac{\langle \Psi_0 | c_n^\dagger | \Psi_k \rangle \langle \Psi_k | c_m | \Psi_0 \rangle}{\omega + (E_k - E_0) + i\eta} \right). \tag{0.13}$$

Here, ω is the frequency, $|\Psi_0\rangle$ is the ground state with ground state energy E_0, $|\Psi_k\rangle$ is the kth eigenstate with energy E_k, $c_n^{(\dagger)}$ is the fermion lowering (raising) operator on orbital n and η is an infinitesimally small parameter preventing singularities. It is a powerful tool in quantum chemistry, condensed matter and quantum field theory as it captures information about electronic interactions and excitations within the system. Having the exact GF of a given system at hand allows to deduce from it long-range order parameters. These can include s-wave and d-wave superconducting gaps or magnetic phases across a crystal. There are many forms of Green's functions, and in the case of many-body fermion systems, one often leverages the retarded GF, that describes the behavior of a system after it is perturbed.

In time-domain, we find the relation

$$G^R_{mn}(\tau,\tau') = -i\theta(\tau-\tau')\langle\{c_m(\tau), c_n^\dagger(\tau')\}\rangle, \tag{0.14}$$

where $\tau > \tau'$, $c_m^{(\dagger)}(\tau)$ is the fermion lowering (raising) operator on orbital m at time τ and $\theta(\tau-\tau')$ is the Heaviside step function enforcing causality. This seemingly innocent equation turns out to be surprisingly hard to evaluate. As it is stated, one could falsely assume that the simple accumulation of two-point time GFs is straightforward and rewards us with the full system GF. In practice however, to render the evaluation of this equation accurate, one needs to incorporate all of the orbitals, and all of their correlations, in a given crystal. Clearly, this is not practical. One way of circumventing the memory hazard is by stamping out subsystems, that are easier to handle with the computational resources at hand. Surely, a smaller system is easier to solve; however what is solved is a poor approximation of physical reality. All of the terms in Eq. (0.14) are influenced by orbitals outside the cutoff range in m, n, and thus outside our calculation. We have trapped ourselves in a dilemma: Real systems cannot be solved, and what is solvable is not real.

The discrepancy in accuracy of the latter approach is due to the influence of the self-energy Σ. We interpret the self-energy as a correction to the energy of a system and, for that matter, to the GF, cf. Eq. (0.13). The correction stems from the influential orbitals, that are neglected. The relation between self-energy and GF is established via the Dyson equation

$$\Sigma(\omega) = G_0^{-1}(\omega) - G^{-1}(\omega), \tag{0.15}$$

where

$$G_0(\omega) = \frac{1}{\omega - E_k + i\eta}, \quad G(\omega) = \frac{1}{\omega - E_k - \Sigma(\omega) + i\eta} \tag{0.16}$$

are the non-interacting GF and the interacting GF with the energy correction in the denominator with E_k being the energy of a particle with momentum k. The ground state energy is set to zero ($E_0 = 0$). While G_0 is relatively easy to obtain via single-particle physics, evaluation of the self-energy is still subject to many different approaches, underlining the difficulty in obtaining it [36].

In this thesis, we discuss a route based on the variational cluster approach. It is a perturbative, non-stochastic approach, that does not require the direct evaluation of the self-energy. Instead, the self-energy is implicitly included throughout the calculations. In the following, the variational cluster approach (VCA) is qualitatively outlined. Later on in Ch. 6 we will dive into mathematical detail.

Within the VCA, the central idea is to divide a computationally demanding system into two subsystems, which are tied together by the Dyson equation. As stated earlier, one of the major benefits of this method is that there is no need for explicit calculation of the self-energy of a system. What are these two subsystems?

One of them is coined the reference system and is a collection of duplicates of clusters, e. g., subsystems of the larger system, which are disconnected from each other. In fact,

evaluating Eq. (0.14) on such a cluster renders the calculation exact, since orbitals that could in principle influence the calculation are isolated. Albeit, the exactness only applies to the very restricted area of the solid.

The other system is then the interactions between the clusters, which we call V. This perturbation shall act as the effect of other orbitals which were neglected. We have on the one hand the exact GF of a cluster, which is per design not exact with respect to the full system. On the other hand, to make the cluster GF asymptotically exact for the full system, we do need to account for the orbitals outside the cluster — and we do so indirectly.

The relation between the two subsystems, and how they are woven together to form the full system, is once again described by a special case of the Dyson equation. Indeed, we simply exchange the self-energy with the perturbative potential V and exchange the non-interacting Green's function with the cluster Green's function $G'(\omega)$, since the potential is meant to simulate the environmental influence on a small region. The reformulated Dyson equation is now

$$V = G'^{-1}(\omega) - G^{-1}(\omega), \tag{0.17}$$

Careful administration of perturbative terms targeting the cluster system allows to treat only a tiny fraction as the equivalent of the full system. Michael Potthoff has found a relation between the grand potentials of both the objective (, i. e., a large lattice system) and the reference system (, i. e., a small cluster system) [37]. It states, that the grand canonical potential (GCP) of the large system depends on the GF and the GCP of the reference system. Thereby, in a self-consistent fashion, we can vary perturbation parameters to the cluster reference system until a saddle-point with respect to the objective system's GCP is found. It can be shown that finding the saddle-point of the large system is equivalent to satisfying the Dyson equation. Having found that saddle-point thus means that the cluster system in first approximation is a good representative of the large system.

Why, even after solving the Dyson equation, does it remain only an approximation? If a cluster is very small, then the majority of correlations amongst all orbitals needs to be captured by the perturbation V, whereas if the cluster is large enough, a good fraction of interactions is already taken into account in the cluster. For a cluster of similar size as the system, the perturbation would not be needed at all. Consequently, small clusters imply relatively poor agreement of the simulated and physical environment. Surely, two ways of increasing the quality of results is extending the clusters, and making good guesses on the perturbative terms, specifically, which long range parameters they cover. It may sound like a tedious task, however the rewards are staggering. The more careful a perturbation is designed, i. e., the more long range parameters are meaningfully integrated into the perturbation Hamiltonian, the easier it will be later on to deduce the superconducting gap, magnetic phases, density of states and on-site chemical potentials or impurities. All of that becomes a simple algebraic task, once the saddle-point is found. We have established the importance of the Green's function, but do not yet know how to evaluate it.

Since the Green's function captures all of the two-point time correlation functions, evaluating it on classical platforms is only feasible for relatively small systems. For more interesting,

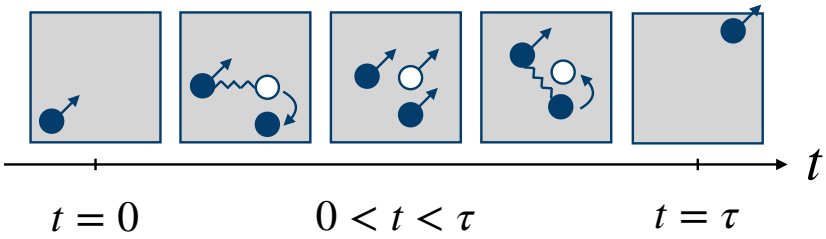

Figure 0.2: One of many possible scattering processes. At time $t = 0$, an electron is injected into a system. At $t > 0$, the added electron interacts (zigzag line) with another electron, lifting it out of its place. A hole emerges at the vacancy of the displaced electron. The presence of the hole alongside the rearrangement of electrons in the nearest vicinity results in the injected electron becoming dressed by the influences of these interactions. Finally, at $t = \tau$ the additional electrons once again interacts with the displaced electron, drawing it back to its old place, thus annihilating the hole. Image is reproduced from [38].

real world scenarios, quantum routines offer immense scaling benefits. In fact, the scaling in the number of evaluations reduces from exponential to quadratic in number of lattice sites, if we were to evaluate the Green's function on a quantum computer, cf. Sec. 3.4. One way to evaluate the Green's function is by means of the Hadamard test.

The Hadamard test is laid out in operational detail in Sec. 3.2.1. Qualitatively, it can be seen as a straight forward approach to perturb a system in a way as to inject (at time t) and extract (at time $\tau > t$) from it a fermion and check, how the system is influenced by the sudden presence and absence of a fermion. One possible process is depicted in Fig. 0.2.

However, the Hadamard test does have one drawback: It only works in the context of the JW transformation, a highly non-local transformation that comes with the cost of long Pauli strings, Fig. 3.3.

The JW transformation is necessary since the Hadamard test involves single Majorana operators as introduced in Sec. 0.3.2. In anticipation of subsection 3.2.1 the circuit representation of the Hadamard test involves a control on single fermion operators as they appear in Eq. 0.14. Since the ancilla qubit controlling the evolution is not part of the fermionic system Hilbert space, the Majorana operations remain single-fermion (non-pairwise) operators. Typically, mappings that aim to preserve locality often explicitly require the insertion of pairs of fermions in contrast to single fermions [39]. Note, that in the compact encoding by Derby and Klassen [40] the odd fermionic subspace can be either accessible or not for the open boundary conditions depending on particular implementation details within this scheme. In general, if we were to use more advanced, locality-preserving mappings, then a different algorithm needs to be used for the Green's function. In scattering experiments one often investigates the response of a system to a given perturbation. If the perturbation is sufficiently small, then the response is expected to be linear. It turns out, that an algorithm based on linear response theory allows for the injection of pairs of fermions.

What is a perturbation? To study single-particle GF, one could introduce a hopping perturbation. It alters the distribution of fermions, probing their individual ability to react to

potential changes in the nearest environment. One then measures the change in the parity expectation value over time, scaling proportionally to a response function. At last, the response function of a system is the retarded GF. Since we measure the response function in terms of a change in expectation values, we call this protocol the direct measurement scheme.

A two-site dimer shall serve as our toy model, for which we demonstrate the direct measurement of the Green's function and pave the way to combine it with the VCA for determining the phase diagram of such a dimer. The isolated cluster (e. g., a dimer) thus consists of two correlated c orbitals, for which each is coupled to a bath site b that promotes delocalization. Carefully tuning the ratio of hopping to interaction strength within the VCA reveals the transition from a metallic state to a Mott insulator.

1 Fermi-Hubbard model

Strongly correlated electron materials exhibit exotic phenomena such as high-temperature superconductivity [41] and Mott-insulating phases [42]. Investigating these effects and their origins is therefore crucial for promoting sophisticated material design [43], magnetic levitation systems [44] and advanced energy storage [45]. Strong correlation arises due to Coulomb interaction between electrons and can be captured within the Fermi-Hubbard model [46]. With adding strong disorder, this model demonstrates yet another intriguing phenomenon, the many-body localization (MBL), both in one- and two-dimensions [47–49]. All these effects are captured by the Fermi-Hubbard. Its Hamiltonian reads

$$\hat{H} = -t \sum_{\langle i,j\rangle,\sigma} \left(\hat{c}^{\dagger}_{i\sigma} \hat{c}_{j\sigma} + \hat{c}^{\dagger}_{j\sigma} \hat{c}_{i\sigma} \right) + U \sum_{i} \hat{n}_{i\uparrow} \hat{n}_{i\downarrow}, \tag{1.1}$$

where t is the hopping, $\hat{c}^{\dagger}_{i\sigma}$, $\hat{c}_{i\sigma}$ are the fermionic creation and annihilation operators, U is the Coulomb repulsion and $\hat{n}_{i\uparrow}, \hat{n}_{i\downarrow}$ are the fermion number operators for spin-up and spin-down, respectively. In Fig. 1.1, the behavior of electrons is depicted. Electrons can hop to neighboring sites, if and only if the associated orbital is not occupied, yet (see green dashed arrows). If two electrons sit on the same site, they are subject to a repulsive force (see red squares). Solid lines represent a possible form of a small cluster.

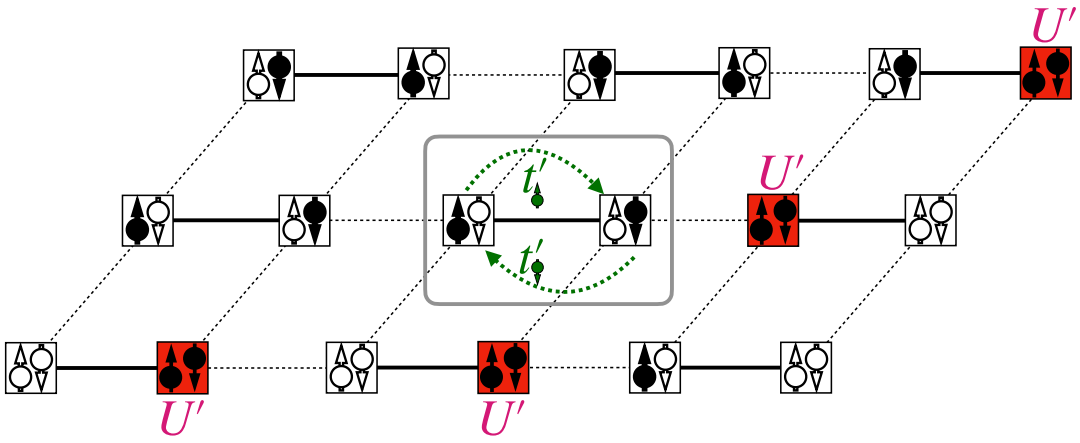

Figure 1.1: 2D lattice representing the Fermi-Hubbard model at half-filling. Each site can be occupied by at most two fermions. Dashed and solid lines show the allowed hopping to neighboring sites. Two fermions occupying a single site are subject to a Coulomb repulsion U'. Solid lines indicate a possible arrangement of two-site clusters, that aggregate to a larger system. Spin orbitals are either black (filled) or white (not filled).

1.1 Known properties

The Fermi-Hubbard model is considered exactly solvable in 1D in the thermodynamic limit [50–52]. Yet in higher dimensions, such a solution does not exist, which renders the FHM not exactly solvable beyond 1D (at least, in reasonably short time).

The absence of an analytical solution is partly offset by known properties associated to model parameter limits. We provide a summary thereof in Tab. 1.1. Four cases are being distinguished: Firstly, the non-interacting limit, $U = 0$, secondly the strong interacting limit $U \to \infty$, thirdly $t = 0$ and lastly $t \approx U$.

Limit	Description
$U = 0$	Tight-binding regime. The electrons are not interacting, the self-energy is zero. Mott-insulation is not possible. The ground state is a Fermi gas with energy levels filled up to the Fermi energy.
$U \to \infty$	Strong correlation regime. The system becomes a Mott insulator at half-filling. Electrons are localized, and no two electrons can occupy the same site. For below half-filling, mobility is in principle possible, albeit highly restricted.
$t = 0$	Mott insulator. Electrons are fully localized with no possibility of hopping to other sites. The ground state is highly degenerate.
$t \approx U$	Moderate correlation regime. The competition between kinetic energy and on-site repulsion creates Mott insulating, superconducting, and magnetic states, contributing to the richness in the phase diagram.

Table 1.1: Known properties of the Fermi-Hubbard model in various limits.

1.2 Strategies to solve the Fermi-Hubbard model

In continuation of the previous section, the FHM is not exactly solvable beyond one dimension. Numerical methods face an inherently exponential demand in computational resources, when transitioning to larger system sizes.

A common approach to think about the Fermi-Hubbard model is by means of Feynman diagrams [53], which is a diagrammatic perturbation theory approach. In a nutshell, one sums up all interaction processes amongst the particles, as well as exchange interactions, virtual excitations, and their infinite series of possibilities in generating such diagrams — albeit knowing that more complex diagrams are less likely to play out in reality, giving it a lesser probability amplitude. This is approach quickly becomes intractable for more

effective correlations, as the number of possible diagrams, i. e., those with probability amplitudes significant enough to be included in a series, grows exponentially.

In practice there exist a handful of methods dealing with the evaluation of the GF and/or self-energy [54]. Stochastic methods such as Quantum Monte Carlo [55] (QMC) do not require the evaluation of the self-energy as they are mainly used for finding the minimum energy state. Not to forget the sign problem, arising from the sign change in the wave function due to exchange of particles.

In this thesis, we put emphasis on cluster perturbation methods [56–58]. They are capable of mitigating computational demands by dividing a lattice system into arbitrarily small, identical and disjoint clusters. The idea is to solve one of the many clusters and extrapolate the result to the full system in a self-consistent fashion.

The VCA [59] can be used to relate the free energy of a microscopic cluster to the GCP of a macroscopic system. When the latter is found, it provides an access to the phase diagram of a given material. As the crucial step, the VCA scheme involves an evaluation of the Green's function which describes one-particle correlations in the interacting system. In practical terms it amounts to an evaluation of the Green's function using relatively small quantum chips, which are build up of as many qubits as the number electronic orbitals contained in a cluster, plus at least one ancilla qubit.

A common strategy to evaluate the cluster's GF of a correlated system is based on the Hadamard test [60–64]. As the core ingredient, it requires an implementation of controlled single-particle fermionic operators. The latter is not problematic, provided the most well-known mapping, the JW transformation, is used to encode fermion degrees of freedom on a quantum computer. On the other hand, local fermion-to-qubit mappings, using additional ancilla qubits, have been gaining popularity recently [40, 65, 66], which are beneficial in two- or higher dimensions. A special feature of all these methods is that they construct products of an *even* number of fermionic operators, in particular bilinears, while single fermionic operators remain inaccessible. As the result, though above advanced constructions can be used to efficiently generate an evolution operator of the Fermi-Hubbard model, they pose an evident problem to implement the Hadamard test.

In this work, we propose a new quantum algorithm, which is rooted in the Kubo formula of linear response theory [67], and adapted here for quantum circuits (the linear response approach finds it application in a variety of classical scattering [68] and transport measurement experiments [69]). This algorithm allows to access the Green's function directly using only bilinears of fermionic operators. Its construction is based solely on the algebra of Majorana operators and as such it is applicable to any local fermion-to-qubit mapping schemes. Provided the Jordan-Wigner encoding is used, the complexities of our new algorithm and the Hadamard test match.

The following chapters shall lay the foundation to measure the GF. The quantum circuits that represent the FHM are shown (Ch. 2) and put together (Ch. 3) to showcase the new algorithm on a toy model (Ch. 4).

2 Circuit representation of the Fermi-Hubbard Model

We start this section by outlining the Jordan-Wigner transformation (for simplicity, any operator $\hat{O}$ maps to $\hat{O} \mapsto O$) and present the GF in terms of fermions. A unitary transformation is used to pivot to Hermitian Majorana fermions.

It is followed by a review of well known results in the literature [57] on how a unitary time evolution of the Fermi-Hubbard model can be represented by a quantum circuit. This is used to introduce an algorithm for the Green's function measurement based on linear response theory in the subsequent chapter 3.

2.1 Jordan-Wigner mapping

To construct an evolution operator of the cluster Hubbard Hamiltonian related to a single Trotter step, one needs to map fermionic operators to the qubit ones. This can be achieved in two stages. First, we introduce *Majorana fermions*, $x_{i\sigma} = c_{i\sigma} + c_{i\sigma}^\dagger$ and $y_{i\sigma} = i(c_{i\sigma} - c_{i\sigma}^\dagger)$, which are Hermitian operators. They obey to the anti-commutation relations

$$\begin{aligned} \{x_{i\sigma}, x_{j\sigma'}\} &= \{y_{i\sigma}, y_{j\sigma'}\} = 2\delta_{ij}\delta_{\sigma\sigma'}, \\ \{x_{i\sigma}, y_{j\sigma'}\} &= 0. \end{aligned} \tag{2.1}$$

At the second stage, the Jordan-Wigner transformation is used to represent $x_{i\sigma}$ and $y_{i\sigma}$ via the following sequences of X-, Y and Z-gates:

$$\begin{aligned} x_{i\uparrow} &= \mathbb{I}^{\otimes 2(N_c-i)+1} \otimes X \otimes Z^{\otimes 2(i-1)}, \\ x_{i\downarrow} &= \mathbb{I}^{\otimes 2(N_c-i)} \otimes X \otimes Z^{\otimes 2i-1}, \\ y_{i\uparrow} &= -\mathbb{I}^{\otimes 2(N_c-i)+1} \otimes Y \otimes Z^{\otimes 2(i-1)}, \\ y_{i\downarrow} &= -\mathbb{I}^{\otimes 2(N_c-i)} \otimes Y \otimes Z^{\otimes 2i-1}, \end{aligned} \tag{2.2}$$

which guarantees satisfiability of the anti-commutation relations Eq. (2.1). Consequently, we define the correlation function for original fermions,

$$iG_{ij}^{\sigma\sigma'}(\tau) = \begin{pmatrix} \langle\{c_{i\sigma}(\tau)c_{j\sigma'}^\dagger(0)\}\rangle & \langle\{c_{i\sigma}(\tau)c_{j\sigma'}(0)\}\rangle \\ \langle\{c_{i\sigma}^\dagger(\tau)c_{j\sigma'}^\dagger(0)\}\rangle & \langle\{c_{i\sigma}^\dagger(\tau)c_{j\sigma'}(0)\}\rangle \end{pmatrix}, \tag{2.3}$$

and for Majorana ones

$$ig_{ij}^{\sigma\sigma'}(\tau) = \begin{pmatrix} \langle\{x_{i\sigma}(\tau)x_{j\sigma'}(0)\}\rangle & \langle\{x_{i\sigma}(\tau)y_{j\sigma'}(0)\}\rangle \\ \langle\{y_{i\sigma}(\tau)x_{j\sigma'}(0)\}\rangle & \langle\{y_{i\sigma}(\tau)y_{j\sigma'}(0)\}\rangle \end{pmatrix}. \tag{2.4}$$

The two representations are related by a unitary transformation

$$G_{ij}^{\sigma\sigma'}(\tau) = \frac{1}{2} M^{\dagger} g_{ij}^{\sigma\sigma'}(\tau) M, \quad M = \frac{1}{\sqrt{2}} \begin{pmatrix} 1 & 1 \\ i & -i \end{pmatrix}. \tag{2.5}$$

For the sake of generality, we do not imply any time ordering in the definition of the Green's functions.

2.2 Quantum circuits representations

Following [57], we present quantum circuits for a time step $\Delta\tau$ for both hopping and repulsion as per the Fermi-Hubbard model, Eq. (1.1). Their representation are taken as ingredients for both the interacting ground state preparation as well as for the Trotterized time evolution.

We also present the notation of gates alongside their matrix representation. The notation is kept throughout the thesis.

2.2.1 Hopping circuit

For our subsequent discussion of the Green's function measurement scheme (see Sec. 3.2.2) it is instructive to rationalize the circuit behind the hopping term, shown in Fig. 2.1. Here, the gate $X_{\pi/2}$ refers to the Y-basis change gate.

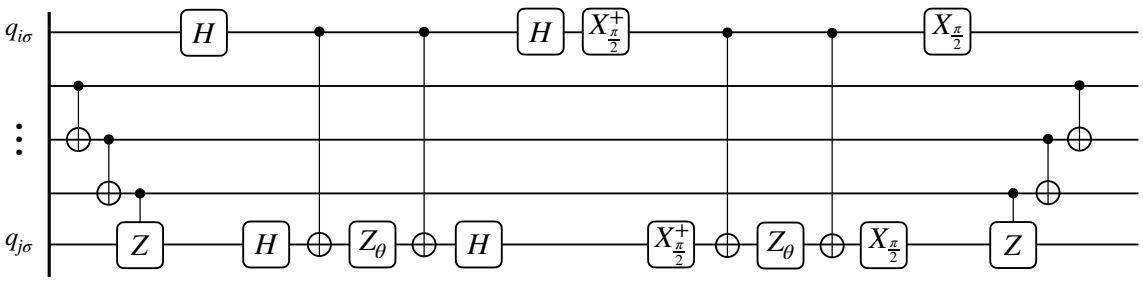

Figure 2.1: Hopping circuit to evaluate the term $t_{ij}(c^{\dagger}_{i,\sigma} c_{j,\sigma} + \text{h.c.})$ for a time step $\Delta\tau$ with angle $\theta = t_{ij}\Delta\tau$.

To this end we note that its representation in terms of Majorana fermions reads

$$h_{ij}^{\sigma\sigma} = c^{\dagger}_{i\sigma} c_{j\sigma} + \text{h.c} = \frac{i}{2} \left(y_{i\sigma} x_{j\sigma} - x_{i\sigma} y_{j\sigma} \right). \tag{2.6}$$

The Jordan-Wigner transformation (Eq. (2.2)) reduces the above operator to

$$h_{ij}^{\sigma\sigma} = \frac{1}{2} \left(X_m X_n + Y_m Y_n \right) Z_{\text{JW}}(m, n), \tag{2.7}$$

where $m = 2i + (1-\sigma)/2$, $n = 2j + (1-\sigma)/2$ and $Z_{\mathrm{JW}}(m,n)$ stands for the Jordan-Wigner string,

$$Z_{\mathrm{JW}}(m,n) = \bigotimes_{k=m+1}^{n-1} Z_k, \tag{2.8}$$

with Pauli operators X_k, Y_k and Z_k acting on kth qubit. We can then introduce unitary Clifford gates S_{mn} acting on all qubits k with $m < k < n$ (its equivalent circuit is shown in Fig. 2.2), for which the role is to eliminate the Jordan-Wigner string and simplify Eq. (2.7) to

$$h_{ij}^{\sigma\sigma} = \frac{1}{2} S_{mn}^{\dagger} \left(X_m X_n + Y_m Y_n \right) S_{mn}. \tag{2.9}$$

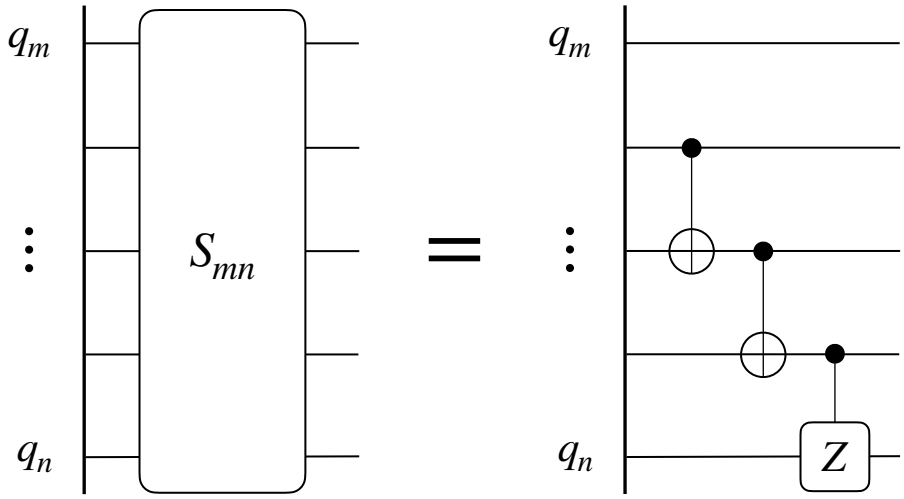

Figure 2.2: Definition of the operator S_{mn}, for which the purpose is to remove Jordan-Wigner strings. It is non-trivial for $m - n \geq 2$ and we set $S_{n+1,n} = \mathbb{1}$.

The XX- and YY-terms above commute, so that an evolution operator generated by $h_{ij}^{\sigma\sigma}$ naturally splits into the product of two. Subsequent unitary transformations using single qubit gates H and $X_{\pi/2}$ transform each term of the sum in Eq. (2.9) to the product $Z_m \otimes Z_n$. After that, the unitary evolution corresponding to a single Trotter step of a hopping operator with an angle $\theta = t_{ij}\Delta\tau$ is realized with the help of Z-rotations and additional similarity transformations with CNOT gates, as shown in Fig. 2.1.

2.2.2 Repulsion circuit

A circuit for the repulsion is shown in Fig. 2.3.

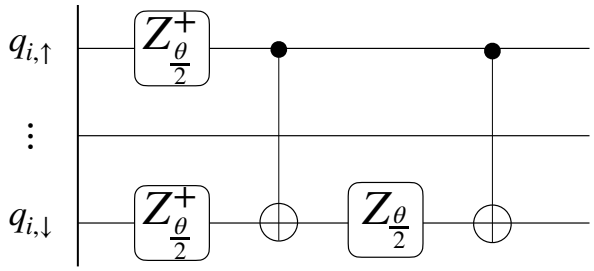

Figure 2.3: Repulsion circuit to evaluate the term $U_i n_{i,\uparrow} n_{i,\downarrow}$ for a time step $\Delta\tau$ with angle $\theta = U_i \Delta\tau$.

2.2.3 Gate set

The following gate notation has been used for circuit design.

Gate	Symbol	Matrix
Hadamard	H	$\frac{1}{\sqrt{2}}\begin{pmatrix}1 & 1\\ 1 & -1\end{pmatrix}$
X	X	$\begin{pmatrix}0 & 1\\ 1 & 0\end{pmatrix}$
Z	Z	$\begin{pmatrix}1 & 0\\ 0 & -1\end{pmatrix}$
Z-rotation	Z_θ	$\begin{pmatrix}e^{-i\theta/2} & 0\\ 0 & e^{i\theta/2}\end{pmatrix}$
Y-basis change	$X_{\frac{\pi}{2}}$	$\frac{1}{\sqrt{2}}\begin{pmatrix}1 & -i\\ -i & 1\end{pmatrix}$
Phase	T_θ	$\begin{pmatrix}1 & 0\\ 0 & e^{i\theta}\end{pmatrix}$
Controlled-Not		$\begin{pmatrix}1 & 0 & 0 & 0\\ 0 & 1 & 0 & 0\\ 0 & 0 & 0 & 1\\ 0 & 0 & 1 & 0\end{pmatrix}$
Controlled-Z	Z	$\begin{pmatrix}1 & 0 & 0 & 0\\ 0 & 1 & 0 & 0\\ 0 & 0 & 1 & 0\\ 0 & 0 & 0 & -1\end{pmatrix}$

Table 2.1: Full list of applied gates in matrix representation. Note, that a superscript '+' refers to the Hermitian conjugate.

3 Evaluation of the Green's function on a quantum computer

This chapter aims to put all the pieces together, that are necessary to evaluate the GF. We start with showing an approach to generate an equilibrium ground state. With this at hand, we present two routes, the Hadamard test and the direct measurement scheme, and showcase the composition of quantum circuits representing the associated quantum algorithms.

3.1 Preparing the ground state

Both of the to-be-presented routes ask for the ground state as the starting point for the quantum routines. The variational Hamiltonian ansatz [70] is a variational algorithm that provides the minimum energy angles needed to rotate an initial non-interacting ground state to the interacting ground state. To that end, energy measurements need to be performed.

3.1.1 Variational Hamiltonian ansatz (VHA) for the ground state

The correlation functions defined by Eq. (2.3) presume the average over the equilibrium density matrix. At zero temperature one is required to start from the ground state of the cluster at time $\tau = 0$. For this reason we will briefly review the variational Hamiltonian ansatz (VHA), which is used to construct the ground state.

The defining idea of VHA is to find a unitary operator $U(\theta)$, such that under variations of the parameters θ_i from the set θ one minimizes the energy expectation value $\langle\Psi_0|U^\dagger(\theta)HU(\theta)|\Psi_0\rangle$, where $|\Psi_0\rangle$ is a guess state which can be prepared easily. Identifying an underlying operator H as the sum of p independent terms $H = \sum_{j=1}^{p} H_j$, the operator $U(\theta)$ is defined over n steps as

$$U(\theta) = \prod_{k=1}^{n}\prod_{j=1}^{p} e^{-i\theta_{j,k}H_j}. \tag{3.1}$$

In each step k, the p parameters are updated until energy measurements on $|\Psi\rangle = U(\theta)|\Psi_0\rangle$ yield minimum values. An example for a rule set governing the update of $\theta_{j,k}$ can be found in [71].

3.1.2 Measuring ground state energy

Finding the minimum expectation value $\langle\Psi_0|U^\dagger(\theta)HU(\theta)|\Psi_0\rangle$ requires energy measurements. From Eq. (1.1) we find terms for hopping and repulsion, which in the following

we refer to as H_0 and H_U, respectively. Hence, schedules for measurement of hopping and repulsion energy, cf. [56], are reviewed.

Energy measurements of repulsion are done by measuring each qubit in the computational basis. Since we operate within the Jordan-Wigner framework, repulsion terms are mapped to the matrix $|11\rangle\langle 11|_{mn}$, where m, n correspond the inspected orbitals. It comes from the representation of the number operators, $n_{i\sigma} = \frac{1}{2}(\mathbb{I} - Z_{i\sigma})$. A term $n_{i\uparrow}n_{i\downarrow}$ (cf. Eq. (1.1)) is thus equal to $\frac{1}{4}(\mathbb{I} - Z_{i\uparrow} - Z_{i\downarrow} + Z_{i\uparrow}Z_{i\downarrow})$, which in turn can be implemented ($n = i\uparrow, m = i\downarrow$) such that the energy equals the probability to find both qubits to be in state $|1\rangle$.

Measurements of kinetic energies depend on the hopping direction, which is rooted in the way how the Jordan-Wigner strings are chosen in the mapping (2.2). For one of the possible choices (see snake pattern in Fig. 3.3) horizontal hoppings are considered less costly in terms of gate depth since Jordan-Wigner strings can be neglected, whereas vertical hoppings may lead to long Jordan-Wigner strings.

Following [56], horizontal hopping map to the matrix $1/2(X_nX_{n+1}+Y_nY_{n+1})$. The eigenstates are $|\psi_\pm\rangle = 1/\sqrt{2}(|01\rangle \pm |10\rangle)$. In order to perform computational basis measurements, the unitary that diagonalizes $\frac{1}{2}(X_nX_{n+1} + Y_nY_{n+1})$ into $|01\rangle\langle 01| - |10\rangle\langle 10|$ is shown in Fig. 3.1. Desired energy expectation is thus the probability of measuring $|01\rangle$ minus the probability of measuring $|10\rangle$.

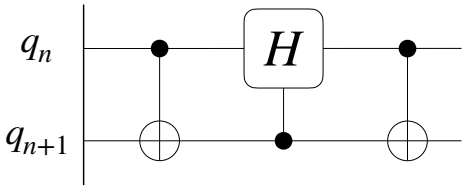

Figure 3.1: Circuit for diagonalizing $\frac{1}{2}(X_nX_{n+1} + Y_nY_{n+1})$ into $|01\rangle\langle 01| - |10\rangle\langle 10|$.

On the other hand, a kinetic energy term $h_{ij}^{\sigma\sigma}$ describing vertical hopping is mapped to the operator (Eq. (2.7)), which contains an additional Jordan-Wigner string. As discussed in subsection 2.1, the latter can be eliminated by similarity transformation via the unitary S_{mn} shown in Fig. 2.2. Afterwards, one can measure two terms in $h_{ij}^{\sigma\sigma}$ separately. The quantum circuit to implement the measurement of the first term, $iy_{i\sigma}x_{j\sigma}$, is given in Fig. 3.2.

It is based on the following similarity transformation of this operator, i. e.,

$$\begin{aligned} iy_{i\sigma}x_{j\sigma} &= \mathbf{S}_{mn}^{\dagger}\,(Z_mZ_n)\mathbf{S}_{mn}, \\ \mathbf{S}_{mn} &= (\mathrm{H}_m\mathrm{H}_n)\,S_{mn}. \end{aligned} \tag{3.2}$$

The expectation value of this operator is then reduced to the average parity of qubits (m, n).

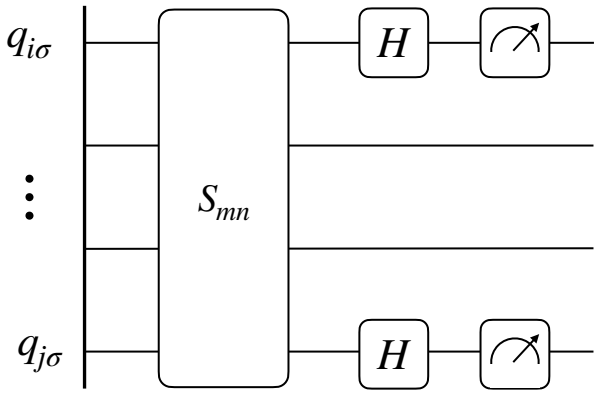

Figure 3.2: Measurement of $iy_{i\sigma}x_{j\sigma}$ term reducing to $\langle Z_{i\sigma}Z_{j\sigma}\rangle$ after a similarity transformation.

A measurement of the second term in the hopping term, $-ix_{i\sigma}y_{j\sigma}$, is implemented along the same lines with the only difference that the Hadamard gate is replaced by $X_{\pi/2}$.

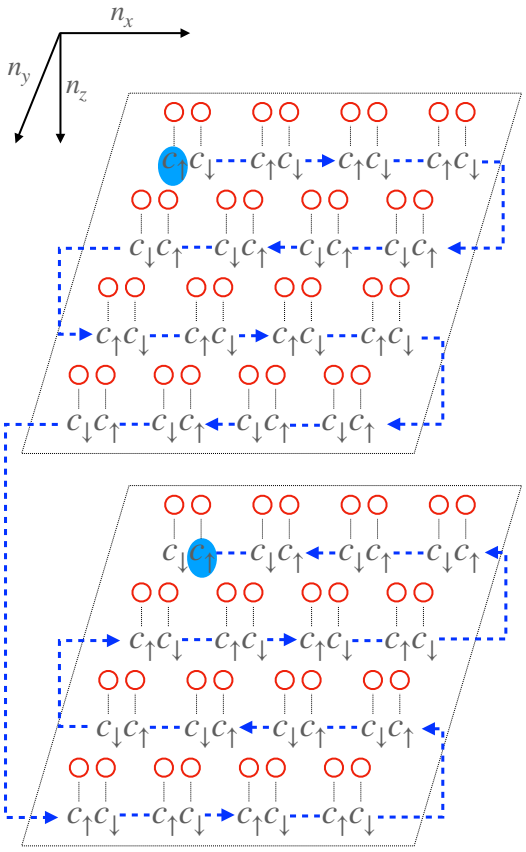

Figure 3.3: Worst case hopping between two neighbored orbitals (highlighted in blue ovals) in 3D with maximum distance from each other. The dashed blue line is the route which gives rise to the longest Jordan-Wigner string. Note, that in general there are more than one of such routes. Red circles represent a heat bath, which is coupled to the corresponding c-fermion. Coordinate numbers n_x, n_y, n_z count the number of clusters (dimers) in x, y, z-direction. Here: $n_x = 4, n_y = 4, n_z = 2$.

3.2 Green's function measurement

We present two routes to measure the Green's function. The orthodox way goes back to the Hadamard test circuit originally proposed in Ref. [60], see Fig. 3.5. Another one makes use of linear response theory, particularly the Kubo formula, which we present afterwards.

3.2.1 The Hadamard test

This section benefits structurally from describing the evolution of the Hadamard test in terms of three stages, starting with the textbook example (first stage) and ending at the optimized applicable circuit (third stage).

3.2.1.1 First stage

The simplest possible Hadamard test [72] is a blueprint for measuring observables. Given a unitary qubit operator $\hat{\mathcal{U}}$ with eigenvalues $\{+1, -1\}$, we wish to measure the associated observable. The quantum circuit for this endeavor is depicted in Fig. 3.4.

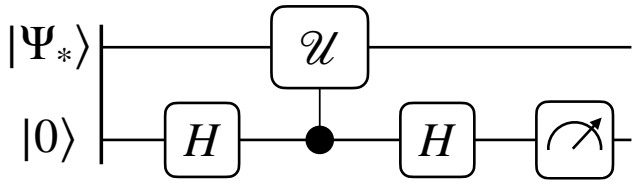

Figure 3.4: Simplest Hadamard test to measure an observable U.

Over many runs, the mean value of random binary variables (± 1) gives $\mathrm{Re}\langle\Psi_*|\mathcal{U}|\Psi_*\rangle$. Here, $|\Psi_*\rangle$ denotes an initial quantum state and $\mathcal{U}$ is an arbitrary unitary acting on $|\Psi_*\rangle$.

3.2.1.2 Second stage

The shown circuit can become more elaborate, given the observable one wishes to measure. For instance, in application to the Green's function measurement within the VCA framework, the wave function $|\Psi_*\rangle$ represents an (approximate) ground state of a Hubbard cluster and one sets $\mathcal{U} = U^\dagger(\tau)\sigma_\nu U(\tau)\sigma_\mu \equiv \sigma_\nu(\tau)\sigma_\mu$, where σ_μ may refer to any of the Hermitian Majorana operators x_μ, y_μ. The averaged real part of $\mathcal{U}$ then coincides with the retarded correlator of two Majoranas, that is

$$\mathrm{Re}[ig_{\mu\nu}(\tau)] = \frac{1}{2}\langle\Psi_*|\{\sigma_\nu(\tau), \sigma_\mu\}|\Psi_*\rangle. \tag{3.3}$$

The corresponding circuit to evaluate the Green's function within the above scheme is given in Fig. 3.5.

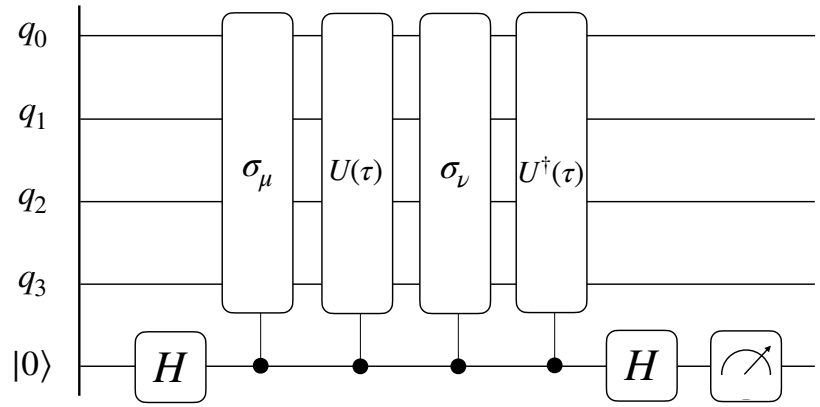

Figure 3.5: Quantum circuit for measuring the correlation functions $C_{\mu\nu}$. The first four qubits $q_0, \cdots, q_3$ represent the physical system, whereas the last qubit in state $|0\rangle$ represents the control qubit.

Here $q_0, \cdots, q_3$ are qubits representing a small physical system (e. g., the four qubit cluster), while the last qubit is an ancilla whose initial state is $|0\rangle$. Within the logic of Hadamard test the correlation function $g_{\mu\nu}(\tau)$ can be then estimated as

$$\mathrm{Re}[ig_{\mu\nu}(\tau)] = P_{\mu\nu}(\mathcal{M} = 0, \tau) - P_{\mu\nu}(\mathcal{M} = 1, \tau), \tag{3.4}$$

where $P_{\mu\nu}(\mathcal{M}, \tau)$ denotes the empirical probability of measuring the ancilla in the state $\mathcal{M}$ at time τ.

As for the analogy from the Overview, see Fig. 0.2, a perturbation is induced to the system, which we denote as σ_μ, acting on qubit q_μ. Those perturbations may represent the injection of an electron at time $\tau = 0$ at later extraction thereof. An inverse time evolution is needed to measure the change in the expected system dynamics.

The Hadamard test circuit requires four blocks of controlled evolution, which include computationally costly two-qubit gates.

3.2.1.3 Third stage

Recently, Endo et al., [73], presented a more elegant version of the Hadamard test (it finds its roots in the pioneering work [60]), whose circuit is presented in Fig. 3.6. For the recent realization of such scheme, we refer to the work [64].

If the average is performed over the ground state, then one evolution operator can be omitted thereby reducing the amount of gates by a factor of two. Additionally, the time evolution is not controlled. Single-qubit gates in the evolution are not rendered to two-qubit gates, as is the case in the second stage.

While the two-qubit gate scaling is clearly the most favorable, the necessity of employing a JW transformation is a defining feature of this algorithm.

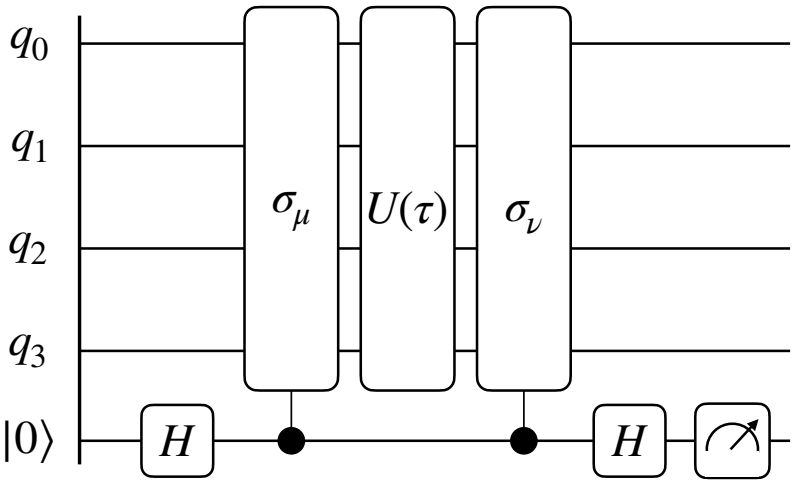

Figure 3.6: Quantum circuit for the (third stage) Hadamard test. The main advantage is that it does not require a controlled unitary evolution $U(\tau)$.

In the following subsection we discuss the new direct measurement scheme which is more physical in that the latter can be applied to more sophisticated, particularly locality-preserving mappings (e. g., the one pointed to in Sec. 3.3), that do not allow for single Majorana fermion operators.

3.2.2 Direct measurement

In this subsection we propose an alternative approach to evaluate the Green's function on a quantum computer, which we refer to in what follows as the direct measurement. It requires no assumption on the initial density matrix ρ_0 of a simulated many-body system and, in contrast to the second stage Hadamard test, relies merely on the forward uncontrolled evolution operator $U(\tau)$. Furthermore, we use the two-site dimer toy model to demonstrate the direct measurement and probe its potential for being a superior method for accessing the system's Green's function.

3.2.2.1 Brief review of linear response theory

Exploiting Green's functions for calculating observables and order parameters is motivated by linear response theory (cf. Appendix A.1). Let $H'(\tau) = H + V(\tau)$ be our system of interest, with H being the stationary, time-independent part and $V(\tau) = \sum_i \Phi_i(\tau) A_i$ being the time-dependent perturbation, whose exact form we specify momentarily. Linear response theory describes how the system reacts to a given perturbation $V(\tau)$, where $\Phi_i(\tau)$ is the interaction strength of operator A_i. If we assume a sufficiently weak perturbation, the change in an expectation value of any Heisenberg operator $\tilde{A}_i(\tau)$ defined relative to the full Hamiltonian $H'(\tau)$ is linear in the perturbing source $\Phi(\tau)$. This is formulated as

$$\delta\langle \tilde{A}_i(\tau)\rangle = \int \mathrm{d}\tau' \chi_{ij}(\tau;\tau')\Phi_j(\tau'), \tag{3.5}$$

where $\chi_{ij}(\tau;\tau')$ is the response function given by

$$\chi_{ij}(\tau,\tau') = -i\theta(\tau-\tau')\langle[A_i(\tau), A_j(\tau')]\rangle. \tag{3.6}$$

Here, operators $A_j(\tau)$ evolve under the action of the non-perturbed Hamiltonian H and, as before, is averaged over an initial density matrix ρ_0. In particular, for the perturbation localized in time at time τ', one writes $\Phi_j(\tau) = \Phi_j\,\delta(\tau-\tau')$, and arrives at the relation

$$\delta\langle\widetilde{A}_i(\tau)\rangle = \sum_j \chi_{ij}(\tau;\tau')\Phi_j. \tag{3.7}$$

which can be used to extract the response function in the demonstration. One assumes here that Φ_j is relatively small so that non-linear effects can be disregarded.

3.2.2.2 Adaptation to the Green's function measurement

To adapt this general idea to the Green's function measurement of c-fermions in our system, we couple them to an auxiliary spinless d-fermion with the Hamiltonian $H_d = \epsilon_d d^\dagger d$ and introduce the hopping operator

$$A_j^\sigma = d^\dagger c_{j\sigma} + c_{j\sigma}^\dagger d \tag{3.8}$$

acting on the jth fermion, while the ancilla qubit stores the state of the d-fermion. The explicit form of the perturbation $V(\tau)$ then reads

$$V(\tau) = \sum_j \Phi_j^\sigma(\tau)A_j^\sigma = \sum_j \Phi_j^\sigma(\tau)[d^\dagger c_{j\sigma} + c_{j\sigma}^\dagger d], \tag{3.9}$$

where again $\Phi_j^\sigma(\tau)$ is the external field acting on the jth fermion with spin σ. Furthermore, considering the response function Eq. (3.6) we may assume $\tau' = 0$ and $\tau > \tau'$ such that we can neglect the τ'-dependence. The commutator then becomes

$$\chi_{ij}^{\sigma\sigma'}(\tau) = -i\Big(\langle A_i^\sigma(\tau)A_j^{\sigma'}\rangle - \langle A_j^{\sigma'}A_i^\sigma(\tau)\rangle\Big). \tag{3.10}$$

Using Eq. (3.8), this leads to

$$\begin{aligned}\chi_{ij}^{\sigma\sigma'}(\tau) = &-i\Big\langle\big(d^\dagger(\tau)c_{i\sigma}(\tau) + c_{i\sigma}^\dagger(\tau)d(\tau)\big)\cdot\big(d^\dagger c_{j\sigma'} + c_{j\sigma'}^\dagger d\big)\Big\rangle \\ &+ i\Big\langle\big(d^\dagger c_{j\sigma'} + c_{j\sigma'}^\dagger d\big)\cdot\big(d^\dagger(\tau)c_{i\sigma}(\tau) + c_{i\sigma}^\dagger(\tau)d(\tau)\big)\Big\rangle.\end{aligned}$$

If we assume the d-fermion orbital to be occupied, it follows that $\langle d^\dagger(\tau)d\rangle \neq 0$ and $\langle d(\tau)d^\dagger\rangle = 0$. Hence, the above equation simplifies to

$$\chi_{ij}^{\sigma\sigma'}(\tau) = -i\Big\langle d^\dagger(\tau)d\,c_{i\sigma}(\tau)c_{j\sigma'}^\dagger\Big\rangle + i\Big\langle d^\dagger d(\tau)c_{j\sigma'}c_{i\sigma}^\dagger(\tau)\Big\rangle. \tag{3.11}$$

Wick's theorem [74] can be used to write the four-point correlators in terms of a combination of two-point correlators. The only non-zero two-point correlators are $\langle d^\dagger(\tau)d\rangle$, $\langle c_i(\tau)c_j^\dagger\rangle$, $\langle d^\dagger d(\tau)\rangle$ and $\langle c_j c_i^\dagger(\tau)\rangle$. It then follows that

$$\chi_{ij}^{\sigma\sigma'}(\tau) = -i\left\langle d^\dagger(\tau)d\right\rangle\left\langle c_{i\sigma}(\tau)c_{j\sigma'}^\dagger\right\rangle + i\left\langle d^\dagger d(\tau)\right\rangle\left\langle c_{j\sigma'}c_{i\sigma}^\dagger(\tau)\right\rangle, \tag{3.12}$$

where $\left\langle d^\dagger(\tau)d\right\rangle$ and $\left\langle d^\dagger d(\tau)\right\rangle$ equal $e^{i\epsilon_d\tau}$ and $e^{-i\epsilon_d\tau}$, respectively. Finally, we arrive at

$$\chi_{ij}^{\sigma\sigma'}(\tau) = -ie^{i\epsilon_d\tau}\left\langle c_{i\sigma}(\tau)c_{j\sigma'}^\dagger\right\rangle + ie^{-i\epsilon_d\tau}\left\langle c_{j\sigma'}c_{i\sigma}^\dagger(\tau)\right\rangle. \tag{3.13}$$

The above relation can be represented in the equivalent form:

$$\chi_{ij}^{\sigma\sigma'}(\tau) = \sin\lambda\langle\{c_{i\sigma}(\tau), c_{j\sigma'}^\dagger\}\rangle - i\cos\lambda\langle[c_{i\sigma}(\tau), c_{j\sigma'}^\dagger]\rangle, \tag{3.14}$$

where $\lambda = \epsilon_d\tau$. Since the energy of the d-fermion ϵ_d is arbitrary, one may vary the phase λ to recover two independent Green's functions. By setting $\lambda = \pi/2$ one obtains the retarded Green's function given by the anti-commutator, while the choice $\lambda = 0$ leads to the so-called Keldysh correlator expressed via the commutator of two fermion operators. Thereby, ϵ_d reflects a flexible control parameter used to interpolate between different correlators via the phase $\lambda = \epsilon_d\tau$.

From here one may find a formal expression the anti-commutator in the form of a derivative with respect to ϵ_d, namely

$$\langle\{c_{i\sigma}(\tau), c_{j\sigma'}^\dagger\}\rangle = \frac{1}{\tau}\frac{\partial}{\partial\epsilon_d}\chi_{ij}^{\sigma\sigma'}(\tau)\Big|_{\epsilon_d=0}. \tag{3.15}$$

However, for a practical realization of the Green's function quantum circuit (see Sec. 4) we use the following trick: one measures $\chi_{ij}(\tau)$ both for ϵ_d and $(-\epsilon_d)$ successively. Then a combination of those two measurements yields

$$\langle\{c_{i\sigma}(\tau), c_{j\sigma'}^\dagger\}\rangle = \frac{\chi_{ij}^{\sigma\sigma'}(\tau,\epsilon_d) - \chi_{ij}^{\sigma\sigma'}(\tau,-\epsilon_d)}{2\sin(\epsilon_d\tau)}, \tag{3.16}$$

with ϵ_d being a free parameter which can be adjusted to optimize the quality of the measurement. In the limit $\epsilon_d \to 0$ one also recovers Eq. (3.15). Note, that Eq. (3.16) becomes exact under the assumption of a weak perturbation, $\Phi \to 0$, at any ϵ_d, which as we have found can be relaxed to $\Phi \lesssim 1/2$ in practical implementations.

When it comes to the actual measurement protocol using the outlined linear response scheme, it is advantageous to perform the measurements in the Majorana basis and use the relation Eq. (2.3) to reconstruct the Green's function of complex fermions afterwards. As an example, let us consider the measurement of the correlator of two Hermitian operators $x_{i\sigma}(\tau)$ and $y_{j\sigma'}$. To this end we introduce two Majorana fermions, $x_d = d + d^\dagger$ and $y_d = i(d - d^\dagger)$, associated with the auxiliary d-fermion and define hopping operators as follows, cf. Eq. (2.6)

$$A_i^\sigma = \tfrac{i}{2}x_{i\sigma}\,x_d, \quad A_j^{\sigma'} = \tfrac{i}{2}y_{j\sigma'}\,x_d. \tag{3.17}$$

Repeating the steps leading to the intermediate result Eq. (3.12), one finds that for such choice of hopping operators $\chi_{ij}^{\sigma\sigma'}(\tau)$ changes to

$$\begin{aligned}\chi_{ij}^{\sigma\sigma'}(\tau) &= -\tfrac{i}{4}\big\langle x_d(\tau)x_d\big\rangle\big\langle x_{i\sigma}(\tau)y_{j\sigma'}\big\rangle \\ &\quad +\tfrac{i}{4}\big\langle x_d x_d(\tau)\big\rangle\big\langle y_{j\sigma'}x_{i\sigma}(\tau)\big\rangle. \end{aligned} \tag{3.18}$$

Additionally, the correlator of an auxiliary Majorana fermion becomes $\langle x_d(\tau)x_d\rangle = e^{i\epsilon_d\tau}$. This means that for the Green's functions of Majorana operators we can use exactly the same final relation Eq. (3.14). In particular, the retarded correlator reads

$$\frac{1}{4}\langle\{x_{i\sigma}(\tau), y_{j\sigma'}\}\rangle = \chi_{ij}^{\sigma\sigma'}(\tau)\Big|_{\epsilon_d\tau=\pi/2}. \tag{3.19}$$

For the later purpose it is advantageous to rewrite the above relation as

$$\frac{1}{2}\langle\{x_{i\sigma}(\tau), y_{j\sigma'}\}\rangle = \frac{\langle ix_{i\sigma}x_d\rangle_\Phi(t,\epsilon_d)}{\sin\Phi_j^{\sigma'}}\Bigg|_{\epsilon_d\tau=\pi/2}, \tag{3.20}$$

where $\langle\ldots\rangle_\Phi$ refers to an average in the presence of a perturbation. Within the linear response theory framework the denominator needs to be substituted by just $\Phi_j^{\sigma'}$. In this case the relation Eq. (3.20) follows from Eqs. (3.7) and (3.19), where $\langle A_i^\sigma\rangle = \frac{i}{2}\langle ix_{i\sigma}x_d\rangle_\Phi$ plus we note that $\langle A_i^\sigma\rangle$ vanishes in the absence of perturbation. The equation becomes exact under weak perturbations as $\sin\Phi_j^{\sigma'} \to \Phi_j^{\sigma'}\big|_{\Phi_j^{\sigma'}=0}$. Stronger perturbations bring us into the non-linear regime, in which Eq. (3.20) can be recovered for arbitrary $\Phi_j^{\sigma'}$ ([75]).

We are now in a position to present the quantum circuit (see Fig. 3.7), which accomplishes the measurement of the correlator, Eq. (3.20).

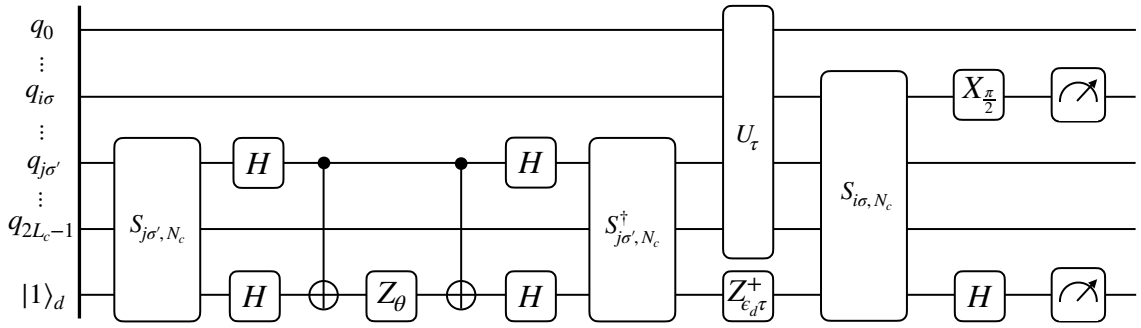

Figure 3.7: Measurement of the correlator $\langle\{x_{i\sigma}(\tau), y_{j\sigma'}(0)\}\rangle$. The unitary U_τ refers to the Trotterized evolution under the Hubbard cluster Hamiltonian Eq. (1.1). While the Z-rotation with the angle $\theta = \Phi_j^{\sigma'}$ is due to perturbation, the $Z^\dagger$-rotation with the angle $\epsilon_d\tau$ accounts for a free evolution of the d-fermion. The number of sites is L_c.

3.2.2.3 Quantum circuit to the direct measurement

Right after the initialization of a quantum computer to the ground state with the help of VHA (not shown), we apply the perturbation with the potential $V(\tau)$. It can be achieved in

one Trotter step yielding the unitary

$$\exp\left(\tfrac{1}{2}\Phi_j^{\sigma'} y_{j\sigma'}\, x_d\right) = S^{\dagger}_{j\sigma',N_c}\, \exp\left(-\tfrac{i}{2}\Phi_j^{\sigma'} X_{j\sigma'} X_{N_c}\right)\, S_{j\sigma',N_c}. \tag{3.21}$$

Its circuit representation is analogous to the one describing the evolution under the hopping term, see Fig. 2.1. In this context, it entangles the ancilla qubit used to represent the d-fermion with the qubits' states representing the cluster. Subsequent independent evolutions of the cluster and the d-fermion are then followed by the measurement of an operator $A_i^{\sigma} = \frac{i}{2} x_{i\sigma} x_d$. The way to average such operator has been described in subsection 3.1.2: via a few unitary transformations $\langle A_i^{\sigma} \rangle$ can be related to the average parity of two qubits, $\langle Z_{i\sigma} Z_{N_c} \rangle$, see Fig. 3.2.

Our primary focus in this works is on the retarded Green's function given by the anti-commutator Eq. (3.20), since the latter eventually enters into the VCA scheme outlined in Sec. 6. However, the full set of possible Green's functions can be evaluated using the proposed algorithm. For instance, for the Keldysh correlator of Majoranas one can write

$$-\frac{i}{2}\langle [x_{i\sigma}(\tau), y_{j\sigma'}] \rangle = \left. \frac{\langle i x_{i\sigma} x_d \rangle_{\Phi}(t, \epsilon_d)}{\sin \Phi_j^{\sigma'}} \right|_{\epsilon_d \tau = 0}. \tag{3.22}$$

Then other correlators, such as $g_{ij}^{\sigma\sigma'}(\tau)$ defined in Eq. (2.4), can be reconstructed from the retarded and Keldysh Green's functions. Additionally, the best choice for the strength of the perturbation is $\Phi_j^{\sigma'} = \pi/2$, which leads to the strongest (non-linear) response and is used for demonstrating the quantum algorithm in Ch. 4.

3.3 Comparing applicability of fermionic mappings

Amongst all known mappings that encode fermions into qubits, the Jordan-Wigner scheme is one of the more prominent examples. It is known for its simplicity, straightforwardness and Pauli strings. In low-dimensional, small systems, the latter hardly emerge. Yet, unfortunate cases of nearest neighbor interactions, cf. Fig. 3.3, may trigger local interactions that propagate through the full system in form of Z-strings.

As these additional terms contribute to the error of quantum demonstrations, it is often advised to find a mapping that balances out qubit overhead, the ability to preserve locality and the overall adequacy of a particular mapping to a particular problem.

For the direct measurement method that is being presented, the Jordan-Wigner mapping works fine. Not only that, but other, more locality-preserving mappings, [40, 65], work as well. Famously, the Bravyi-Kitaev mapping, [39], is less prone to non-locality. In this landmark paper, it was discussed that only products (or sums thereof) of an even number of fermionic operators spans the algebra of physical operators. It follows that for a number of more advanced mappings, single Majorana fermion operators — as required by the Hadamard test — cannot be constructed.

It is this fact that renders the method of a direct measurement of a response function more versatile as it can be applied to mappings beyond Jordan-Wigner. Larger systems can benefit from this scheme by suppressing the emergence of Pauli strings. Note, that the math is not carried out in this thesis. The interested reader is encouraged to view the detailed algebra and the adapted quantum circuits in Ref. [75].

3.4 Quantum advantage

The complete matrix for the Green's function, made up of two-point time correlations functions Eq. (0.14), has a dimension of $2L_c \times 2L_c$, where L_c is the number of sites in a cluster. While the final matrix size remains agnostic to either classical or quantum platforms, the classical approach incurs a drastic overhead in matrix multiplication, significantly outpaced by its quantum analog.

To showcase the quantum advantage, we start off with the classical case. Following [76], the Lehmann representation Eq. (0.13) is broken down to

$$G'(\omega) = Q' g(\omega) Q'^{\dagger}. \tag{3.23}$$

Here, Q' holds the electron-like and hole-like amplitudes with dimension $2L_c \times 16^{L_c}$ and $g(\omega)$ is a square matrix of dimension $16^{L_c} \times 16^{L_c}$, cf. Fig. 3.8.

The multiplication of exponentially scaling matrices necessary to evaluate the full cluster GF makes the classical case impractical. In contrast, the quantum schemes require measurements that scale quadratically in the number of sites L_c.

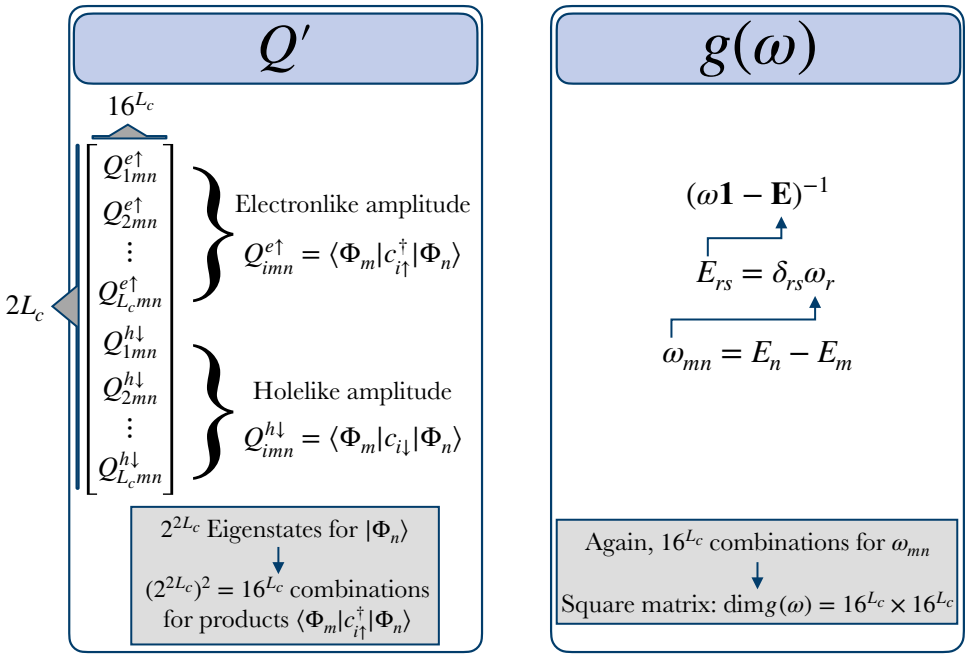

Figure 3.8: Anatomy of exponentially scaling matrices Q' and $g(\omega)$. Q' is a $2L_c \times 16^{L_c}$ matrix, $g(\omega)$ is a $16^{L_c} \times 16^{L_c}$ matrix. Not to mention that the eigenstates in Q' need to be extracted as well.

4 Two-site dimer model

In this section we introduce a two-site dimer [77] (, i. e., a four-orbital dimer) that serves as our toy model for which we evaluate the Green's function. Following the general framework outlined in Sec. 6, it can be seen as the smallest non-trivial cluster, so that the VCA is able to deliver physically reasonable results. Specifically, such minimal cluster is sufficient to reproduce the Mott insulating transition in the Hubbard model. On the other hand, in order to recover the d-wave superconducting phase, one needs at least four sites per cluster [76].

The two-site dimer model consists of a Hubbard site that is coupled to a bath site. Its Hamiltonian at half-filling given by

$$H' = H_0 + H_U = -t \sum_{\sigma} (c_\sigma^\dagger b_\sigma + b_\sigma^\dagger c_\sigma) + \frac{U}{2}(n_c^2 - 2n_c), \tag{4.1}$$

where t is the hopping energy and U is the Coulomb repulsion. The field operators $c_\sigma^\dagger, c_\sigma$ respectively create or destroy a fermion with spin σ at the Hubbard site, while $b_\sigma^\dagger, b_\sigma$ respectively create or destroy a fermion with spin σ at the bath site and $n_c = \sum_\sigma c_\sigma^\dagger c_\sigma$. Lastly, the linear n_c term in H_U stems from a chemical potential $\mu = U$ at half-filling. A qubit ordering is shown in Fig. 4.1 and is chosen in a way that allows for decreasing circuit depth, see section 4.1.

Investigating the dimer at half-filling (two out of four orbitals are occupied) allows us to concentrate on just six out of 16 possible state configurations. With $|0\rangle$ being the vacuum state, following states $|1\rangle, |2\rangle, \ldots, |6\rangle$ are possible as two electrons reside at the dimer:

$$\begin{aligned} |1\rangle &= c_\downarrow^\dagger c_\uparrow^\dagger |0\rangle, \quad |2\rangle = c_\downarrow^\dagger b_\uparrow^\dagger |0\rangle, \quad |3\rangle = b_\downarrow^\dagger b_\uparrow^\dagger |0\rangle \\ |4\rangle &= b_\downarrow^\dagger c_\uparrow^\dagger |0\rangle, \quad |5\rangle = b_\uparrow^\dagger c_\uparrow^\dagger |0\rangle, \quad |6\rangle = b_\downarrow^\dagger c_\downarrow^\dagger |0\rangle. \end{aligned} \tag{4.2}$$

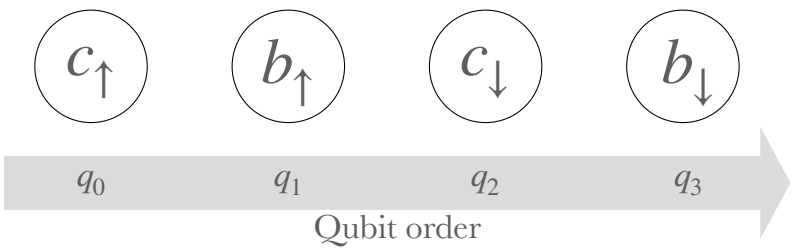

Figure 4.1: Indexing qubits over two Hubbard orbitals and two bath orbitals.

In matrix form, the Hamiltonian (Eq. (4.1)) thus reads

$$H' = -\begin{pmatrix} 0 & -t & 0 & t & 0 & 0 \\ -t & \frac{U}{2} & -t & 0 & 0 & 0 \\ 0 & -t & 0 & t & 0 & 0 \\ t & 0 & t & \frac{U}{2} & 0 & 0 \\ 0 & 0 & 0 & 0 & \frac{U}{2} & 0 \\ 0 & 0 & 0 & 0 & 0 & \frac{U}{2} \end{pmatrix}, \tag{4.3}$$

with the ground state energy

$$E_0 = -\frac{1}{4}(U + \sqrt{U^2 + 64t^2}), \tag{4.4}$$

corresponding to the eigenstate

$$|\Psi\rangle \propto C(|1\rangle + |3\rangle) + |2\rangle + |4\rangle), \quad C = \frac{\sqrt{U^2 + 64t^2} - U}{8t}, \tag{4.5}$$

up to a normalization factor. Lastly, we find the expectation values of H_0 and H_U to be

$$\langle H_0 \rangle = -\frac{16t^2}{\sqrt{U^2 + 64t^2}} \tag{4.6}$$

and

$$\langle H_U \rangle = -\frac{U}{4}\left(1 + \frac{U}{\sqrt{U^2 + 64t^2}}\right). \tag{4.7}$$

As required by linear response theory, we need to start from an equilibrium state, e. g., the ground state. Consequently, we present a route to find the ground state via the VHA.

4.1 Ground state preparation

For the sake of finding the ground state of the dimer system, we employ a technique known as the variational Hamiltonian ansatz [70]. Starting from the ground state of the cluster $|\Psi_0\rangle$ in the non-interacting limit $U = 0$, we aim to find the interacting system's ground state $|\Psi\rangle$ as

$$|\Psi(\alpha, \beta)\rangle = \prod_{j=1}^{p} e^{i\beta_k H_0} e^{-i\alpha_k H_U} |\Psi_0\rangle \tag{4.8}$$

where $\alpha_j, \beta_j \in \mathbb{R}$ are the variational parameters.

The ground state $|\Psi_0\rangle$ is a Slater determinant. For instance, Eq. (4.5) at $U = 0$ can be written in terms of two f-fermions,

$$|\Psi_0\rangle = f_\downarrow^\dagger f_\uparrow^\dagger |0\rangle, \qquad f_\sigma^\dagger = \frac{1}{\sqrt{2}}(c_\sigma^\dagger + b_\sigma^\dagger), \tag{4.9}$$

which are linear superpositions of operators b and c.

An initialization of the quantum chip in a Slater determinant state most generally can be constructed from an initial one, $|0, 0, ..., 0\rangle$, by the so-called Given's rotation [57]. However, for the two-fermion state (Eq. (4.9)) a much simpler circuit is sufficient. One can verify by direct inspection that the circuit shown in Fig. 4.2 transforms the vacuum state into $|\Psi_0\rangle$.

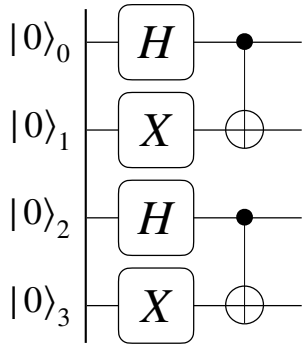

Figure 4.2: Quantum circuit to prepare a Slater determinant as a trial ansatz for the VHA.

Moreover, it is possible to find the exact matching between the trial and actual ground state functions already for the minimal depth VHA, i. e., with $p = 1$. Therefore, Fig. 4.3 shows the full circuit to prepare the ground state is a single sequence of the circuit shown in Fig. 4.2, followed by a variation of the hopping circuit, cf. Fig. 2.1 and finalized by a simpler variation of the repulsion circuit, Fig. 2.3.

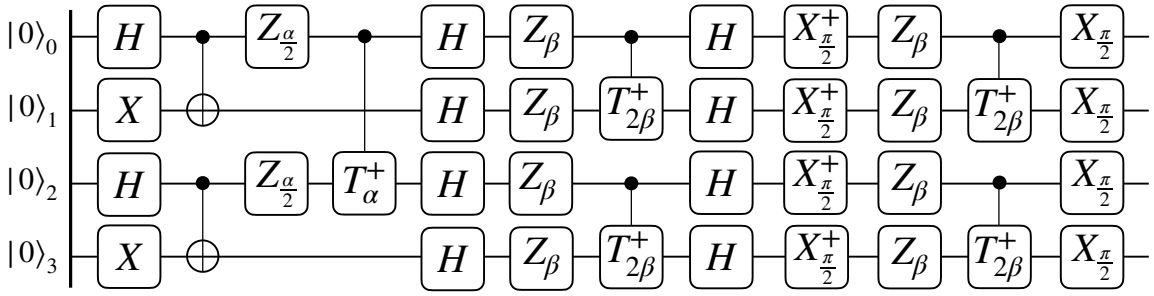

Figure 4.3: Reduced quantum circuit for finding the ground state of a correlated system. At the end of the circuit we are left with the interacting ground state of the two-site dimer.

At this point, we note that the evolution operator over a time step $\Delta\tau$ under the interaction Hamiltonian H_U, see Eq. (4.1), reads

$$U(\theta) = \mathrm{CNOT}^{(13)} \cdot \mathrm{R}_z^{(3)}\,(\theta/2) \cdot \mathrm{CNOT}^{(13)}, \tag{4.10}$$

with angle $\theta = U \cdot \Delta\tau$. A difference from the repulsion circuit on Fig. 2.3 comes from the extra term Un_c in the present choice of H_U, which effectively leads to the reduction of two single-qubit Z-rotation gates.

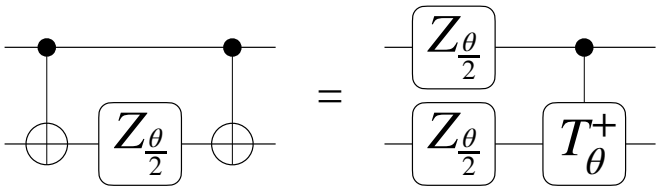

Figure 4.4: Circuit identity as used in the two-site dimer.

Furthermore, if one of the natural two-qubit gates on the hardware is a controlled-phase gate, $\mathrm{CT}(\theta)$, then the unitary in Eq. (4.10) can be simplified to

$$U(\theta) = \mathrm{R}_{\mathrm{z}}^{(1)}(\theta/2) \cdot \mathrm{R}_{\mathrm{z}}^{(3)}(\theta/2) \cdot \mathrm{CT}^{(13)}(-\theta), \tag{4.11}$$

up to a global phase. The equivalence of the two circuits in Eqs. (4.10) and (4.11) for $U(\theta)$ is presented in Fig. 4.4.

Comparing Fig. 4.3 to Figs. 2.1 and 2.3, we reach a reduction of two two-qubit gates mainly based on the transformation shown in Fig. 4.4 and the choice of the qubit ordering, Fig. 4.1, further suppressing Pauli strings to enter the circuit. Finally, the variational energy reads

$$E(\alpha, \beta) = -2t \cos\frac{\alpha}{2} - \frac{U}{4}\Big(1 - \sin\frac{\alpha}{2}\sin 4\beta\Big), \tag{4.12}$$

which depends on just two parameters, α and β. Fig. 4.5 shows the corresponding (numerical) energy landscape alongside the analytic energies in Fig. 4.6.

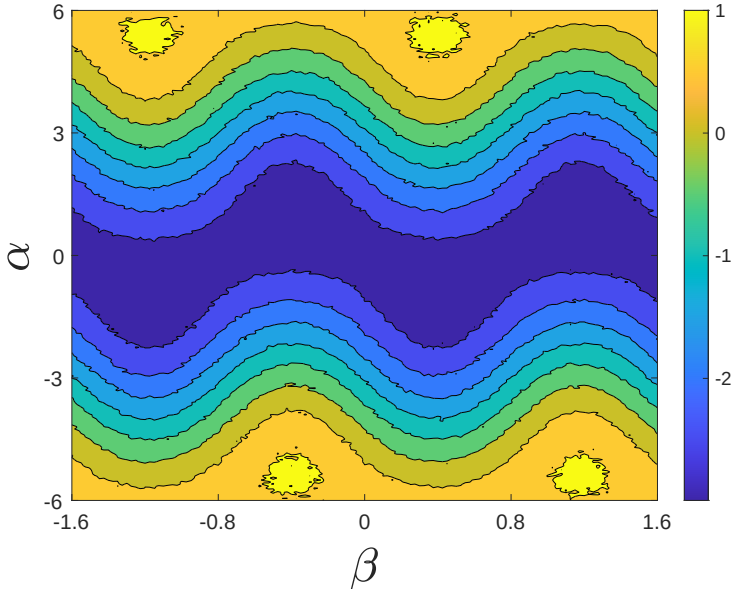

Figure 4.5: Energy landscape for the two-site dimer for finding its ground state via the variational Hamiltonian ansatz with angles α and β shown for $t = 1$ and $U = 4$. The energies were evaluated on Qiskit's noisy *Aer* simulator of the *FakeKolkataV2()* backend, an open-access simulator of the corresponding superconducting device *ibmq_kolkata* provided by IBM. The optimum is lying very close to theoretical values $\alpha_* = -0.92$ and $\beta_* = 0.39$ found from Eq. (4.12).

The analytical landscape is shown in Fig. 4.6. A direct comparison shows slight discrepancies in the amplitudes. The circuit is shallow, yet the noise from the few gates affect the energy measurements. More importantly, the qualitative direction is accurate. After all, one seeks the angles that yield the interacting ground state.

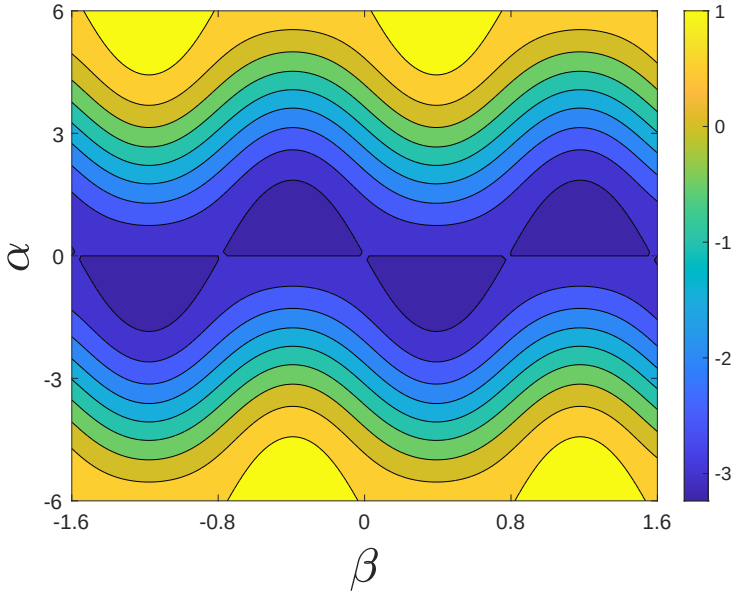

Figure 4.6: Analytical energy landscape for the two-site dimer according to Eq. (4.12).

4.2 Analytical formulae for the Green's function

Next we discuss the analytical results for the Green's functions of the two-site model in order to benchmark them with our circuit simulations, reviewed in the next subsection. Following the ordering of fermion states under Jordan-Wigner mapping shown in Fig. 4.1, we introduce a set of eight Majorana operators $\{x_n, y_n\}$ so that

$$\begin{aligned} c_\uparrow &= \tfrac{1}{2}(x_0 - iy_0), \qquad b_\uparrow = \tfrac{1}{2}(x_1 - iy_1), \\ c_\downarrow &= \tfrac{1}{2}(x_2 - iy_2), \qquad b_\downarrow = \tfrac{1}{2}(x_3 - iy_3), \end{aligned} \tag{4.13}$$

with n being a composite index accounting for both site and spin. Correlation functions of interest take the form given by Eqs. (2.3) and (2.4). Because of spin symmetry we find them to be block-diagonal w. r. t. spin indices,

$$ig^{\uparrow\uparrow}(\tau) = \begin{pmatrix} \langle x_0(\tau)x_0(0)\rangle & \langle x_0(\tau)y_1(0)\rangle \\ \langle y_1(\tau)x_0(0)\rangle & \langle y_1(\tau)y_1(0)\rangle \end{pmatrix}, \tag{4.14}$$

and

$$ig^{\downarrow\downarrow}(\tau) = \begin{pmatrix} \langle x_2(\tau)x_2(0)\rangle & \langle x_2(\tau)y_3(0)\rangle \\ \langle y_3(\tau)x_2(0)\rangle & \langle y_3(\tau)y_3(0)\rangle \end{pmatrix}, \tag{4.15}$$

with two blocks being mutually equal, $g^{\uparrow\uparrow}(\tau) = g^{\downarrow\downarrow}(\tau)$. Other non-zero correlators follow from the symmetries

$$\begin{aligned} \langle x_i(\tau)x_i(0)\rangle &= \langle y_i(\tau)y_i(0)\rangle, \qquad \forall\, i \\ \langle x_i(\tau)y_{i+1}(0)\rangle &= \langle x_{i+1}(\tau)y_i(0)\rangle, \quad i = 0, 2. \end{aligned} \tag{4.16}$$

Additionally, the self-adjoint property of Majorana operators implies that

$$\langle x_i(\tau)y_j(0)\rangle^* = \langle y_j(0)x_i(\tau)\rangle, \tag{4.17}$$

and the same for $x-x$ and $y-y$ correlators. Therefore, the retarded correlator reads

$$\langle\{x_i(\tau), y_j(0)\}\rangle = 2\mathrm{Re}\,\langle x_i(\tau)y_j(0)\rangle, \quad \tau > 0. \tag{4.18}$$

We can evaluate the above correlation functions exactly using the Lehmann representation. Starting from $iG^{>}(\tau) = \langle\Psi_*|U^\dagger(\tau)x_iU(\tau)y_j|\Psi_*\rangle$, where $|\Psi_*\rangle$ is the ground state, we use the eigenstate decomposition of the evolution operator, $U(\tau) = \sum_m^{2^D} |m\rangle e^{-iE_mt}\langle m|$, with $D = 4^{L_c}$ being the Hilbert space dimension of a cluster. It then follows that $iG^{>}(\tau) = \sum_m^D e^{-iE_0t}\langle\Psi_*|x_i|m\rangle e^{-iE_mt}\langle m|y_j|\Psi_*\rangle$. The eigenstates $|m\rangle$ can be obtained by exact diagonalization of H', cf. Eq. (4.1), which renders the two-site dimer Green's function amenable to analytic treatment. The correlation functions evaluated in this manner read

$$\langle x_0(\tau)x_0(0)\rangle = e^{-\frac{i}{4}\tau U_2}\left(\cos\frac{\tau U_1}{4} - \frac{i\left(U^2-32t^2\right)}{U_1U_2}\sin\frac{\tau U_1}{4}\right), \tag{4.19}$$

$$\langle x_1(\tau)x_1(0)\rangle = e^{-\frac{i}{4}\tau U_2}\left(\cos\frac{\tau U_1}{4} + \frac{i\left(U^2+32t^2\right)}{U_1U_2}\sin\frac{\tau U_1}{4}\right) \tag{4.20}$$

and

$$\langle x_0(\tau)y_1(0)\rangle = 4e^{-\frac{i}{4}\tau U_2}\left(\frac{2it}{U_2}\cos\frac{\tau U_1}{4} - \frac{t}{U_1}\sin\frac{\tau U_1}{4}\right), \tag{4.21}$$

where two additional energy scales,

$$U_1 = \sqrt{U^2+16t^2}, \quad U_2 = \sqrt{U^2+64t^2}, \tag{4.22}$$

were introduced to shorten the results.

4.3 Quantum circuits for the direct measurement of the two-site dimer Green's function

In accordance to section 3.2.2, we provide quantum circuits for the direct measurement of the Green's function. To implement the unitary evolution operator U_τ, one applies the Trotterization scheme with a duration of a single step being $\Delta\tau$. The one-step evolution operator can be constructed following the same sequence of gates used in the VHA circuit, see Fig. 4.5, with angles $\alpha = U\Delta\tau$ and $\beta = -t\Delta\tau$.

4.3.1 Correlator circuits

The y_2–y_2 correlator is directly measured when employing the circuit shown in Fig. 4.7. In turn, circuits for measuring y_3–y_3 and y_3–x_2 correlators are shown in Fig. 4.8 and Fig. 4.9, respectively.

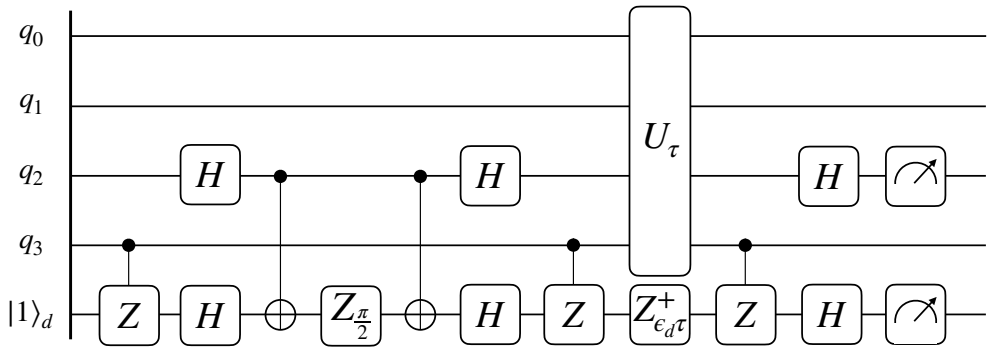

Figure 4.7: Circuit for evaluating the $\langle\{y_2(\tau), y_2(0)\}\rangle$ correlator.

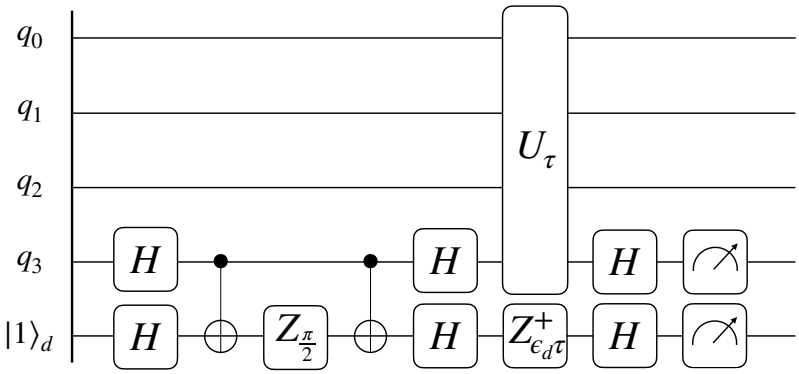

Figure 4.8: Circuit for evaluating the $\langle\{y_3(\tau), y_3(0)\}\rangle$ correlator.

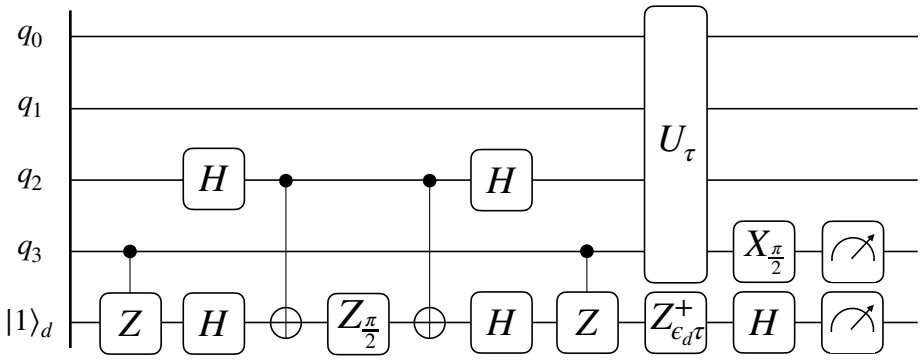

Figure 4.9: Circuit for evaluating the $\langle\{x_3(\tau), y_2(0)\}\rangle$ correlator.

The input state to the circuits is the interacting ground state as per variational Hamiltonian ansatz. The common feature is the application of a perturbative hopping to the input state, which is supposed to be weak enough to expect a linear response in the parity measurement.

4.3.2 Complete evaluation of the dimer Green's function

We start off by presenting the full set of tools to evaluate the GF, from initializing the trial wave function to the parity measurement in Fig. 4.10. This shall serve as a recipe for the evaluation of any correlator of the form $x_{i\sigma}(\tau)y_{j\sigma'}(0)$.

Subsequently, we present the evaluation for one particular correlator $x_3(\tau)x_3(0)$ from scratch. The subscript corresponds to the the fourth orbital, cf. Fig. 4.1, e. g., to the spin-down bath orbital.

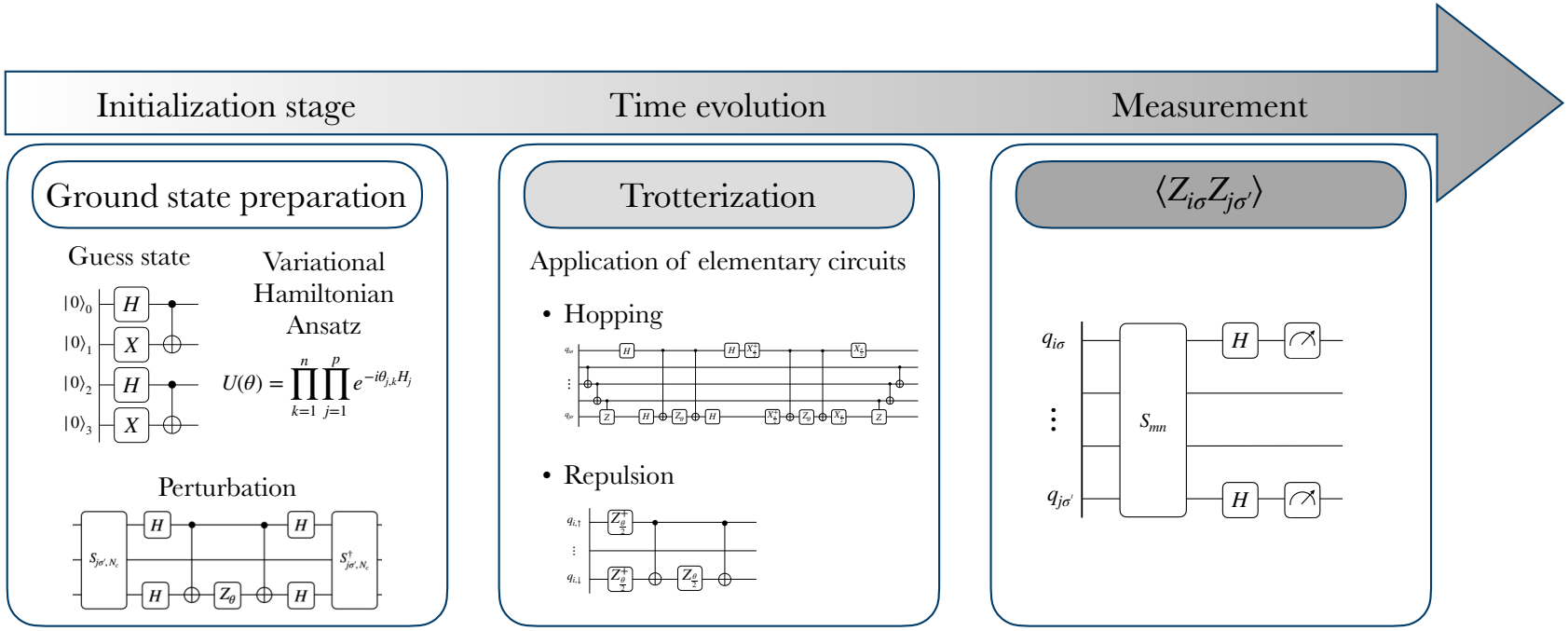

Figure 4.10: The complete tool set for evaluating the cluster's Greens function. *Initialization stage (left):* A non-interacting trial wave function is engineered. Variational Hamiltonian Ansatz gives the interacting ground state of the two-site dimer. Finally, the system is perturbed via a hopping process. *Time evolution (center):* The system is evolved in time via Trotterization. To that end, we alternate between applications of hopping and repulsion circuits. *Measurement (right)*: Finally, a parity measurement of the target qubits i, j is performed.

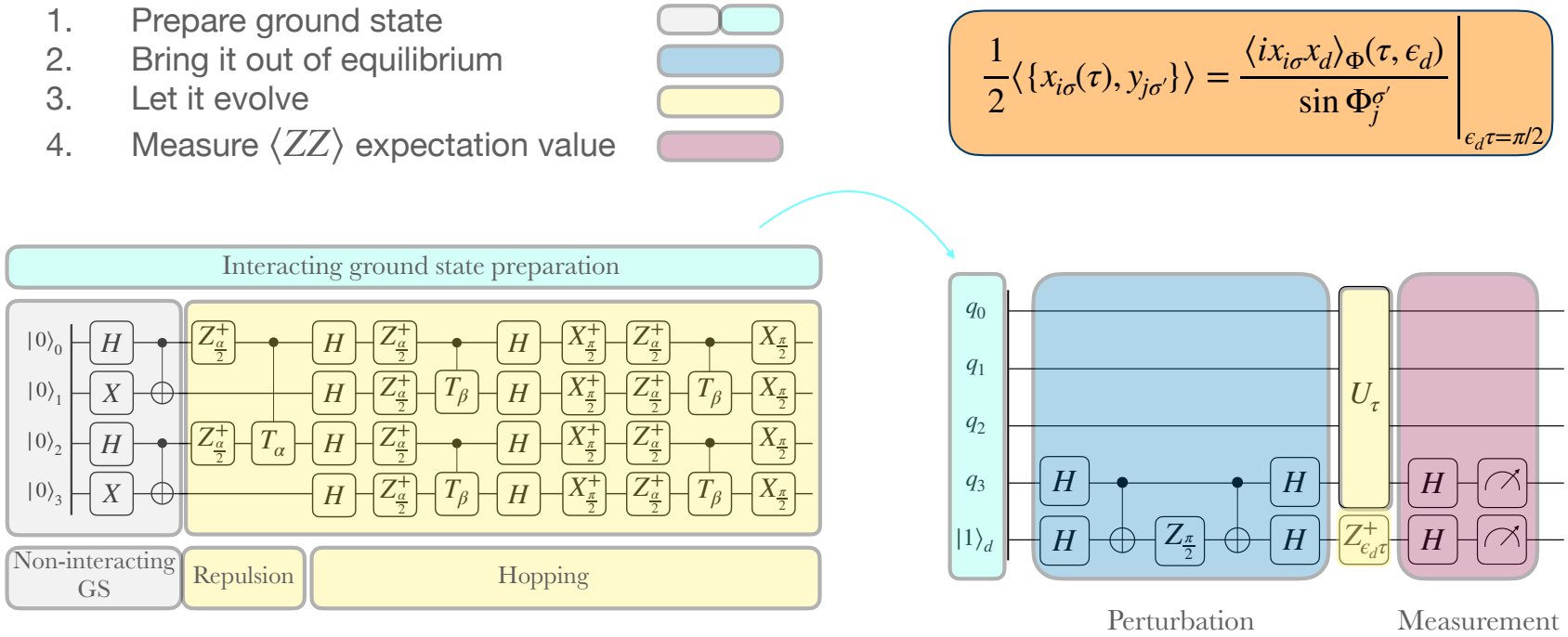

Figure 4.11: The complete process of evaluating the cluster's Greens function, exemplified on the $x_3(\tau)x_3(0)$ correlator. *Left:* The interacting ground state (teal) is prepared from a Slater determinant (gray box) and a single sequence of repulsion and hopping circuit (yellow boxes), according to the optimal angles via variational Hamiltonian ansatz. *Right:* The ground state orbitals 3 and d are target to a perturbation, representing a hopping as per Eq. (3.20) (orange box, top right). Note, that while the d orbital is always part of the perturbation and measurement, the perturbed system orbital does not necessarily equal the measured system orbital, cf. Fig. 4.9. It follows a time evolution, done by pairwise applications of repulsion and hopping circuits (see yellow box). The number of pairwise applications equals the number of Trotter steps. Finally, a parity measurement on orbital 3 and orbital d is performed. The result is the element $x_3(\tau)x_3(0)$, that together with other correlators constitute the Green's function.

4.4 Results and discussion

We show data points for the Green's function after 25 Trotter steps and plot these against the analytical Green's function, see Eqs. (4.19)–(4.21). The chosen parameters are $t = 1$, $U = 4t$, $\Phi = \pi/2$ and $\epsilon_d \tau = \pi/2$. The results are shown in Fig. 4.12.

While a statevector simulation delivers exact results for any perturbation, a discrepancy in noisy quantum circuit simulation results and the analytical curves can be observed, that grows larger with increased duration τ. This is due to a combination of gate and measurement errors (see Ch. 5) and Trotter errors that accumulate over time (not shown). In practical simulations, the perturbation was set to $\Phi_j^\sigma = \pi/2$ as it has triggered the strongest (non-linear) response.

It can be seen, that 25 Trotter steps are sufficient to have a decent overlap of measurement points and the analytic correlator up to time $\tau \sim 8$. Single-qubit gates take typical operation times of 20ns, two- and three-qubit gates may be designed with operation times of typically 100ns. It is thus crucial to reduce multi-qubit gates as much as possible to keep operation time short and quantum state fidelity large. After all, such gates are the major contributors to errors in the computation. In the subsequent chapter 5, the errors associated with the one- and two-qubit gates are listed. The effective qubits were drafted such that a practical balance of gate errors, qubit vicinity, readout errors and coherence times is achieved, cf. Fig. 5.1.

In terms of the two-qubit gate count, the new algorithm is comparable to the third stage of the Hadamard test, Sec. 3.2.1. The only variation in the number of such gates comes from the time evolution, which is similar to both the Hadamard test as well as the direct measurement ansatz. The number of Trotter steps determines the depth of the quantum circuit associated with the unitary $U(\tau)$.

The second stage Hadamard test suffers from the evolution being controlled. In principle, all n-qubit gates become $n + 1$-qubit gates. In some cases, symmetry arguments lead to identification of gates, that are not subject to an increase in gate complexity.

As outlined in 3.4, the number of sites on a cluster significantly affects the number of required classical operations in the Lehmann Green's function. A multiplication of matrices that grow exponentially with respect to the number of sites L_c is only possible for small systems. A two-site dimer is sufficiently small to be analytically solvable, gifting us with the analytic results Eqs. (4.19, 4.20, 4.21). On the contrary, the number of required quantum measurements scales quadratically in the number of sites L_c within the cluster and the number of qubits scales linearly in L_c.

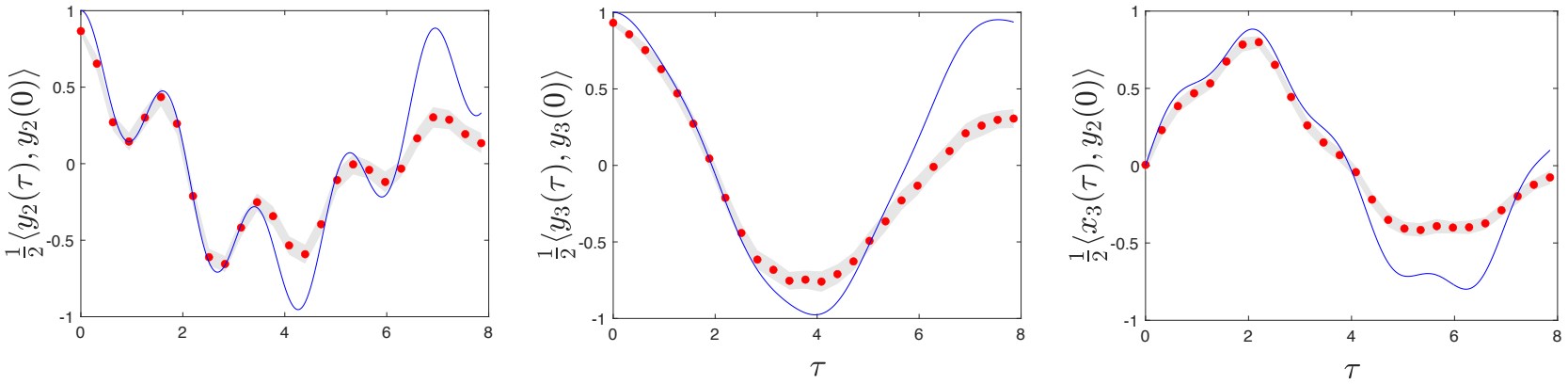

Figure 4.12: Correlators y_2–y_2, y_3–y_3 and x_3–y_2 (from left to right) evaluated in 25 Trotter steps (red dots) of the duration $\Delta\tau = \frac{\pi}{10}$. A shaded area (gray) indicates the standard deviation stemming from gate errors, measurement errors and Trotter errors over 100 instances of executing quantum circuits. The solid blue curves correspond to the analytical results, cf. Eqs. (4.19)–(4.21), where we account for the symmetry relations Eq. (4.16). System parameters are chosen to be $t = 1$ and $U = 4t$. The correlators were evaluated on Qiskit's noisy *Aer* simulator of the *FakeKolkataV2()* backend, an open-access simulator of the corresponding superconducting device *ibmq_kolkata* provided by IBM.

5 Implementation details

In this section we give details on the simulated quantum processor used for showcasing our proposed algorithm. Moreover, we give details on the execution and error mitigation schemes for the presented quantum circuits. Throughout this work, we have worked solely with Qiskit [78], an open-source software kit provided by IBM. Qiskit allows users to design and execute quantum software on either simulated quantum hardware, or on quantum hardware made available through IBM.

5.1 Simulated quantum processor

The demonstrations take place on the *FakeKolkataV2()* backend, resembling the characteristics of the *ibmq_kolkata* quantum device, consisting of 27 superconducting qubits. The layout of the chip as well as couplings between the qubits are depicted in Fig. 5.1. Five qubits required for executing proposed algorithm are highlighted in green, alongside their couplings.

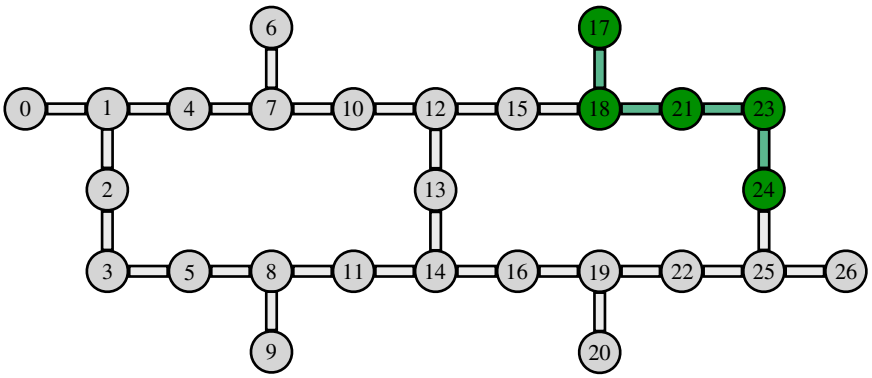

Figure 5.1: Layout of the *ibmq_kolkata* quantum device, consisting of 27 superconducting qubits and their couplings. The set of physical qubits $\{18, 17, 21, 23, 24\}$ (green) was used for demonstrating our algorithm.

For the following analysis, we will denote the simulated qubits as $q_p^{(l)}$, for which the exponent is the logical qubit number, and p is the number of the physical qubit, which arises from mapping logical to physical qubits. Let $\mathcal{L} = \{0, 1, 2, 3, 4\}$ be the set of logical qubits and $\mathcal{P} = \{18, 17, 21, 23, 24\}$ be the set of physical qubits. Then, a mapping from logical to physical qubits is performed via $f : \mathcal{L}_i \mapsto \mathcal{P}_i$, where i points to the ith element of the corresponding set.

At the time of performing the simulations, the device has the following set of basis gates: ID, X, SX, RZ and CX. In Tab. 5.1 one finds qubit calibration data at the time of the

	Frequency [GHz]	$T_1[10^{-5}\text{s}]$	$T_2[10^{-5}\text{s}]$
$q_{18}^{(0)}$	5.09	10.93	6.99
$q_{17}^{(1)}$	5.24	9.08	3.53
$q_{21}^{(2)}$	5.27	10.13	10.98
$q_{23}^{(3)}$	5.14	8.45	10.78
$q_{24}^{(4)}$	5.0	11.41	2.61

Table 5.1: Calibration data of simulated qubits $q_{\mathcal{P}_i}^{(\mathcal{L}_i)}$, at the time of the simulation.

simulation. Furthermore, Tab. 5.2 shows single-qubit gate errors and measurement errors. Note, that RZ is a virtual Z rotation and thereby has neither an error, nor a duration. Finally, Tab. 5.3 gives the CX errors to qubit pairs $(q_{\mathcal{P}_i}^{(\mathcal{L}_i)}, q_{\mathcal{P}_{i+1}}^{(\mathcal{L}_{i+1})})$.

	Single-qubit operation error (and duration)	
	$\{ID, X, SX\}$	Measurement
$q_{18}^{(0)}$	$1.98 \cdot 10^{-4}$ $(3.56 \cdot 10^{-8}\text{s})$	$7.4 \cdot 10^{-3}$ $(6.76 \cdot 10^{-7}\text{s})$
$q_{17}^{(1)}$	$4.22 \cdot 10^{-4}$ $(3.56 \cdot 10^{-8}\text{s})$	$6.1 \cdot 10^{-3}$ $(6.76 \cdot 10^{-7}\text{s})$
$q_{21}^{(2)}$	$2.59 \cdot 10^{-4}$ $(3.56 \cdot 10^{-8}\text{s})$	$6.8 \cdot 10^{-3}$ $(6.76 \cdot 10^{-7}\text{s})$
$q_{23}^{(3)}$	$1.73 \cdot 10^{-4}$ $(3.56 \cdot 10^{-8}\text{s})$	$7.9 \cdot 10^{-3}$ $(6.76 \cdot 10^{-7}\text{s})$
$q_{24}^{(4)}$	$1.65 \cdot 10^{-4}$ $(3.56 \cdot 10^{-8}\text{s})$	$5.3 \cdot 10^{-3}$ $(6.76 \cdot 10^{-7}\text{s})$

Table 5.2: Gate errors and execution durations.

5.2 Quantum simulation details

For performing noisy simulations, we employ Qiskit's *Aer*, a high performance simulator for executing quantum circuits within Qiskit. Next, we chose the *FakeKolkataV2()* backend, which is supposed to mimic the behavior of the quantum device *ibmq_kolkata*, as described in 5.1. These two ingredients allow for noisy simulations based on the *ibmq_kolkata* device with given gate fidelities, operations and durations. This is particularly useful to gauge the accuracy of results, if demonstrations took place on the real quantum device.

qubit pair	CX error (and duration)
$(q_{18}^{(0)}, q_{17}^{(1)})$	$1.62 \cdot 10^{-2}$ $(5.05 \cdot 10^{-7}\text{s})$
$(q_{17}^{(1)}, q_{21}^{(2)})$	$8.77 \cdot 10^{-3}$ $(4.91 \cdot 10^{-7}\text{s})$
$(q_{21}^{(2)}, q_{23}^{(3)})$	$5.39 \cdot 10^{-3}$ $(3.63 \cdot 10^{-7}\text{s})$
$(q_{23}^{(3)}, q_{24}^{(4)})$	$5.34 \cdot 10^{-3}$ $(2.84 \cdot 10^{-7}\text{s})$

Table 5.3: CX gate errors on qubit pairs $(q_{\mathcal{P}_i}^{(\mathcal{L}_i)}, q_{\mathcal{P}_{i+1}}^{(\mathcal{L}_{i+1})})$, at the time of the simulation.

5.2.1 Employment of error mitigation techniques

We made use of several error mitigation techniques [9], some of them are implemented natively in Qiskit. In particular, we have utilized

- measurement error mitigation,
- Pauli twirling,
- dynamical decoupling
- and zero-noise extrapolation.

The methods used for generating the results shown in Fig. 4.5 are readout error mitigation and dynamical decoupling with XX sequences on idle qubits.

On the other hand, the evaluation of correlators, Fig. 4.12, requires a more extensive use of described error mitigation techniques. The sequence of applied techniques is as follows.

One starts by Pauli twirling all of the two-qubit gates in a given circuit, and repeats this 99 times. We have now 100 Pauli twirled circuits associated with a given evolution time τ. In the spirit of zero noise extrapolation, we denote the target scaling factors as $F = [1.0, 1.5, 2.0, 2.5, 3.0]$. In a given circuit, each CNOT gate is being copied twice with respective probabilities $P(F) = [0, 0.25, 0.5, 0.75, 1]$. For instance, a scaling factor of 2.0 implies that the count of CNOT gates doubles. Since however back-to-back CNOTs merge into the identity (therefore altering the effective circuit), a practical route is to flip a coin at each CNOT gate for the chance of copying it twice. Since we have in total 100 Pauli circuits per experimental time τ, the sample size is large enough to justify such strategy. Of course, the empirical probabilities from the count of copied CNOT gates differs slightly from the respective theoretical probabilities in $P(F)$. Later on, the extrapolation will take the empirical probabilities as reference points, and not the ones from $P(F)$.

As a last step, the XX sequence on idle qubits is applied. All circuits are run and readout error mitigation is applied.

The individual evaluations are then extrapolated to the zero-noise level via a second-order polynomial. The 100 data points give rise to the standard deviations visible in Fig. 5.2. Finally, the shot number for all demonstrations was set to 4096, as Fig. 5.2 suggests this number balances out computational resources with accuracy of a result.

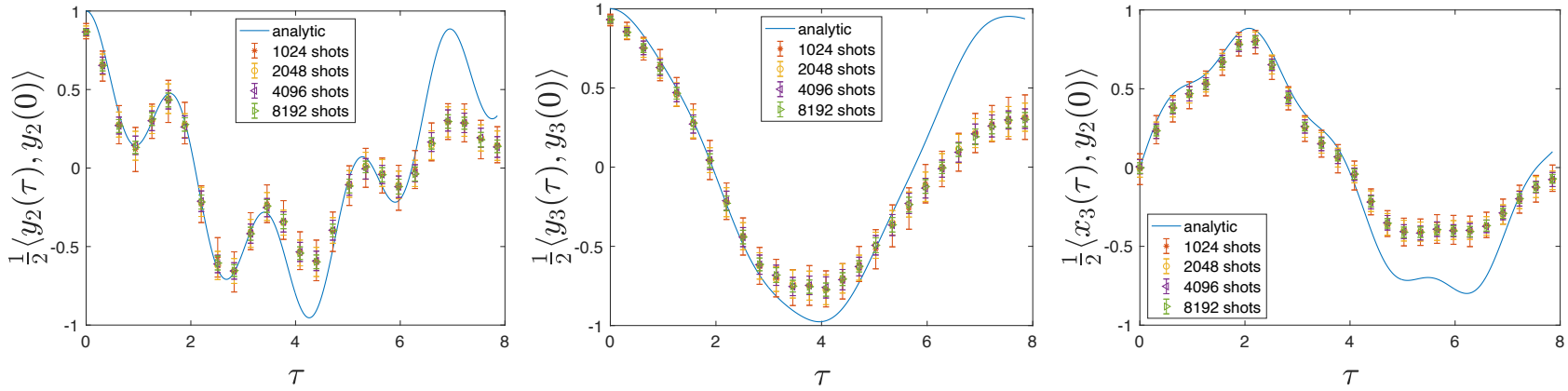

Figure 5.2: Correlators y_2-y_2, y_3-y_3 and x_3-y_2 evaluated in 25 Trotter steps of the duration $\Delta\tau = \frac{\pi}{10}$. The solid blue curves correspond to the analytical results, cf. Eqs. (4.19)–(4.21). System parameters are chosen to be $t = 1$ and $U = 4t$. Errors bars indicating the standard deviation of outcomes decrease with greater number of shots. The correlators were evaluated on Qiskit's noisy *Aer* simulator of the *FakeKolkataV2()* backend, an open-access simulator of the corresponding superconducting device *ibmq_kolkata* provided by IBM.

6 Variational Cluster Approach

In this introductory section we outline the basic idea behind the variational cluster approach (VCA) [59]. This recapitulation mainly serves for the purpose of demonstrating the usefulness of the quantum algorithms aimed at finding the correlation functions of moderately large clusters plus their potential speed-up over purely classical methods of computation. We also briefly recap the Hamiltonian of the Fermi-Hubbard model, which is a prototypical example where VCA can be successfully applied.

The VCA is a method that allows for solving many-body systems in a self-consistent manner. In general, we assume that a many-body system is described by a lattice Hamiltonian H of macroscopic size. While the number of qubits needed to encode the full Hilbert space of H scales linearly with the number of sites, the VCA enables one to reduce the number of required qubits by investigating only a small, representative subset, i. e., a cluster, of the full lattice. These clusters are disjoint, identical copies of each other, whose Hamiltonian is denoted as H'. Since the cluster acts as a proxy to the full system, meaningful investigations can be carried out with a relatively small quantum chip.

The Fermi-Hubbard model is described via a Hamiltonian of the form $H = H_0(\mathbf{t}) + H_1(\mathbf{U})$. It is a sum of a kinetic short-range hopping term characterized by amplitudes $\mathbf{t}$ and a repulsive on-site interaction of strength $\mathbf{U}$:

$$\hat{H} = -\mathbf{t} \sum_{\langle i,j\rangle,\sigma} \left(\hat{c}^\dagger_{i\sigma} \hat{c}_{j\sigma} + \hat{c}^\dagger_{j\sigma} \hat{c}_{i\sigma} \right) + \mathbf{U} \sum_i \hat{n}_{i\uparrow} \hat{n}_{i\downarrow}, \tag{6.1}$$

Again, the operators $\hat{c}_{i\sigma}$ and $\hat{c}^\dagger_{i\sigma}$ destroy or create an electron with spin σ on the ith site, respectively, $\hat{n}_{i\sigma} = \hat{c}^\dagger_{i\sigma} \hat{c}_{i\sigma}$ are number operators, and the summation in the kinetic term goes over nearest neighbors.

A microscopically small cluster described by H' can not lead to long-range effects such as magnetism and superconductivity, which arise in the macroscopic system described by the full H. In order to impose these effects in the cluster, we can add symmetry breaking terms to the Hamiltonian which may promote different superconducting, ferromagnetic or charge-density orders. A connection between micro- and macroscopic systems is established via their grand potentials. In particular, following Luttinger and Ward [79], one can consider the grand canonical potential (GCP) of interacting fermions to be a functional of the Green's function $\mathbf{G}$ and the self-energy $\mathbf{\Sigma}$,

$$\Omega_{\mathbf{t}}[\mathbf{G}, \mathbf{\Sigma}] = -\mathrm{Tr} \ln\left(\mathbf{G}_0^{-1} - \mathbf{\Sigma} \right) - \mathrm{Tr}(\mathbf{G}\mathbf{\Sigma}) + \Phi[\mathbf{G}], \tag{6.2}$$

where $\mathbf{G}_0^{-1}$ is the non-interacting Green's function and $\Phi[\mathbf{G}]$ is the Luttinger-Ward functional. Diagrammatically, the latter can be defined as a sum over all irreducible two-particle diagrams, referred to as skeleton diagrams, Fig. 6.1.

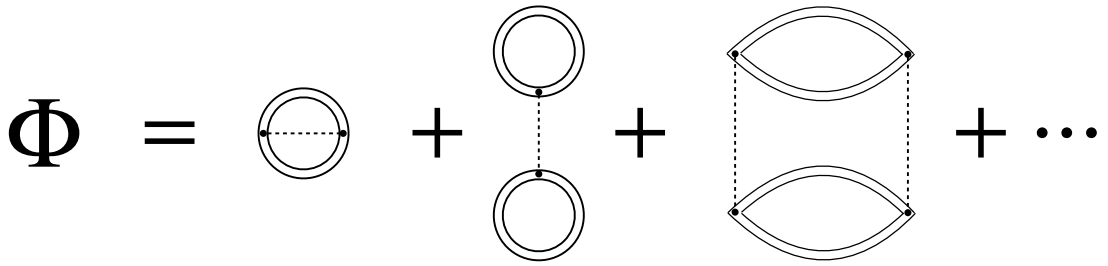

Figure 6.1: The Luttinger-Ward functional $\Phi[\mathbf{G}]$ is a sum over closed two-particle skeleton diagrams. The first summand is a particle-hole pair interacting with itself, the second summand are two particle-hole pairs interacting with each other once, the third summand are two particle-hole pairs interacting with each other twice.

In the expression above both the Green's function, $G^{\alpha\beta}_{\tau_1\tau_2}$, and the self-energy, $\Sigma^{\alpha\beta}_{\tau_1\tau_2}$, have to be understood as matrices in position, spin and (Matsubara) time domains, with Greek letters, $\alpha = (i, \sigma)$, being used as combined indices in lattice and spin spaces. The functional $\Omega_{\mathbf{t}}[\mathbf{G}, \mathbf{\Sigma}]$ achieves its stationary value at the physical $\mathbf{G}$ and $\mathbf{\Sigma}$. In particular, a functional derivative of the Luttinger-Ward functional gives the diagrammatic expansion for the self-energy,

$$\delta\Phi[\mathbf{G}]/\delta\mathbf{G} = \mathbf{\Sigma}[\mathbf{G}]. \tag{6.3}$$

This relation guarantees that $\delta\Omega_{\mathbf{t}}[\mathbf{G}, \mathbf{\Sigma}]/\delta\mathbf{G} = 0$. On the other hand, optimization over the self-energy yields the exact Dyson equation,

$$\frac{\delta\Omega_{\mathbf{t}}[\mathbf{G}, \mathbf{\Sigma}]}{\delta\mathbf{\Sigma}} = 0 \;\Rightarrow\; (\mathbf{G}_0^{-1} - \mathbf{\Sigma})\mathbf{G} = \mathbb{1}. \tag{6.4}$$

The variational principle outlined above can be simplified if one assumes that one can resolve (6.3) by defining the Green's function $\mathbf{G} = \mathbf{G}[\mathbf{\Sigma}]$ in terms of the self-energy. The functional in (Eq. (6.2)) then reduces to

$$\Omega_{\mathbf{t}}[\mathbf{\Sigma}] = -\mathrm{Tr}\ln\left(\mathbf{G}_0^{-1} - \mathbf{\Sigma}\right) + F[\mathbf{\Sigma}], \tag{6.5}$$

where we have introduced the Legendre transform of the Luttinger-Ward functional,

$$F[\mathbf{\Sigma}] = \Phi[\mathbf{G}[\mathbf{\Sigma}]] - \mathrm{Tr}(\mathbf{\Sigma}\mathbf{G}[\mathbf{\Sigma}]), \tag{6.6}$$

which satisfies $\delta F[\mathbf{\Sigma}]/\delta\mathbf{\Sigma} = \mathbf{G}[\mathbf{\Sigma}]$. It follows that $\Omega_{\mathbf{t}}[\mathbf{\Sigma}]$ is stationary at the physical self-energy, since the condition $\delta\Omega_{\mathbf{t}}[\mathbf{\Sigma}]/\delta\mathbf{\Sigma} = 0$ constitutes the Dyson equation, Eq. (6.4). An overview of this scheme is shown in Fig. 6.2.

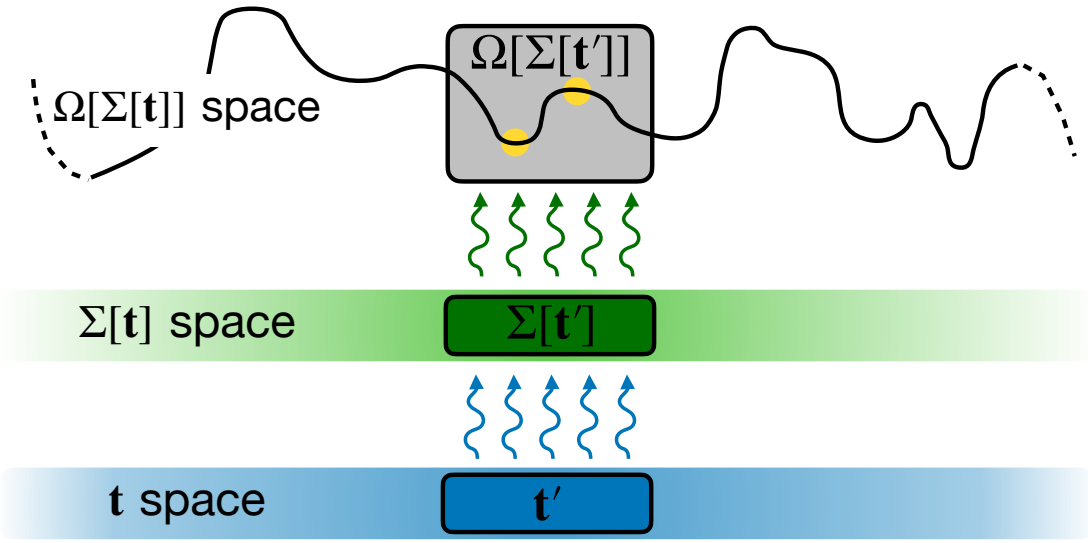

Figure 6.2: The variational cluster approach in practice. Within the vast space of $\mathbf{t}$ (blue stripe) one cuts out a subspace of trial single-particle parameters $\mathbf{t}'$ (dark blue box). Treating the latter as variational parameters, a set of trial self-energies $\Sigma[\mathbf{t}']$ (dark green box) can be proxied. Likewise, these self-energies are a subset of the full $\Sigma[\mathbf{t}]$ space (green stripe). The grand potential as a functional of the trial self-energies can then be scanned (gray box). The Dyson equation is solved as soon as one finds a saddle-point in the $\Omega[\Sigma[\mathbf{t}']]$ space. It is sufficient to find one of the two (yellow) saddle-points to satisfy the variational equation $\delta\Omega_{\mathbf{t}'}[\boldsymbol{\Sigma}]/\delta\boldsymbol{\Sigma} = 0$. Starting with a different set of variational parameters $\mathbf{t}'$ leads to different self-energies and finally to a different explorable subspace for the grand potential.

The Luttinger-Ward functional, and hence $F[\boldsymbol{\Sigma}]$, is not known in general [1], cf. [80]. However it is universal in the sense that it is defined only by the interaction part of the Hamiltonian, $H_1(\mathbf{U})$, and is independent of $H_0(\mathbf{t})$. This observation has motivated Potthoff to restrict the class of variational self-energies to those which optimize the functional $\Omega'_{\mathbf{t}}[\boldsymbol{\Sigma}]$ for the reference system of disjoint clusters described by the Hamiltonian $H = H_0(\mathbf{t}') + H_1(\mathbf{U})$. Denoting the (exact) solution of this optimization problem by $\boldsymbol{\Sigma}_{\mathbf{t}'}$, one can relate the original functional $\Omega_{\mathbf{t}}[\boldsymbol{\Sigma}]$ of the physical system to the reference one, $\Omega_{\mathbf{t}'} \equiv \Omega'_{\mathbf{t}}[\boldsymbol{\Sigma}_{\mathbf{t}'}]$, by a simple relation

$$\Omega_{\mathbf{t}}[\boldsymbol{\Sigma}_{\mathbf{t}'}] = \Omega_{\mathbf{t}'} - \mathrm{Tr}\ln\left(\mathbf{G}_0^{-1} - \boldsymbol{\Sigma}_{\mathbf{t}'}\right) + \mathrm{Tr}\ln\left(\mathbf{G}_0^{-1} - \boldsymbol{\Sigma}_{\mathbf{t}'}\right),$$

where $\mathbf{G}'_0$ represents the free fermion propagator of a cluster. The above approximate functional can be rewritten in the Fourier space with the help of Matsubara sums and treating a single cluster as a unit cell of the infinite size physical system,

$$\Omega_{\mathbf{t}}[\boldsymbol{\Sigma}_{\mathbf{t}'}] = \Omega_{\mathbf{t}'} - T\sum_{\omega_n,\boldsymbol{k}} \mathrm{Tr}\ln\left(1 - V_{\boldsymbol{k}}\mathbf{G}'(\omega_n)\right), \tag{6.7}$$

[1] One exception is the so-called SYK model with random all-to-all two-body interaction, where the Luttinger functional can be found on average, $\Phi[\boldsymbol{G}] = J\int d^2\tau\, G^4_{\tau_1\tau_2}$, with J being an interaction strength.

where $\mathbf{G}'(\omega_n) = \left(i\omega_n - \mathbf{t}' - \mathbf{\Sigma}_{\mathbf{t}'}(\omega_n)\right)^{-1}$ is the cluster Green's function expressed through the corresponding self-energy and $V_{\boldsymbol{k}} = \mathbf{t}' - \mathbf{t}_{\boldsymbol{k}}$ being a matrix of inter-cluster hopping terms.

The self-consistency scheme of the VCA then substitutes the variational principle in Eq. (6.4) by optimizing $\Omega_{\mathbf{t}}[\mathbf{\Sigma}_{\mathbf{t}'}]$ (Eq. (6.7)) over inter-cluster parameters $\mathbf{t}'$. The latter may include different mean-field order parameters related to expected patterns of symmetry breaking, which are not a part of the microscopic Hamiltonian (Eq. (6.1)).

Such optimization procedure over $\mathbf{t}'$ requires an efficient evaluation of the Green's function $\mathbf{G}$, which was provided to the reader in Ch. 4. As soon as the saddle-point with respect to the GCP in Eq. (6.7) is found, the approximate full system $\mathcal{G}_{\boldsymbol{k}}(\omega)$ can be restored by stitching together the twin clusters via

$$\mathcal{G}_{\boldsymbol{k}}(\omega) = \left(\mathbf{G}'^{-1}(\omega) - V_{\boldsymbol{k}}\right)^{-1}. \tag{6.8}$$

We have already discussed the superiority of quantum routines versus classical routines in Sec. 3.4. The following section taps into the application of the VCA onto the two-site dimer. The efficient evaluation of the GF was established in Sec. 3.2.2. We go one step further and parameterize the cluster GF under a variation in the Coulomb repulsion $\mathbf{U}$, thereby altering the effective relation between hopping and repulsion. This allows for a quick access to the GF, rendering subsequent circuit evaluations obsolete.

7 The variational cluster approach on the two-site dimer

Lastly, we touch on embedding our direct measurement scheme into the VCA. The two-site dimer as it was presented previously is investigated for Mott-transitions in Ref. [81]. For this model, the reference provides us with simple analytical formulae for the GF in frequency space.

The GF is part of the variational algorithm Eq. (6.7), with the variational parameter being the repulsion U, effectively affecting the relation of kinetic energy to repulsion energy. It can be similarly implemented as the quantum circuits for the repulsive term. With this in mind, there is no need for explicit formulation of a perturbation Hamiltonian, but rather adjust the inherent repulsion term U in the model Eq. (6.1) as a proxy accordingly.

According to [81], the analytical formulae for the GF read

$$G(z) = \frac{A}{z-\epsilon_1} + \frac{A}{z+\epsilon_1} + \frac{B}{z-\epsilon_2} + \frac{B}{z+\epsilon_2}, \tag{7.1}$$

$$\epsilon_1 = \frac{1}{4}\left(\sqrt{U^2+64t^2} - \sqrt{U^2+16t^2}\right), \tag{7.2}$$

$$\epsilon_2 = \frac{1}{4}\left(\sqrt{U^2+64t^2} + \sqrt{U^2+16t^2}\right), \tag{7.3}$$

$$A = \frac{1}{4}\left(1 - \frac{U^2-32t^2}{\sqrt{(U^2+64t^2)(U^2+16t^2)}}\right), \tag{7.4}$$

and finally

$$B = 0.5 - A. \tag{7.5}$$

7.1 Parameterization of the two-site dimer Green's function

The benefit of parameterization of the simulated GF is firstly a check, if known analytical results can be reproduced. Moreover, it allows for an easy engineering of the GF based on previous simulations. Given a parameterization in $\epsilon_1, \epsilon_2, A$ and B is sufficiently smooth, scanning the repulsion space in U for probing the GF in Eq. (6.7) can be made practical via interpolation between successive parameter data points.

Naturally, the simulation results Fig. 4.12 from a noisy simulator will not match the analytical results. The noise can be modeled by damping factors γ_1, γ_2, added in the corresponding denominators of Eq. (7.1). This factor is already known to us from Eqs. (0.13), (0.16). Given our hopping amplitude stays constantly at $t = 1$, Eqs. (7.1)–(7.4) transform to

$$G(\omega) = \frac{A}{\omega - \epsilon_1 + i\gamma_1} + \frac{A}{\omega + \epsilon_1 + i\gamma_1} + \frac{B}{\omega - \epsilon_2 + i\gamma_2} + \frac{B}{\omega + \epsilon_2 + i\gamma_2}, \tag{7.6}$$

$$\epsilon_1 = \frac{1}{4}\left(\sqrt{U^2 + 64} - \sqrt{U^2 + 16}\right), \tag{7.7}$$

$$\epsilon_2 = \frac{1}{4}\left(\sqrt{U^2 + 64} + \sqrt{U^2 + 16}\right), \tag{7.8}$$

$$A = \frac{1}{4}\left(1 - \frac{U^2 - 32}{\sqrt{(U^2 + 64)(U^2 + 16)}}\right). \tag{7.9}$$

To actuate a match between the simulation data in time-domain and the analytical frequency-dependent GF from Eq. (7.6), an inverse Fourier transformation onto the analytical formula yields

$$G(\tau) = 2\left(A\exp(-\gamma_1\tau)\cos(\epsilon_1\tau) + B\exp(-\gamma_2\tau)\cos(\epsilon_2\tau)\right). \tag{7.10}$$

Following chapters 4 and 5, we have simulated the FHM for the interval $U \in [0, 20]$. Simulation results were based on 26 Trotter steps with $\Delta\tau = \pi/10$, leading to a full simulation time of $T = 2.6\pi$. This is based on practical considerations, as it renders the numerical frequency domain symmetric.

To achieve a parameterization to the retarded GF based on noisy simulator data, we fit $G(\tau)$ in Eq. (7.10) to the simulated data. The results are presented in Fig. 7.1.

In some early instances of $U < 1$, discrepancies appear mostly in the energy value ϵ_2. At this point, the amplitude B of the Lorentzian peak is so small, that the position in the frequency domain becomes blurry. This problem may be worked around by having higher resolution in the frequency domain. Similarly, γ_2 spikes at weak U. Note, that larger values in U progressively worsen the match in amplitudes A, B, plus relatively strong discrepancies in values of ϵ_2. However, the parameters γ_1, γ_2 partially offset the discrepancies as they are not accounted for in the analytic curve.

With the help of the parameter set $p = [A, B, \epsilon_1, \epsilon_2, \gamma_1, \gamma_2]$, we can now engineer the empirical GF directly. In snapshots of $U \in \{0, 5, 10, 15\}$, we compare the empirical GF against the analytical GF in Figs. 7.2–7.5.

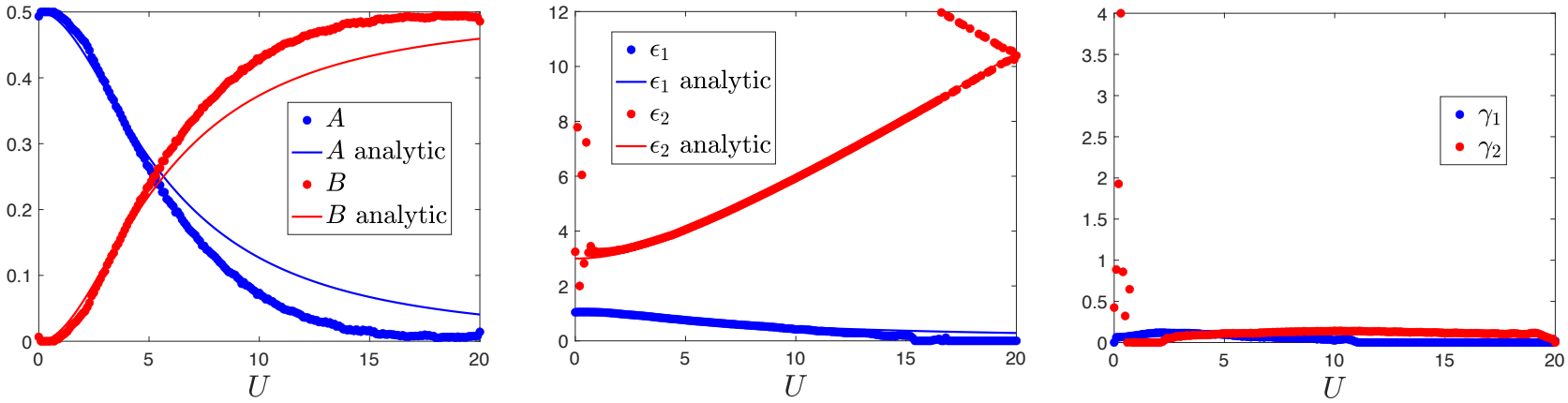

Figure 7.1: Amplitudes A, B *(left)*, energies ϵ_1, ϵ_2 *(center)* and damping factors γ_1, γ_2 *(right)* depending on the Coulomb repulsion U.

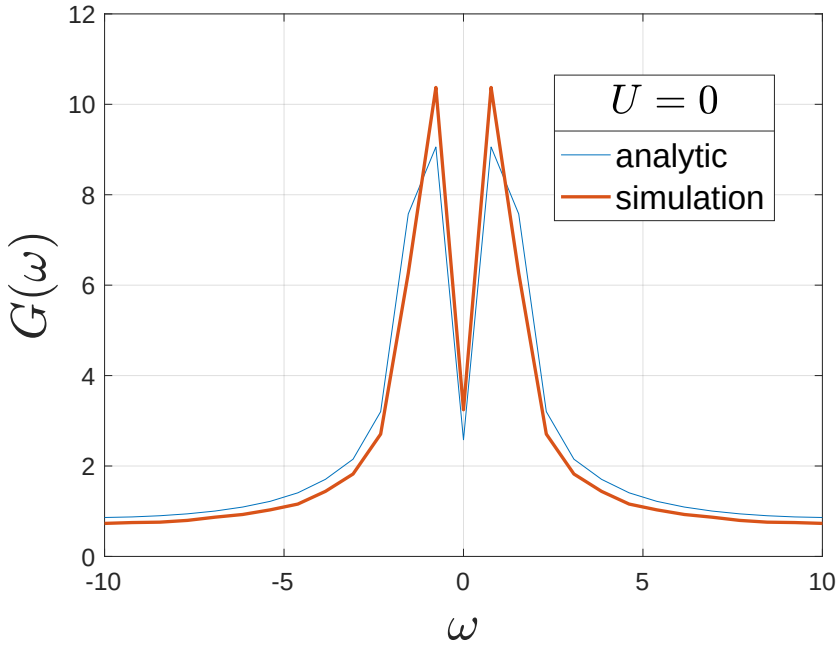

Figure 7.2: Parameterized Green's function for $U = 0$.

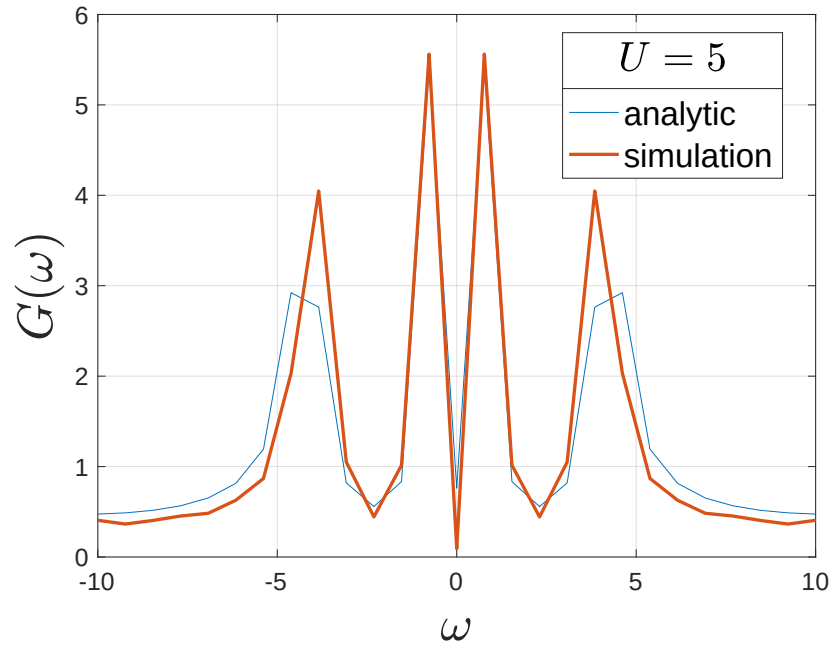

Figure 7.3: Parameterized Green's function for $U = 5$.

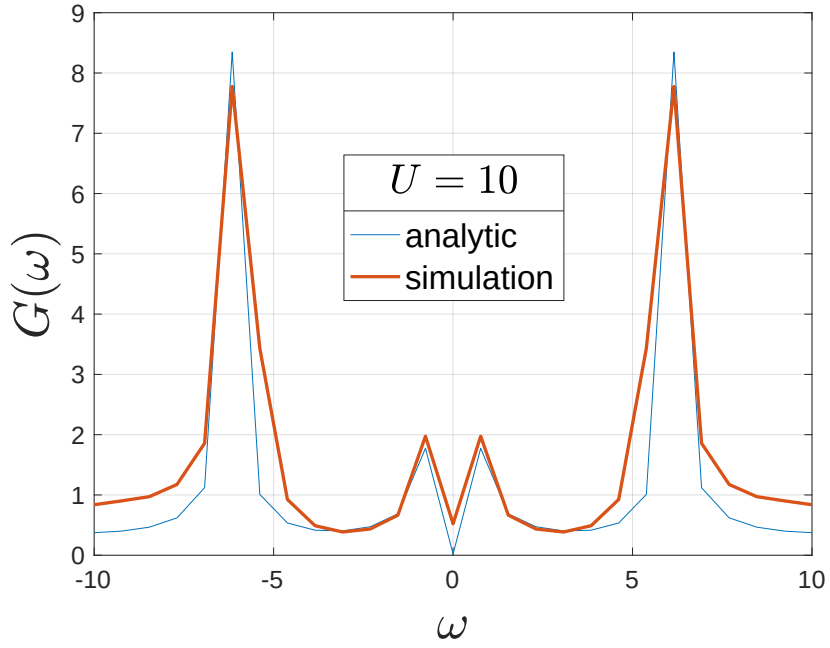

Figure 7.4: Parameterized Green's function for $U = 10$.

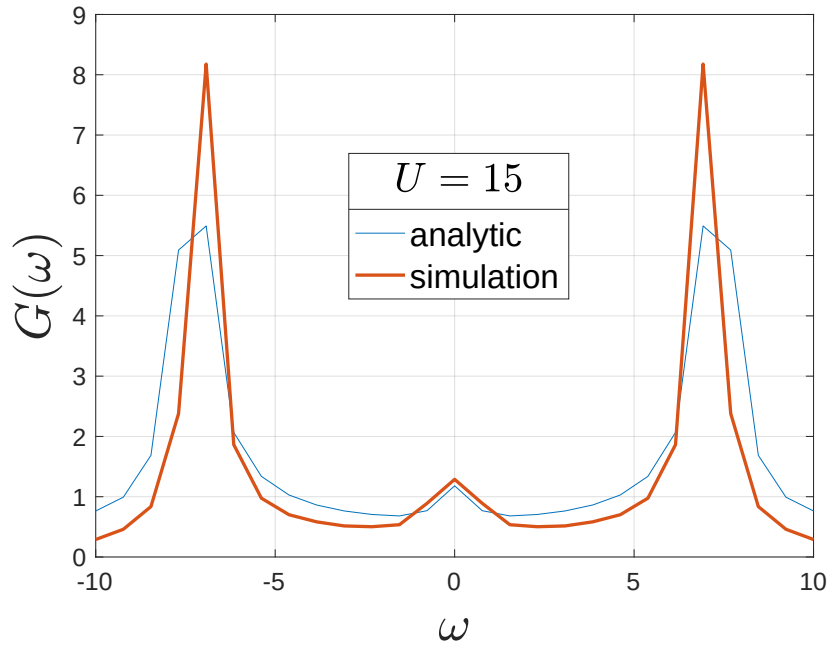

Figure 7.5: Parameterized Green's function for $U = 15$. The kink at $\omega = 0$ stems from the overlap of two peaks around ϵ_1, which is close to zero for $U \geq 15$.

The images show an overall good approximation of the GF in terms of the parameters $p = [A, B, \epsilon_1, \epsilon_2, \gamma_1, \gamma_2]$. In the context of the two-site dimer, the quick access to the Green's function is guaranteed by a successful parameterization.

Since the cluster GF is an input to the grand potential, Eq. (6.7), it would be of interest to check, if the latter can be parameterized from the parameters p in the toy study as well. If this was the case, we could rapidly scout the $\Omega[p]$ space to find a saddle-point in variations of p.

7.2 Determination of the phase diagram

Satisfying the GCP relation Eq. (6.7) yields the system parameters p, that generate a cluster, which in turn can be used to restore $\mathcal{G}_{\boldsymbol{k}}(\omega)$ (Eq. (6.8)), i. e., the effective approximate full system GF. For the optimal value of t/U, which is found from optimizing the VCA free energy Eq. (6.7), the cluster GF corresponds to the physical dynamics in the system. In this case the cluster GF can be used for the construction of the single-particle density of states $\rho(\omega)$:

$$\rho(\omega) = -\frac{1}{\pi}\mathrm{Im}\int_{\boldsymbol{k}} \frac{\mathrm{d}\boldsymbol{k}}{(2\pi)^d}\mathcal{G}_{\boldsymbol{k}}(\omega). \tag{7.11}$$

Negative frequencies $\omega < 0$ corresponds to possible states below the Fermi energy E_F; positive frequencies $\omega > 0$ correspond to those above the Fermi energy. By convention, at $\omega = 0$ we set $E_F = 0$. To distinguish if a large system is insulating or conducting, one checks the amplitude of the density of states at the Fermi energy. If $\rho(\omega = 0) = 0$, we have an insulator; a sharp peak around the Fermi energy ($\rho(\omega = 0) > 0$) signifies a metal.

If we wish to determine magnetization or superconductivity, firstly we need to make sure that the cluster is of appropriate size. Two sites are sufficient to study s-wave superconductivity, and also the transition from a metal to an insulator. If we wish to capture d-wave superconductivity or magnetization, at least four sites are required. Plus, in the case of d-wave superconductivity, a cluster should be at least of dimension two. For the study of antiferromagnetism and superconductivity, we refer to the works [61, 76]. The basic idea is to add symmetry breaking terms to the cluster Hamiltonian Eq. (1.1) to nudge the cluster system into phases (e. g., magnetic), which would naturally occur in the large system. The order parameter is then simply the amplitude of the added symmetry breaking term, which led to the satisfaction of the GCP relation Eq. (6.7).

Part II

Optimized quantum annealing

This part has been published as "Gino Bishop, Simone Montangero and Frank K. Wilhelm, *A Set of Annealing Protocols for Optimized System Dynamics and Classification of Fully Connected Spin Glass Problems*", arXiv:2310.10442 — Submitted on October 16th, 2023. It is an independent extension to the Master's thesis "Quantum annealing algorithms applied to infinite-range Ising problems", written under supervision of S. Montangero and with practical advice of F. Tschirsich. One figure from the Master's thesis was reproduced here.

Overview

In continuation of Sec. 0.5, a target eigenstate of a Hamiltonian is often the lowest energy state. For systems too large to be treated by exact diagonalization, quantum annealing can in principle be used to find the spectrum of a given Hamiltonian. Here, we are interested in the ground state as it represents the optimal solution to the Ising problem embodying an underlying combinatorial optimization problem. Particularly, we aim to find the ground state to problems associated with the Lechner-Hauke-Zoller (LHZ) [82] architecture, which is an annealing scheme designed to overcome challenges related to embedding problems into hardware graphs.

While specialized annealers exist for not-fully connected graphs, the intriguing advantage of the LHZ architecture is the achievement of all-to-all connectivity via fully programmable local interactions. A one-to-one mapping between local and full connectivity is established via mapping N *logical* qubits onto $K = N \cdot (N-1)/2$ *physical* qubits. Locally tunable constraints need to be introduced to balance out the increase in the amount of degrees of freedom. An implementation with Rydberg atoms in an optical lattice has been proposed [83], where the key challenge is reportedly the implementation of the constraints. Lastly, a generalization of the LHZ scheme within the stabilizer mechanism is possible [84]. The authors show that their proposed stabilizer formulation can reduce the qubit count in specific problems as well as map higher-order interactions in *logical* spins onto single *physical* qubits.

In this work, we explore the original LHZ proposal with $N = 5$ fully connected *logical* qubits. In particular, we aim to contribute to the process of finding optimal annealing schedules by providing a set of fixed optimized protocols, applicable to arbitrary transverse-field Ising instances within the LHZ scheme to ramp an initial Hamiltonian to the problem Hamiltonian. This is done by analyzing a sample of 2400 instances, which will serve as our training set. As these desired protocols are applied and evaluated on the basis of the large sample, by design protocols in S are not optimal for any individual instance, but rather outperform linear ones on a large class of programmable problems. Moreover, the protocols are deliberately different from each other, so that the variety of all protocols cover a wide range of instances. Lastly, all protocols can further be used as a collection of guess pulses for thorough optimization of system dynamics in any underlying problem of similar size. Optimizing annealing protocols beyond the linear slope enables us to find solutions for combinatorial optimization problems faster [85], especially if we allow for detachment from the adiabatic regime. Prior use of optimization techniques is required to find optimal protocols. For this task, we use the *dressed Chopped RAndom Basis algorithm* (dCRAB) [86, 87] which is a bandwidth-limited optimal control technique capable of exploring phase space in an ergodic fashion. It is part of the *Quantum Optimal Control Suite* (QuOCS), [88]. We will choose the ground state infidelity as the cost function.

The adiabatic condition, Eq. (0.12), requires the simulation time T to be sufficiently large to

enable conversion between two quantum states, with ΔE denoting the minimum instantaneous spectral gap between the ground state and the first excited state. What is an appropriate magnitude of T to use for an arbitrary instance? The answer becomes increasingly difficult to anticipate with more instances to be solved with the same strategy, not to forget that extracting ΔE is itself generally a challenging problem [14].

One way to handle this is to cluster instances according to some shared traits. We call the set that consists of groups of instances of similar kind $G \equiv \{g_1, g_2, \dots\}$. These kinds could include the magnitude of the global minimum gap ΔE, the number of local minimum gaps and their distribution throughout the annealing process. Intuitively, instances that share certain traits are then put into a single group g_i. We argue, that the assignment of instances to such groups simplifies the effort of finding optimal annealing protocols. Following this notion, we present routes to group instances, find optimal protocols for the individual groups g_i and probe their performance on a test set. The goal is to find a suitable protocol $s_i(\tau)$ for every group g_i, that in application yields average ground state fidelities of $\overline{\mathcal{F}}_{g_i} \geq 0.9$.

System dynamics to the use of those schedules display a trend: While some schedules keep the adiabaticity intact, others lead to a violation of the adiabatic condition, triggering non-adiabatic dynamics.

8 LHZ architecture

We chose to work on the LHZ architecture for two main reasons. Firstly, albeit four-body constraints need to be implemented which might pose a technical challenge, it is hardware-aligned as interactions are implemented locally. Secondly, from [82] we learn that there are discrepancies between the Ising spin glass and the programmable model in terms of three key metrics: deviation of the lowest energy levels at $\tau = 1$, the ratio of instantaneous gaps during the sweep and the time of occurrence of the minimum gap. Although these discrepancies can be damped depending on the choice of constraint strength C against interaction strength $|J|$, they will not vanish utterly. It is thus straightforward to argue that system dynamics will differ in both models.

Following [82], we give a brief overview on the LHZ architecture. For a thorough description we urge the interested reader to consult the original paper.

We start by describing the Hamiltonians and the mapping from *logical* to *physical* spins.

8.1 Fully connected annealer

We start from a classical Ising spin-glass type Hamiltonian

$$\hat{H}_p = \sum_{i=1}^{N-1} \sum_{j=i+1}^{N} J_{i,j}\, \hat{\sigma}_z^{(i)} \hat{\sigma}_z^{(j)}, \tag{8.1}$$

where the interactions $J_{i,j}$ encode some problem we wish to solve by finding the lowest energy configuration, and i, k run over spin-1/2 sites. While sampling $J_{i,j}$ from the binary configurations $\{0, 1\}$ is already sufficient to encode a range of hard problems such as the well known maximum cut problem [18], we follow LHZ by choosing $J_{i,j} \sim U(-J, J)$, i. e., the interaction matrix elements being continuously, uniformly sampled with $J = 1$.

We can obtain a quantum annealer by adding a local transverse field

$$\hat{H}_i = \sum_i \hat{\sigma}_x^{(i)}, \tag{8.2}$$

for which the initial ground state can be easily prepared, and then introduce two ramps $A(\tau)$ and $B(\tau)$ as

$$\hat{H}(\tau) = A(\tau)\hat{H}_i + B(\tau)\hat{H}_p. \tag{8.3}$$

In the adiabatic quantum annealing approach, the initial part is slowly ramped down from $A(\tau = 0) = 1$ to $A(\tau = 1) = 0$, while the final (problem) part is ramped up, $B(\tau = 0) = 0, B(\tau = 1) = 1$, over a timescale T which is large enough to allow an adiabatic passage such that at $t = T$ ($\tau \equiv t/T = 1$) we arrive in the ground state of $\hat{H}_p$.

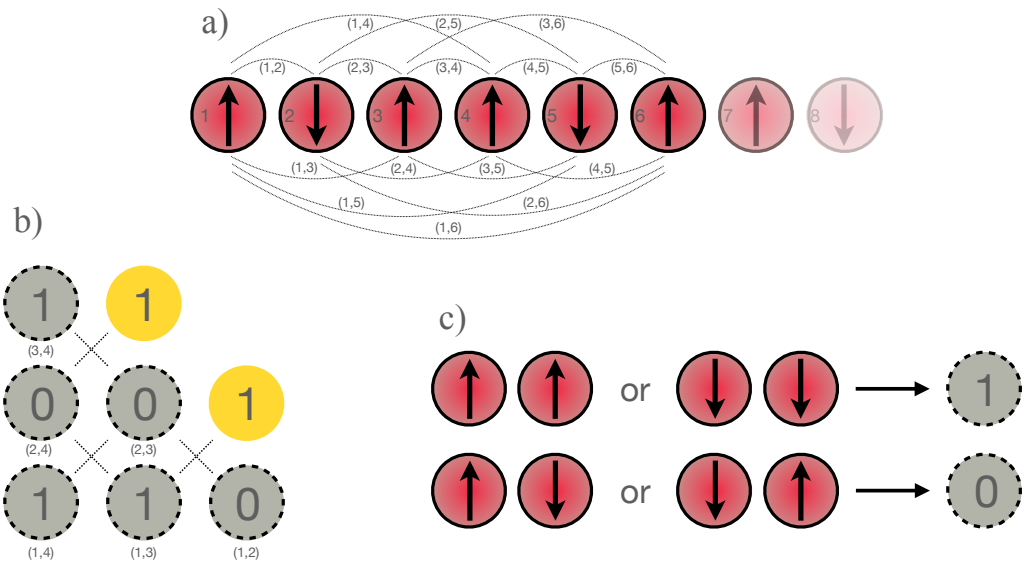

Figure 8.1: Mapping of the infinite-range interactions to local interactions as per [82]. a) Ising chain with six *logical* qubits (red, solid frame). Lines mark the interactions between qubit pairs (i, j). b) Corresponding *physical* qubit (gray, dashed frame) architecture with local interactions (reduced to four *logical* qubits due to space issues). Number of spin up in a given plaquette must be even. Two cornered qubits (yellow, open frame) are fixed to protect the constraints in edge cases. c) Set of rules for mapping *logical* (red, solid frame) to *physical* (gray, dashed frame) qubits.

8.2 LHZ architecture

We obtain the LHZ architecture by mapping the parity of every pair of two *logical* spins (i, j) from the fully connected, original problem, onto a single *physical* spin k.

As a result, from N *logical* spins, we obtain $K = N(N-1)/2$ *physical* spins with local fields $J_k = J_{i,j}$, and can directly map the final Hamiltonian onto

$$\tilde{H}_p = \sum_{k=1}^{K} J_k \, \tilde{\sigma}_z^{(k)}, \tag{8.4}$$

where $\tilde{\sigma}_x$, $\tilde{\sigma}_z$ are the spin-1/2 Pauli operators acting on the *physical* spins. The mapping is shown in Fig. 8.1. However, it is only invertible upon introduction of at least $K - N$ constraints mapping from K *physical* qubits back onto the N *logical* qubits. In the LHZ architecture, the *logical* state is resolved only up to global spin-flip parity. The latter can be alleviated by one more addition to a total of $N_c = K - N + 1$ constraints: The number of spin up must be even in every plaquette p. These constraints can be implemented by introducing an energy penalty of the form

$$\tilde{H}_c^{(p)} = -\tilde{\sigma}_z^{(p_1)} \tilde{\sigma}_z^{(p_2)} \tilde{\sigma}_z^{(p_3)} \tilde{\sigma}_z^{(p_4)}, \tag{8.5}$$

where $p_1 \ldots p_4$ label the spin in the four corners of plaquette p. Again, for an annealing

process, we introduce a simple local initial Hamiltonian

$$\tilde{H}_i = \sum_{k=1}^{K} \tilde{\sigma}_x^{(k)}. \tag{8.6}$$

The full passage Hamiltonian then reads

$$\tilde{H}(\tau) = \tilde{A}(\tau)\tilde{H}_i + \tilde{B}(\tau)\Big(\tilde{H}_p + \sum_{p=1}^{N_c} C^{(p)}(\tau)\tilde{H}_c^{(p)}\Big). \tag{8.7}$$

Aside from the ramps $\tilde{A}(\tau), \tilde{B}(\tau)$, we have introduced time-dependent constraint strengths $C^{(p)}(\tau)$ which can be tuned freely during the adiabatic passage but must ultimately become large enough to make sure the ground state fulfills all constraints at $\tau = 1$. This preserves the one-to-one mapping between *logical* and *physical* qubits, i. e., the constraints ensure that the solution to the problem in the LHZ scheme can be mapped to the solution to the original, all-to-all connected problem. As LHZ point out, the constraints $C^{(p)}$ influence the value of the minimal gap in the *physical* regime. It is therefore desired to find constraints that preserve the mapping while simultaneously prevent the size of the minimum energy gaps to drop significantly. There exist sweet spots in these functions $C^{(p)}$, which in principle can be subject to an optimization routine. In the supplementary material of the work by Lechner et al., the authors give quantitative suggestions for $C^{(p)}$ for $N \in \{3, 4\}$ *logical* qubits. Here, we set the constraints equal across all plaquettes, i. e., $C^{(p)} = C = 2.0$.

9 Optimization of annealing schedules

9.1 Design of fixed optimized schedules

The rate at which a system can be evolved in time is critically dependent on the size of the minimum gap (and its occurrence within the sweep). As we vary the interaction matrix in Eq. (8.4), we consequently change its energy landscape. Two Ising problems with arbitrary interaction matrices may exhibit, for instance, similar energy landscapes and thus energy gaps. Hence, the speed at which adiabatic time evolution can be performed should exhibit a comparable upper bound. Systems of ten or fewer *physical* qubits do hardly exhibit multiple minima in our training sample: For $K = 10$ we find the ratio of instances that have at least one local minimum alongside a global minimum is $< 1\%$. Moreover, as can be seen from Figs. 9.2, 9.3, the time of the emergence of the avoided crossing within the sweep is correlated to the magnitude of ΔE. The larger ΔE becomes, the earlier the emergence of the avoided crossing tends to occur. Since time of occurrence of the minimal gap is linked to its magnitude, and the number of instances exhibiting local minima is insignificant, we focus on the size of the minimal gap as our main metric used to generate problem groups.

The groups are designed such that if two instances are taken from the same group, they will exhibit a comparable minimum gap value. If one instance is taken from one group g_i, and another instance is taken from another group $g_{i'}$, $i \neq i'$, then the discrepancy between the two energy gaps grows. Consequently, for any two instances taken from g_i, we expect the annealing time required for a successful transition into the desired output state to be of similar order. This motivates the search for finite set of annealing protocols, where the idea is to customize protocols according to the different groups.

Table 9.1 summarizes the notation used throughout the following.

9.1.1 Problem groups

We start from a large sample M containing $|M| = 4 \cdot 10^4$ programmable instances, which are used to construct a training set of in total 2400 instances. Implementation and sampling details can be found in appendix B.1. The first step is to perform an exact diagonalization on all instances in order to obtain their individual minimum gap ΔE. We then sort all instances according to ΔE, such that for all instances $j \in M$

$$\Delta E_j \leq \Delta E_{j+1} \tag{9.1}$$

applies. Hence, the first instance ($j = 1$) has the smallest minimum gap, whereas the instance indexed by $j = |M|$ has the largest gap. The next step is to choose $|G|$, i. e., the number of groups included in G. We choose the number of groups to be six. This is

Symbol	Summary
j	Index of an instance.
M	Raw sample of $4 \cdot 10^4$ instances j.
ΔE_j	Minimal energy difference between ground state and first excited state of instance j.
g_i	Group, that includes many instances j of similar ΔE_j.
$G = \{g_1, g_2, \cdots, g_6\}$	Set of all groups.
ΔE_{g_i}	Average minimum gap over all instances j in g_i.
$s_i(\tau)$	Optimized schedule applied to all instances j in g_i.
$S = \{s_1, s_2, \cdots, s_6\}$	The set of optimized schedules.
$\lvert M\rvert, \lvert G\rvert, \lvert S\rvert$	Cardinality of M ($4 \cdot 10^4$), G (6) and S (6).

Table 9.1: Summary of notation used in Part II.

motivated by the notion, that less groups make the question of how large to choose T for all instances more difficult to solve, while too many groups render the applicability of all protocols in S too costly.

Afterwards, we put the first $|M|/|G|$ instances in g_1 and note the standard deviation $\sigma_1(\Delta E_1, \cdots, \Delta E_{|M|/|G|})$ in terms of their energy gaps. We do this for all groups in G. In this manner, we are able to assign a standard deviation σ_i to each group g_i. The goal is to shift instances from g_i to neighbored groups $g_{i\pm1}$ such that (i) $\sigma_1 \approx \sigma_2 \approx \cdots \approx \sigma_{|G|}$ and (ii) σ_i is as small as possible for all i. This approach has one major advantage: all ΔE from individual instances in a given group g_i are as similar as possible. This implies, that each group g_i is maximally different from the other groups $g_{i'\neq i}$. Hence, applying a group specific optimized protocol $s_i(\tau)$ onto any instance j in g_i yields meaningful results as opposed to applying it to an instance j' in $g_{i'}$, $i \neq i'$ and $j \neq j'$. At this point six groups spanning unique intervals of minimum energies exist. Our analysis suggests that 400 instances per group are sufficient to represent it fully (i. e., 2400 instances in total), which is on par with the analysis carried out in [82], where in total 400 instances were analyzed. Trimming down the number of instances per group to $|g_i|$= 400 leaves us with the final groups accompanied by the distribution of ΔE, Fig. 9.1.

The histogram of instances in the training set G is illustrated in Fig. 9.1. Groups of instances g_i are shaded in gray and white. Their width span the interval of ΔE for all instances within their corresponding group.

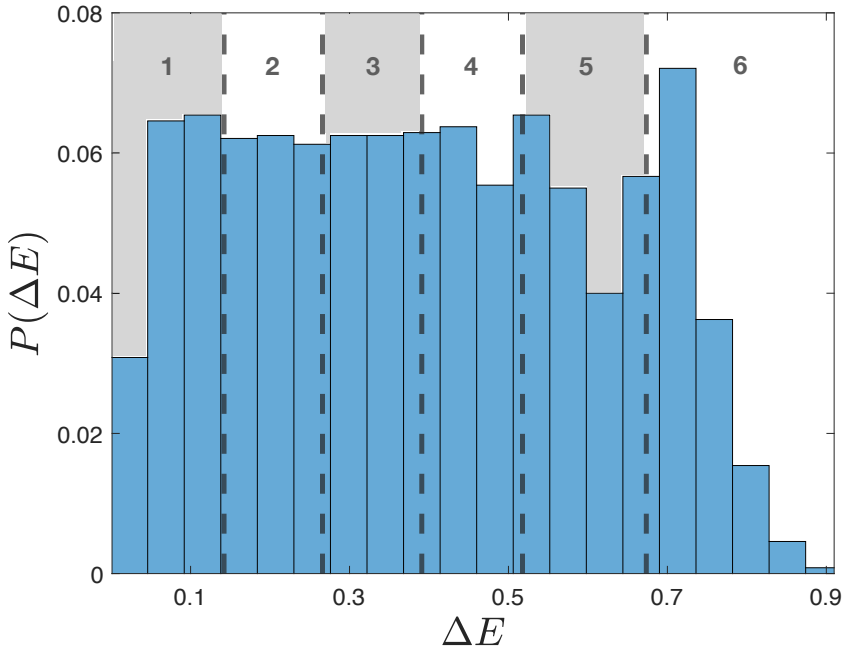

Figure 9.1: Histogram of minimum gaps. Areas of alternating shades represent all instances within a group g_i, numbered in ascending order at the top. Their width indicate the range of values in ΔE for each group.

9.1.2 Optimized schedules

Given a set G, we are now able to find out the set of corresponding optimized annealing protocols S by employing the dCRAB algorithm (cf. introduction to Part II). The first step is to define $A(\tau) \equiv 1 - s(\tau)$ and $B(\tau) \equiv s(\tau)$, Eq. (8.7). Moreover, we omit the explicit time-dependence of the protocols $s_i(\tau)$ to shorten equations and refining the figures, except when it serves the purpose of clarity. From here on, optimized protocols are called s_i, where i indicates the corresponding group, the protocol was designed for. Furthermore, due to the simple relation $A(\tau) = 1 - B(\tau)$, it is sufficient to denote the set of protocols as $S = \{s_1, s_2, \dots\}$. To measure the effect of a protocol s_i onto the time-evolution of all instances (indexed as j) in g_i, we take the average group fidelity $\mathcal{F}(s_i, g_i)$ into account, denoted by

$$\mathcal{F}(s_i, g_i) = \frac{1}{|g_i|} \sum_{j \in g_i} \mathcal{F}(s_i, j). \tag{9.2}$$

It is the average ground state fidelity at $\tau = 1$, which will be the figure of merit in the optimization loop. Here, the fidelity for a single instance j

$$\mathcal{F}(s_i, j) = |\langle \Psi_{\text{sim}}(s_i, j) | \Psi_{\text{exact}}(j) \rangle|^2 \tag{9.3}$$

is the overlap of simulated state $|\Psi_{\text{sim}}(s_i, j)\rangle$ and exact ground state $|\Psi_{\text{exact}}(j)\rangle$ of the final Hamiltonian $\tilde{H}_p$, Eq. (8.4), respectively.

The goal fidelity is chosen to be $\mathcal{F}(s_i, g_i) \geq 0.9$. As the group-specific average minimum gap ΔE_{g_i} heavily influences the required simulation time T to reach a given target ground state fidelity $\mathcal{F}(s_i, g_i) > 0.9$, we increase T until the target fidelity is reached. Fig. 9.2 and Fig. 9.3 show for all groups $g_i, i \in \{1, 2, 3, 4, 5, 6\}$ the average energy gap ΔE_{g_i} for all instances in g_i along with the associated optimized schedule s_i.

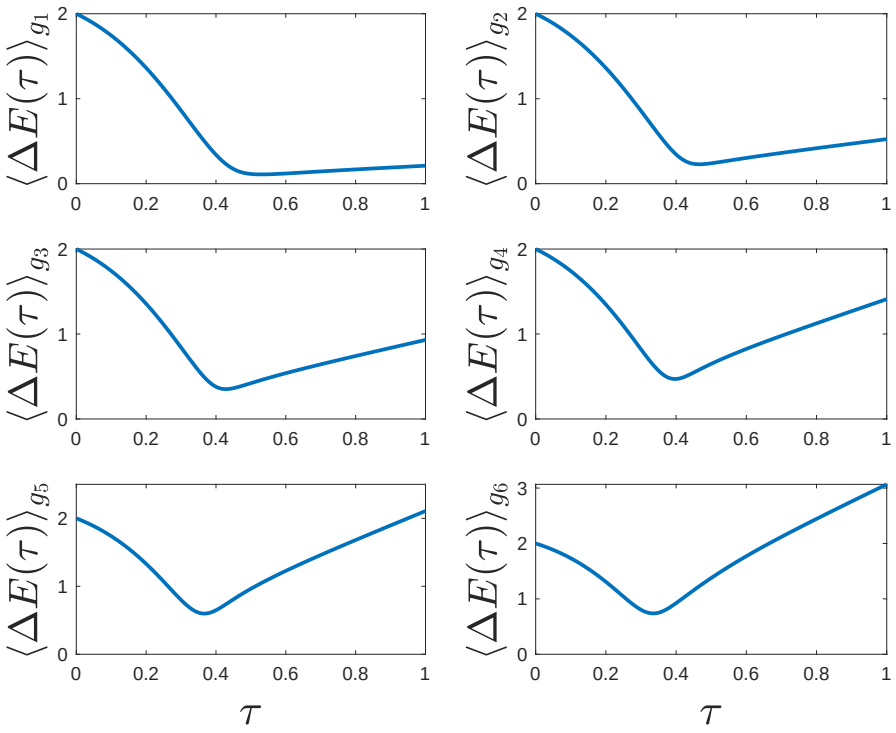

Figure 9.2: Instantaneous energies $\langle \Delta E(\tau) \rangle_{g_i}$ averaged over all instances in g_i (solid line) along with their corresponding optimized annealing protocols in s_i (dashed line) numbered in ascending order at the top.

Note, that by minimizing the annealing time T, we implicitly assume sufficiently long coherence times, allowing us to neglect them in the simulations. Realistically, quantum devices have coherence times, which shall not be exceeded by annealing times in order to allow for coherent dynamics. It is thereby reasonable to fix annealing times limited by coherence time, and minimize the ground state infidelity or energy instead of fixing the goal fidelity and minimizing annealing time. Results for the latter approach (fixed annealing times) can be found in B.3. The approach we have chosen (minimize annealing times) is motivated in Appendix B.2.

We report that when the average minimum gap ΔE_{g_i} over all instances in g_i becomes smaller, then the time of its occurrence shifts to the first half of the sweep, Fig. 9.2. The protocols s_i are reminiscent of characteristics from an optimal adiabatic ramp [23] as the first time derivative of $s_i(\tau)$ reaches a saddle-point, when the energy gap gets close to its minimum. Furthermore, the schedules do not necessarily start at zero, i. e., $s_i(\tau = 0) \neq 0, i = 5, 6$, and

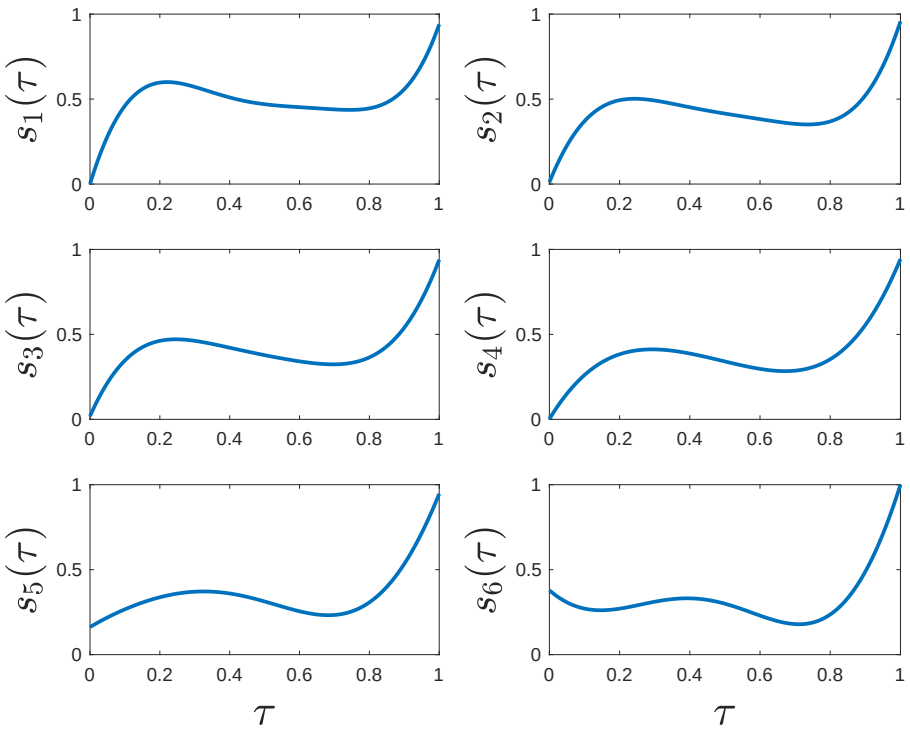

Figure 9.3: Optimized annealing schedules designed for groups g_i numbered in ascending order at the top.

do not necessarily end at unity by the end of the sweep, $s_i(\tau = 1) \neq 0, i = 1, \cdots, 5$. This indicates the presence of non-adiabatic effects; a dedicated analysis can be found in 10.4.

Another form of diabatic dynamics can be achieved via quantum walks [89]. We like to point the interested reader to literature, that dives deeper into the relation and potential interplay of both methods. Specifically, optimized schedules s_5 and s_6 expose a flat ramp in the region $\tau \in [0.0, 0.7]$, meaning that the Hamiltonian $\tilde{H}(\tau)$ (Eq. (8.7)) hardly changes in the time span. This can be linked to continuous-time quantum walks, and a combination of using both adiabatic annealing in tandem with quantum walks has been proposed [90]. Furthermore, quantum walks can be helpful in understanding the formation of optimal schedules in the non-adiabatic quantum regime [91, 92].

10 Performance analysis

This chapter starts with presenting the single-instance fidelities to the optimized schedules. The spread of fidelities is discussed, trending more narrow for instances that are considered easy.

Further on, we discuss the speed-up gained from the optimization of schedules over linear ramps. Interestingly, the speed-up is more apparent for instances that are easy to solve, e. g., have a relatively large minimum gap ΔE. The irritation is addressed in the section Sec. 10.4, investigating the nature of system dynamics to the schedules; it turns out, that instances which are easy to solve are more prone to adiabatic dynamics.

Lastly, we check the schedules on a test set of instances, which were not part of the design process of group-specific schedules s_i. The optimized schedules achieve similar fidelities, demonstrating their robustness on a wide range of problems.

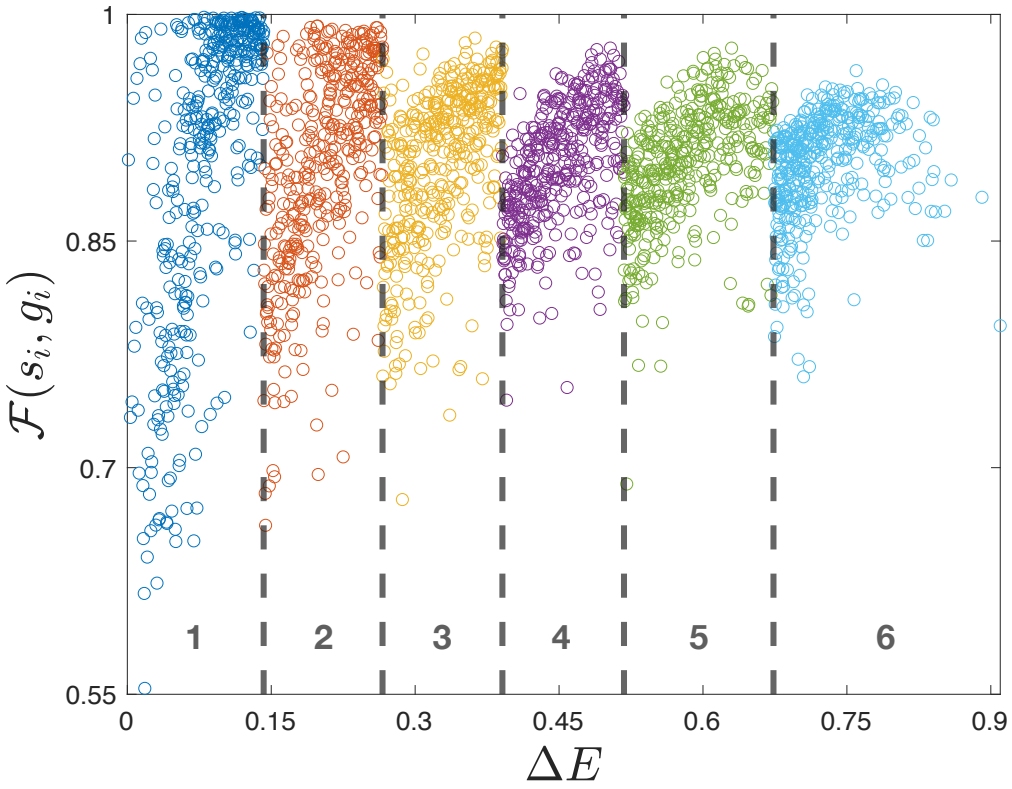

Figure 10.1: Single-instance fidelities $\mathcal{F}(s_i, j \in g_i)$ from optimal protocols $\{s_i\}$ onto all instances j of corresponding groups $\{g_i\}$ separated by solid vertical lines and numbered in ascending order at the bottom.

10.1 Single-instance fidelities

We show the distribution of single-instance fidelities $\mathcal{F}(s_i, j)$, Fig. 10.1, when the optimized protocol s_i is applied to its corresponding instances j in g_i. Vertical lines separate the groups in ascending order from left to right.

Clearly, the smaller the gaps become, the wider the spread of single-instance fidelities. This is due to the fact that the smaller the average energy gap per group, the wider is the range of required simulation time T as $T \sim \Delta E^{-1}$ (non-adiabatic) or $T \sim \Delta E^{-2}$ (adiabatic). Additionally, although the instance-dependent minimum gaps are correlated to their positions (smaller minimum gaps tend to occur later in the annealing process), variations in their locations further widen the spread in single-instance fidelities.

We find the ratio of instances with more than one energy minimum to be $< 1\%$ for $N = 5$ *logical* qubits. It shall be pointed out, that for system sizes of $N > 5$, multiple local minima are more likely to occur [93], contributing further to the hardness of the problem.

10.2 Speed-up from optimizations

Next, we compare required annealing times of linear and optimized annealing protocols, Fig. 10.2, needed to reach the mean goal fidelity $\mathcal{F}(s_i, g_i) \geq 0.9$. For $N = 5$ we have an averaged reduction of annealing time of 71.6%, i. e., one needs 3.52 fold longer annealing times with linear protocols compared to optimized ones. Raw numbers can be found in Table 10.1.

g_i	1	2	3	4	5	6
T_{lin}	326.72	123.05	74.71	53.05	39.59	30.63
T_{opt}	118.99	38.32	21.09	14.52	10.29	7.42

Table 10.1: Raw numbers for annealing times. For linear schedules, the average annealing time T_{lin} is 3.52 larger than annealing times T_{opt} for optimized schedules.

Note, that the speed-up becomes more noticeable for problem instances with a larger minimum gap. As T scales linearly (or quadratically) in the reciprocal of the minimum gap for non-adiabatic (or adiabatic) dynamics, one could expect the speed-up to be more prominent for problem instances with small minimum energy gaps. In the frame of the conducted simulations, those instances tend to prefer adiabatic dynamics. On the other hand, instances which have larger minimum energy gaps are more prone to non-adiabatic dynamics.

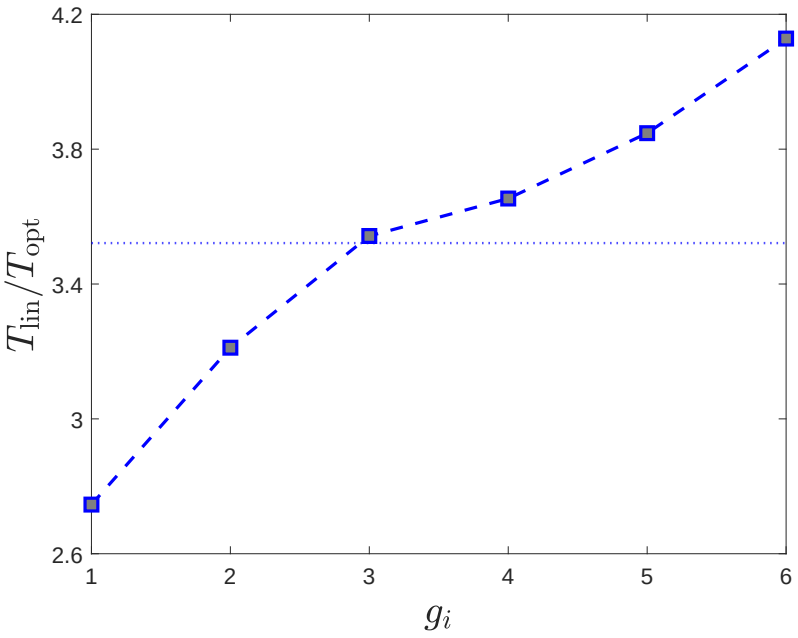

Figure 10.2: Simulation time speed-up for $N = 5$ from the set of optimized protocols s_i relative to a linear ramp to reach mean goal fidelity $\mathcal{F}(s_i, g_i) \geq 0.9$. Thick lines are group specific speed-ups, thin lines represent average speed-up of factor ~ 3.52.

10.3 Robustness test

Lastly, we probe optimized protocols in S gathered by analysis of the training set onto a different test set G^{test} of again $6 \cdot 400$ instances. Albeit no optimizations were performed with respect to the test set, a tiling into different groups g_i^{test} is required to verify, that the protocols are applicable and useful for any transverse-field Ising instance within the LHZ model and not a product of overfitting.

We find that $\forall i \in \{1, 2, 3, 4, 5, 6\}$ it holds $\mathcal{F}(s_i, g_i) \approx \mathcal{F}(s_i, g_i^{\mathrm{test}})$, cf. Fig. 10.3. This indicates that optimized protocols s_i indeed cover a wide range of programmable LHZ problems and can successfully be applied to arbitrary instances sampled via a similar distribution in J, cf. Appendix B.1.

Comparing with Fig. 10.4, we find that the lowest data point in fidelity $\mathcal{F}(s_i, g_i^{\mathrm{test}})$ is still above the 0.5 line.

Investigations for larger systems ($N > 5$) need to be carried out in order to probe the usability of the method and whether or not optimized protocols can be found, not to mention the number of groups necessary to cover a wide range of programmable LHZ problems. After all, larger systems are typically more relevant for real world applications, but often come with multiple local energy minima [94], which makes the design process of groups more complicated. Larger systems may pick up a Stückelberg phase when passing through multiple avoided crossings [95], which disturbs the single-instance wave function $|\Psi_{\mathrm{sim}}(s, j)\rangle$ and thereby fidelity, Eq. (9.3), in a non-trivial way.

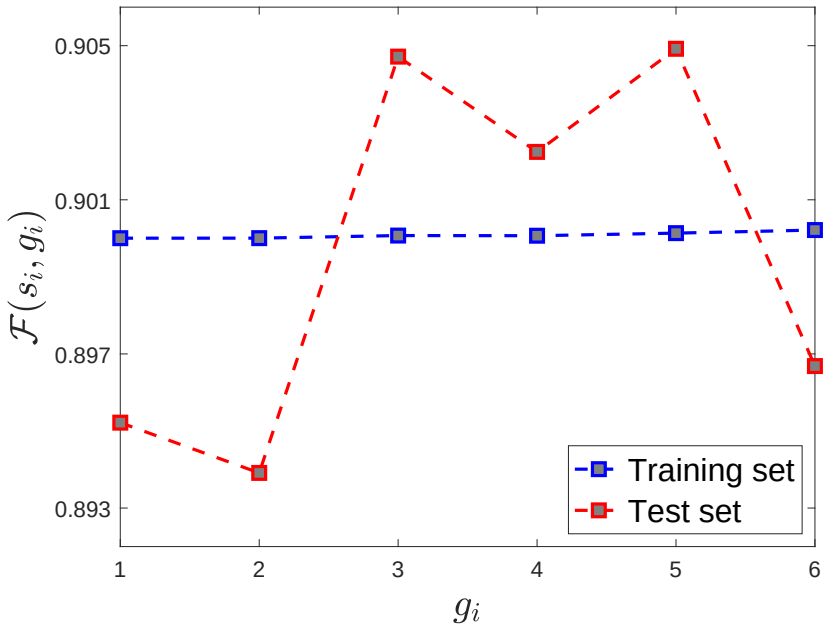

Figure 10.3: Comparison of averaged fidelities $\mathcal{F}(s_i, g_i)$ and $\mathcal{F}(s_i, g_i^{\text{test}})$ for $N = 5$ when applying optimized protocols in $\{s_i\}$ to all instances j in the training set $\{g_i\}$ and test set $\{g_i^{\text{test}}\}$. By design, $\mathcal{F}(s_i, g_i)$ is just above the 0.9 line.

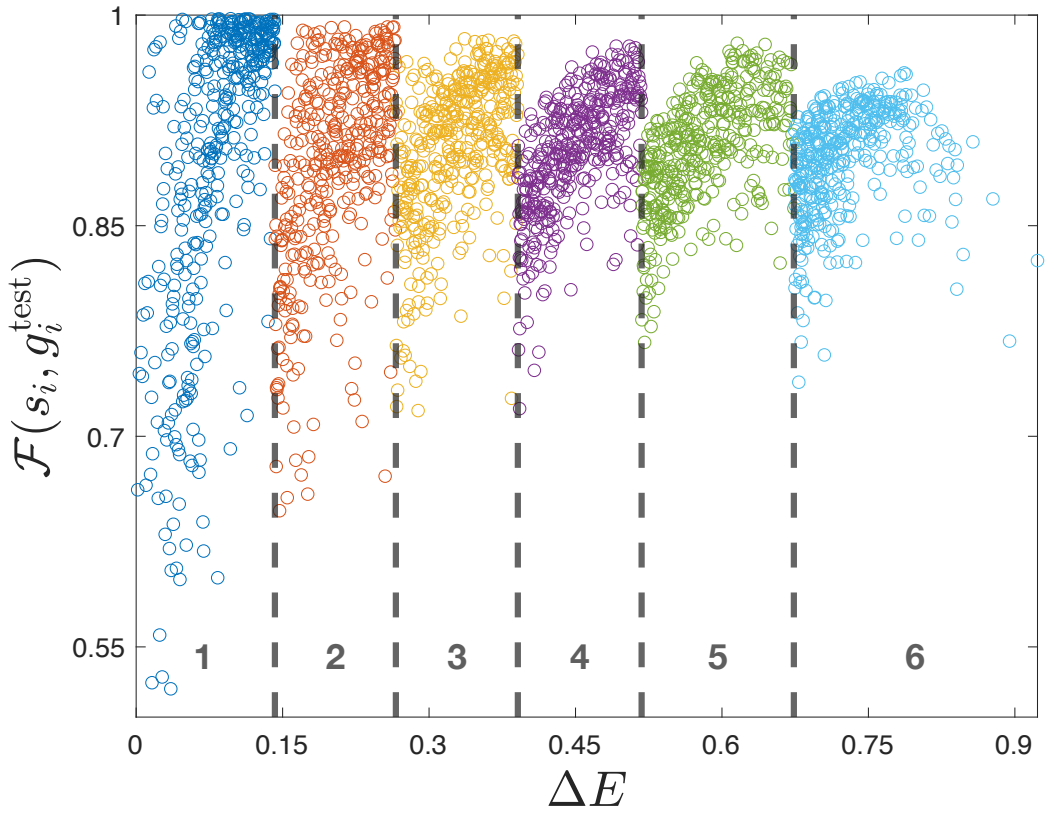

Figure 10.4: Single-instance fidelities $\mathcal{F}(s_i, j \in g_i^{\text{test}})$ in the test group from optimal protocols $\{s_i\}$ onto all instances j of corresponding groups $\{g_i^{\text{test}}\}$ separated by solid vertical lines and numbered in ascending order at the bottom.

10.4 Adiabaticity Check

If we compare with Fig. 9.3, we see that for group 5 and group 6 the schedule starts from a nonzero value, e. g., $s_i(\tau = 0) > 0, i = 5, 6$. This is the first hint to non-adiabaticity. We further see that the schedules are not monotonically increasing. In of itself this is not necessarily a violation of the Adiabatic Theorem [20], but in the context of minimizing the annealing time to a given goal solution, it is. To investigate this further, the instantaneous ground state probabilities $|\langle \Psi_{\text{sim}}(s(\tau))|\Psi_{\text{exact}}(s(\tau))\rangle|^2_{g_i}, i = 1, \cdots, 6$ (each line represents one instance out of the associated group) are shown in Fig. 10.5.

We remind the reader that the annealing times of the distinct groups are given in Tab. 10.1. The first group g_1 is comprised of instances with the smallest minimum gaps, hence the required annealing time is largest. Most of the instantaneous ground state probabilities are close to one, hinting that time evolution of instances in g_1 is dominated by adiabatic dynamics.

Already for group g_2, which includes the next hardest instances, we see a slight shift away from probabilities of one. This trend continues to unfold as group g_6 does not have a single instance, that is being evolved with an adiabatic schedule.

One way to look at this is by noticing that required annealing times for g_1 is large enough to allow for adiabatic evolution, whereas the much shorter annealing time for g_6 forces the system dynamics into diabaticity. Another way to look at it follows when we acknowledge that by employing optimal schedules $s_i(\tau)$, which are not necessarily one at the end of the sweep, Fig. 9.3, we effectively solve a slightly altered proxy problem in terms of a $\tilde{H}(\tau)$, Eq. (8.7), for which the solution directly maps to the original, diagonal problem Hamiltonian $\tilde{H}_p$, Eq. (8.4). In group g_1 and g_2 most of those proxy problems are solved adiabatically. However for members of groups g_4, g_5 and g_6 solutions to the proxy problems stem from diabatic dynamics.

For further investigation, one could explore the energy landscapes of individual problems in g_1 and g_6. By design, problems situated in group g_6 have a large minimum energy gap, e. g., $\langle \Delta E_{g_6} \rangle > \langle \Delta E_{g_1} \rangle$. Perhaps, a diabatic time-evolution is easier to navigate for problems with a larger minimum gap, because on average the system passes through less energy levels as compared to problems with very small minimum energy gaps.

Within the frame of our studies, arguably simpler instances benefit more from an optimization speed-up than more difficult problem instances. Non-adiabatic dynamics that emerge primarily for g_5 and g_6 benefit from shorter annealing times as $T \sim \Delta E^{-2}$. This is in stark contrast to adiabatic dynamics found in g_1 and g_2, for which $T \sim \Delta E^{-1}$. This results in the unexpected speed-up distribution in Fig. 10.2.

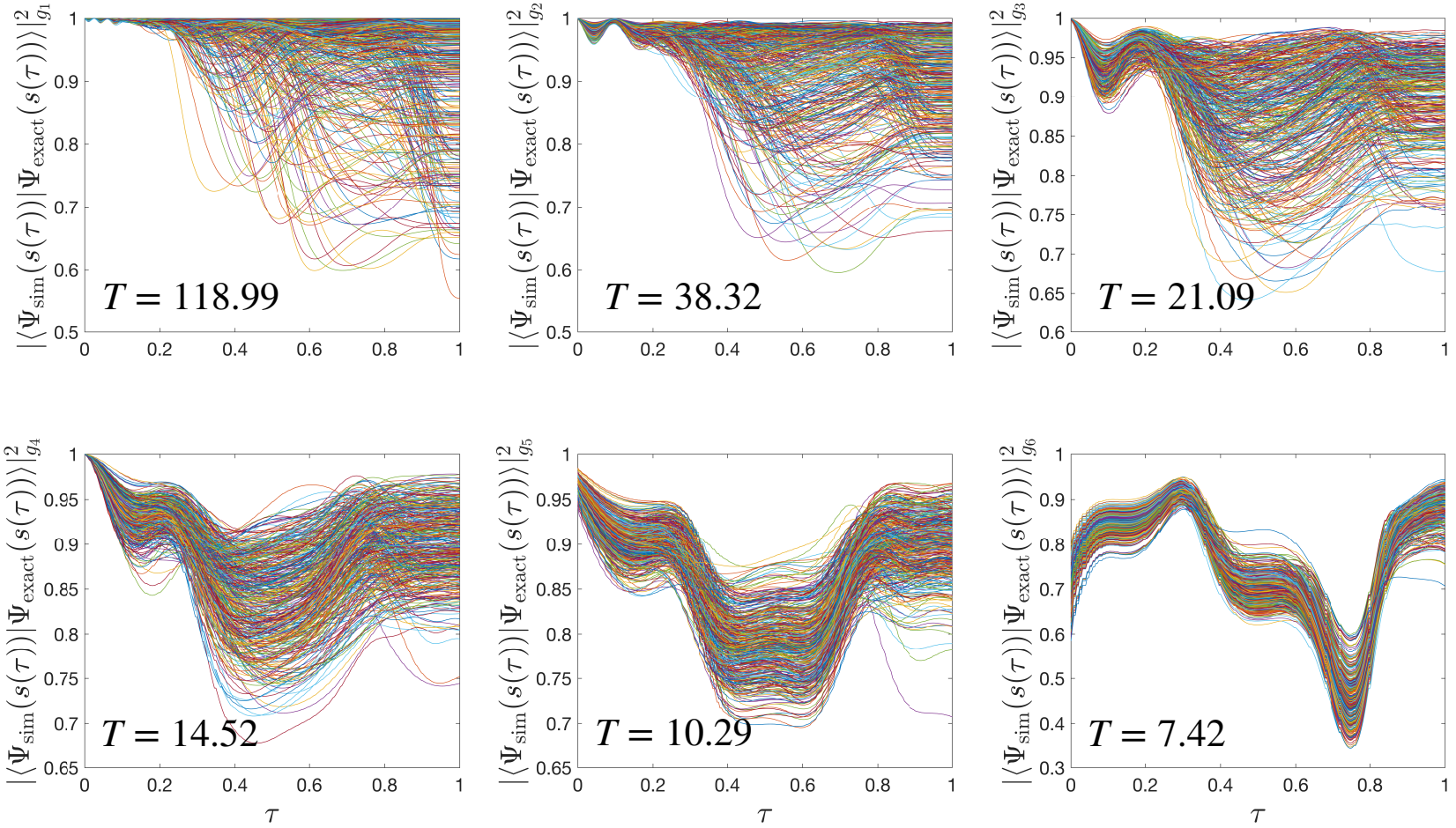

Figure 10.5: Instantaneous ground state fidelities $|\langle\Psi_{\rm sim}(s(\tau))|\Psi_{\rm exact}(s(\tau))\rangle|^2_{g_i}, i = 1, \cdots, 6$ and corresponding annealing times. Each line represents the probability trajectory of one instance in g_i. While system dynamics mainly follow adiabatic passages in g_1 and g_2 (large T), non-adiabatic patterns dominate in g_4, g_5 and g_6 (small T).

Synthesis

11 Summary & Takeaways

11.1 Part I: Simulation of correlated electrons

11.1.1 Summary

Chapter 1 introduces the Fermi-Hubbard model (FHM), which incorporates electronic correlations and can be used to study long-range effects such as d-wave superconductivity. This model is hard to solve classically, however there exist quantum routines that need much less computational resources compared to its classical counterpart.

In chapter 2, we lay out the quantum circuits that evaluate correlation functions, that constitude the system Green's function (GF). With a Jordan-Wigner (JW) mapping, the number of qubits scales linearly with the number of orbitals within the system. Chapter 3 presents the quantum routines to evaluate the GF and their complete quantum circuit representations.

Chapter 4 showcases the algorithm on a small toy model: the two-site dimer. We show data points for the GF ranging over 25 Trotter steps and plot these against the analytical GF. The fidelity of the results were significantly improved through the use of quantum error mitigation techniques. Full details on the conduction of the demonstration are to be found in chapter 5.

The following chapter 6 briefly introduces the variational cluster approach (VCA). It is a technique used to break down a full lattice system into smaller entities, which are easier to solve, but require careful tuning to serve as an effective approximation.

Finally, in chapter 7, we evaluate the cluster GF for 26 time steps. For a parameter space covering effective Coulomb repulsion, we show how a GF can quickly be parameterized in good approximation for repulsion values $U \in [0, 20]$. It can be achieved by introducing damping, reflecting the natural decoherence of qubits. As for the VCA, the cluster GF is an input parameter to an approximate large system's grand potential (GCP), subject to the variational principle with respect to the self-energy.

11.1.2 Takeaways

Part I lays out the complete path to solve the Fermi-Hubbard model (FHM) on a quantum computer. Starting from the FHM and its reformulation into quantum circuits, we explore two algorithms for evaluating the many-body GF. Both are equal in circuit depth. Yet, the direct measurement scheme turns out to be a powerful candidate when dealing with larger systems beyond one dimension due to its adaptability to a broader set of fermion-to-qubit mappings.

We provide the framework to prepare the ground state, its perturbation and finally the measurement of a hopping term, as part of the linear response routine. In its application to the toy model, we can recycle the simulated data to instantly engineer a GF via a few characteristic parameters reflecting the shape of the Fourier domain GF. This can be expanded to a quicker evaluation of the GCP, the key quantity for the Dyson equation to be asymptotically satisfied with ever growing clusters. Only then can the phase diagram be determined.

Lastly, the direct measurement algorithm in combination with the variational cluster approach can also be used to explore the phase diagram of more complex materials. For instance, twisted bilayer graphene exhibits high-temperature superconducting and Mott insulating phases. With current noisy intermediate-scale quantum (NISQ) devices, a six-site cluster could be implemented several times on the qubit architecture of a superconducting quantum chip. This makes the application of the VCA accessible even for a larger, unified cluster system.

11.2 Part II: Optimized quantum annealing

11.2.1 Summary

On the Lechner-Hauke-Zoller (LHZ) annealing architecture [82], outlined in chapter 8, our stated goal is to provide a set S that consists of fixed optimized annealing protocols $s(\tau)$, that outperform linear passage on a large class of transverse-field Ising problems. To that end, the target is to minimize the annealing time over which a system evolves from an initial Hamiltonian to a sampled problem Hamiltonian.

For $K = 10$ physical qubits, the annealing time is critically dependent on the minimum energy gap ΔE between ground state and first excited state within the instantaneous energy spectrum. We will use the amplitude of the gap as a proxy for the difficulty of a given problem.

Chapter 9 explores the idea to use pre-optimized ramps, that were designed for varying difficulties of problem instances, ranked via their minimum energy gap value. Therefore, six groups $g_i, i = 1, ..., 6$, were established, that collect instances with similar traits, specifically, with comparable ΔE per instance. This way, we can adjust required annealing times for each individual group within g_i, paving the way for an optimization over all instances $j \in g_i$ $\forall i \in \{1, 2, 3, 4, 5, 6\}$. We find six optimized protocols $s_i(\tau), i = 1, ..., 6$ that, when applied to their corresponding groups g_i, yield an average ground state fidelity of ≥ 0.9. We further showcase the robustness of the schedules in application to a wide range of programmable problems.

Chapter 10 discusses results and reliability of the optimized schedules. Utilizing them for their corresponding groups g_i reduces required simulation time by an average of 71.6% relative to linear protocols. In some cases, particularly for groups g_5 and g_6, the solution is reached via non-adiabatic time evolution, leading to a more drastic speed-up. However, if

the system is given more time, as is the case for solutions for groups g_1, g_2, g_3, the evolution is mainly governed by adiabatic dynamics.

A visual overview of the full process is given in Fig. B.2.

11.2.2 Takeaways

In Part II we find a set of optimal annealing schedules that lead to average ground state fidelities of $\overline{\mathcal{F}} \geq 0.9$ in the LHZ architecture, utilizing only local qubit couplings. We provide a framework to generate such intermediate optimized schedules. For high-fidelity optimizations of single-instances beyond $\overline{\mathcal{F}} \geq 0.99$, they could be used as an initial guess, potentially speeding up the search for suitable schedules.

Interestingly, instances with considerably large minimum energy gaps seem to benefit more from a quantum speed-up than more difficult instances. In our studies, instances with small minimam gaps are more prone to adiabatic dynamics, resulting in longer annealing times. Problem instances with a relatively large minimum gap tend more towards non-adiabatic dynamics, minimizing annealing times even further.

It is not yet clear if the strategy remains effective for systems consisting of more spins, e. g., larger systems tend to exhibit multiple local minima. In this case, we should not only group instances according to their ΔE, but also according to their number of local minima. Further investigations are needed as to how many groups are required for a beneficial tradeoff between correctness and cost. More groups mean more trial protocols. This decreases applicability, but naturally increases the performance of protocols. More generally, it needs to be verified, that one can expect similar results for larger systems.

On a different note, it would be interesting to study if the sole application of an optimized schedule to a given problem yields information on the problem itself. For instance, can the minimum gap of a given problem be inferred from its response to an applied schedule?

Lastly, the design of optimized protocols as presented in this paper requires knowledge of the minimum gaps, which were found via exact diagonalization. As this strategy is not applicable in a laboratory, we explore a method to generate optimized protocols experimentally on annealers in Appendix B.4.

12 Outro

Linear response experiments require the quantum system to be in equilibrium at time zero. Only then, the system is poked and a response is provoked. Quantum annealing can be utilized to prepare the equilibrium ground state of a strongly correlated many-body quantum system. The latter can be viewed as an all-to-all connected system, for which minor embedding can pose challenges. However, within the LHZ architecture, full connectivity is broken down to local connectivity, which is straightforward to implement on annealing platforms. Hence, at the intersection of both quantum annealing and linear response experiments, we find the ingredients to solve strongly correlated quantum systems from scratch.

Although the presented algorithms have been tailored to specific problems, a more general perspective highlights their potential: Both the direct measurement scheme and the optimized quantum annealing share the common goal of bringing quantum advantage closer to applications on NISQ devices.

The former is a novel quantum algorithm that matches the Hadamard test in the scaling of costly two-qubit gates. As a defining feature the new scheme can be extended to a broader class of fermion-to-qubit mappings. Combined with the variational cluster approach meaningful experiments can be conducted on relatively small quantum chips.

On the other hand, quantum annealing provides an approach for solving combinatorial optimization problems. Leveraging non-adiabatic quantum dynamics can lead to rapid convergence to the solution of a given problem. Since NISQ annealers are limited in their applicability in terms of coherence time, a significant reduction in the annealing time widens the range of problems, that can be effectively addressed.

The approaches benefit near-term applications on NISQ devices in that they are physically motivated and readily implementable on existing quantum hardware. While mathematical models continue to guide what is controlled in quantum systems, the need for high performance compute is reduced by delegating the most demanding tasks to nature itself. A many-body Green's function can be measured — not calculated. Annealers output the solution to a combinatorial optimization problem naturally — not numerically. In summary, the presented approaches offer ways to bring the break-even point for quantum advantage closer to the present.

Bibliography

[1] G. Rickayzen. Green's functions and condensed matter. In *Green's Functions and Condensed Matter*. Dover Publications, Inc., 2013.

[2] Amira Abbas et al. Challenges and opportunities in quantum optimization. *Nature Reviews Physics*, 6(12):718–735, October 2024. URL: http://dx.doi.org/10.1038/s42254-024-00770-9, doi:10.1038/s42254-024-00770-9.

[3] Frank Arute et al. Quantum supremacy using a programmable superconducting processor. *Nature*, 574(7779):505–510, October 2019. doi:10.1038/s41586-019-1666-5.

[4] John Preskill. Quantum Computing in the NISQ era and beyond. *Quantum*, 2:79, August 2018. doi:10.22331/q-2018-08-06-79.

[5] P. Krantz et al. A quantum engineer's guide to superconducting qubits. *Applied Physics Reviews*, 6(2):1–66, June 2019. arXiv:1904.06560v3, doi:10.1063/1.5089550.

[6] Masoud Mohseni et al. How to build a quantum supercomputer: Scaling challenges and opportunities, 2024. arXiv:2411.10406.

[7] Adam Winick, Joel J. Wallman, and Joseph Emerson. Simulating and mitigating crosstalk. *Phys. Rev. Lett.*, 126:230502, Jun 2021. URL: https://link.aps.org/doi/10.1103/PhysRevLett.126.230502, doi:10.1103/PhysRevLett.126.230502.

[8] Pascual Jordan and Eugene Paul Wigner. *Über Das Paulische Äquivalenzverbot*. Springer, 1993.

[9] Zhenyu Cai et al. Quantum error mitigation, 2023. arXiv:2210.00921.

[10] Avimita Chatterjee, Koustubh Phalak, and Phalak Ghosh. Author index - vol. 1. In *2023 IEEE International Conference on Quantum Computing and Engineering (QCE)*, volume 01, pages 1433–1440, 2023. doi:10.1109/QCE57702.2023.00162.

[11] Rajeev Acharya et al. Quantum error correction below the surface code threshold, August 2024. arXiv:2408.13687.

[12] Kristan Temme, Sergey Bravyi, and Jay M. Gambetta. Error Mitigation for Short-Depth Quantum Circuits. *Physical Review Letters*, 119(18):180509, November 2017. doi:10.1103/PhysRevLett.119.180509.

[13] Tadashi Kadowaki and Hidetoshi Nishimori. Quantum annealing in the transverse Ising model. *Physical Review E*, 58(5):5355–5363, November 1998. doi:10.1103/PhysRevE.58.5355.

[14] Tameem Albash and Daniel A. Lidar. Adiabatic quantum computation. *Reviews of Modern Physics*, 90(1), January 2018. arXiv:1611.04471v2, doi:10.1103/RevModPhys.90.015002.

[15] Edward Farhi et al. Quantum Computation by Adiabatic Evolution, January 2000. arXiv:quant-ph/0001106.

[16] Edward Farhi et al. A Quantum Adiabatic Evolution Algorithm Applied to Random Instances of an NP-Complete Problem. *Science*, 292(5516):472–475, April 2001. doi:10.1126/science.1057726.

[17] Rajesh Matai, Surya Singh, and M. L. Mittal. *Traveling Salesman Problem: An Overview of Applications, Formulations, and Solution Approaches*. Intechopen: London, UK, 2010; p. 1., November 2010. doi:10.5772/12909.

[18] F. Hadlock. Finding a Maximum Cut of a Planar Graph in Polynomial Time. *SIAM Journal on Computing*, 4(3):221–225, September 1975. arXiv:https://doi.org/10.1137/0204019, doi:10.1137/0204019.

[19] Bikas K. Chakrabarti, Ryo Tamura, and Shu Tanaka. *Quantum Spin Glasses, Annealing and Computation*. Cambridge University Press, 2017.

[20] M. Born and V. Fock. Beweis des Adiabatensatzes. *Zeitschrift für Physik*, 51(3-4):165–180, March 1928. doi:10.1007/bf01343193.

[21] Tosio Kato. On the Adiabatic Theorem of Quantum Mechanics. *Journal of the Physical Society of Japan*, 5(6):435–439, November 1950. arXiv:https://doi.org/10.1143/JPSJ.5.435, doi:10.1143/JPSJ.5.435.

[22] Sabine Jansen, Mary-Beth Ruskai, and Ruedi Seiler. Bounds for the adiabatic approximation with applications to quantum computation. *Journal of Mathematical Physics*, 48(10):102111, October 2007. doi:10.1063/1.2798382.

[23] Jérémie Roland and Nicolas J. Cerf. Quantum search by local adiabatic evolution. *Physical Review A*, 65(4), March 2002. doi:10.1103/physreva.65.042308.

[24] Erik Torrontegui et al. Shortcuts to Adiabaticity. *Advances In Atomic, Molecular, and Optical Physics*, 62(September):117–169, 2013. arXiv:1212.6343, doi:10.1016/B978-0-12-408090-4.00002-5.

[25] Xi Chen et al. Shortcut to Adiabatic Passage in Two- and Three-Level Atoms. *Physical Review Letters*, 105(12):123003, September 2010. doi:10.1103/PhysRevLett.105.123003.

[26] M. V. Berry. Transitionless quantum driving. *Journal of Physics A: Mathematical and Theoretical*, 42(36):365303, August 2009. doi:10.1088/1751-8113/42/36/365303.

[27] Takashi Imoto et al. Quantum annealing with twisted fields. *New Journal of Physics*, 24(11):113009, November 2022. doi:10.1088/1367-2630/ac9155.

[28] Herschel Rabitz et al. Whither the Future of Controlling Quantum Phenomena? *Science*, 288(5467):824–828, May 2000. doi:10.1126/science.288.5467.824.

[29] Tadashi Kadowaki and Hidetoshi Nishimori. Greedy parameter optimization for diabatic quantum annealing. *Philosophical Transactions of the Royal Society A: Mathematical, Physical and Engineering Sciences*, 381(2241):20210416, December 2022. doi:10.1098/rsta.2021.0416.

[30] Yu-Qin Chen et al. Optimizing quantum annealing schedules with Monte Carlo tree search enhanced with neural networks. *Nature Machine Intelligence*, 4(3):269–278, March 2022. arXiv:2004.02836, doi:10.1038/s42256-022-00446-y.

[31] Daniel Herr et al. Optimizing schedules for quantum annealing, 2017. arXiv:1705.00420.

[32] Shunji Matsuura et al. Variationally scheduled quantum simulation. *Physical Review A*, 103(5):4–9, May 2021. arXiv:2003.09913, doi:10.1103/PhysRevA.103.052435.

[33] M. W. Johnson et al. Quantum annealing with manufactured spins. *Nature*, 473(7346):194–198, May 2011. doi:10.1038/nature10012.

[34] T W B Kibble. Topology of cosmic domains and strings. *Journal of Physics A: Mathematical and General*, 9(8):1387–1398, August 1976. doi:10.1088/0305-4470/9/8/029.

[35] Quantum computer in the solid state. 2024. URL: https://q-solid.de.

[36] Roberto Orlando, Pina Romaniello, and Pierre-François Loos. The three channels of many-body perturbation theory: *GW*, particle–particle, and electron–hole *T*-matrix self-energies. *The Journal of Chemical Physics*, 159(18):184113, November 2023. doi:10.1063/5.0176898.

[37] Michael Potthoff. Self-Energy-Functional Theory. *Springer Series in Solid-State Sciences*, pages 303–339, August 2011. arXiv:1108.2183v1, doi:10.1007/978-3-642-21831-6_10.

[38] Richard D. Mattuck. *A guide to Feynman diagrams in the many-body problem*. Dover books on physics and chemistry. Dover Publications, New York, 2nd edition, 1992.

[39] Sergey B. Bravyi and Alexei Yu. Kitaev. Fermionic quantum computation. *Annals of Physics*, 298(1):210–226, 2002. URL: https://www.sciencedirect.com/science/article/pii/S0003491602962548, doi:10.1006/aphy.2002.6254.

[40] Charles Derby et al. Compact fermion to qubit mappings. *Physical Review B*, 104(3):035118, July 2021. doi:10.1103/PhysRevB.104.035118.

[41] Elbio Dagotto. Correlated electrons in high-temperature superconductors. *Reviews of Modern Physics*, 66(3):763–840, July 1994. doi:10.1103/RevModPhys.66.763.

[42] Goetz Moeller et al. Critical Behavior near the Mott Transition in the Hubbard Model. *Physical Review Letters*, 74(11):2082–2085, March 1995. doi:10.1103/PhysRevLett.74.2082.

[43] Eva Y. Andrei and Allan H. MacDonald. Graphene bilayers with a twist. *Nature Materials*, 19(12):1265–1275, November 2020. doi:10.1038/s41563-020-00840-0.

[44] Le Xu et al. Motion and thermal stability for high-temperature superconducting maglev vehicle under extreme crosswind conditions. *Physica C: Superconductivity and its Applications*, 628:1354620, 2025. URL: https://www.sciencedirect.com/science/article/pii/S0921453424001849, doi:10.1016/j.physc.2024.1354620.

[45] Ying Shirley Meng and M. Elena Arroyo-de Dompablo. First principles computational materials design for energy storage materials in lithium ion batteries. *Energy & Environmental Science*, 2(6):589, 2009. doi:10.1039/b901825e.

[46] John Hubbard. Electron correlations in narrow energy bands. *Proceedings of the Royal Society of London. Series A. Mathematical and Physical Sciences*, 276(1365):238–257, November 1963. doi:10.1098/rspa.1963.0204.

[47] Michael Schreiber et al. Observation of many-body localization of interacting fermions in a quasirandom optical lattice. *Science*, 349(6250):842–845, August 2015. doi:10.1126/science.aaa7432.

[48] Pranjal Bordia et al. Coupling Identical one-dimensional Many-Body Localized Systems. *Physical Review Letters*, 116(14):140401, April 2016. doi:10.1103/PhysRevLett.116.140401.

[49] Pranjal Bordia et al. Probing Slow Relaxation and Many-Body Localization in Two-Dimensional Quasiperiodic Systems. *Physical Review X*, 7(4):041047, November 2017. doi:10.1103/PhysRevX.7.041047.

[50] Elliott H. Lieb and F. Y. Wu. Absence of Mott Transition in an Exact Solution of the Short-Range, One-Band Model in One Dimension. *Physical Review Letters*, 20(25):1445–1448, June 1968. doi:10.1103/PhysRevLett.20.1445.

[51] J Voit. One-dimensional fermi liquids. *Reports on Progress in Physics*, 58(9):977, sep 1995. URL: https://dx.doi.org/10.1088/0034-4885/58/9/002, doi:10.1088/0034-4885/58/9/002.

[52] Elliott H. Lieb and F.Y. Wu. The one-dimensional hubbard model: a reminiscence. *Physica A: Statistical Mechanics and its Applications*, 321(1):1–27, 2003. Statphys-Taiwan-2002: Lattice Models and Complex Systems. URL: https://www.sciencedirect.com/science/article/pii/S0378437102017855, doi:10.1016/S0378-4371(02)01785-5.

[53] R. P. Feynman. Space-time approach to quantum electrodynamics. *Phys. Rev.*, 76:769–789, Sep 1949. URL: https://link.aps.org/doi/10.1103/PhysRev.76.769, doi:10.1103/PhysRev.76.769.

[54] Kiel T. Williams et al. Direct comparison of many-body methods for realistic electronic hamiltonians. *Phys. Rev. X*, 10:011041, Feb 2020. URL: https://link.aps.org/doi/10.1103/PhysRevX.10.011041, doi:10.1103/PhysRevX.10.011041.

[55] Matthias Troyer and Uwe-Jens Wiese. Computational complexity and fundamental limitations to fermionic quantum monte carlo simulations. *Phys. Rev. Lett.*, 94:170201, May 2005. URL: https://link.aps.org/doi/10.1103/PhysRevLett.94.170201, doi:10.1103/PhysRevLett.94.170201.

[56] Chris Cade et al. Strategies for solving the Fermi-Hubbard model on near-term quantum computers. *Physical Review B*, 102(23):235122, December 2020. doi:10.1103/PhysRevB.102.235122.

[57] Dave Wecker et al. Solving strongly correlated electron models on a quantum computer. *Physical Review A*, 92(6):062318, December 2015. doi:10.1103/PhysRevA.92.062318.

[58] David Sénéchal, Danny Perez, and Dany Plouffe. Cluster perturbation theory for Hubbard models. *Physical Review B*, 66(7):751291–7512911, August 2002. doi:10.1103/PhysRevB.66.075129.

[59] M. Potthoff. Self-energy-functional approach to systems of correlated electrons. *The European Physical Journal B - Condensed Matter*, 32(4):429–436, April 2003. doi:10.1140/epjb/e2003-00121-8.

[60] R. Somma et al. Simulating physical phenomena by quantum networks. *Physical Review A*, 65(4):042323, April 2002. doi:10.1103/PhysRevA.65.042323.

[61] Pierre-Luc Dallaire-Demers and Frank K. Wilhelm. Method to efficiently simulate the thermodynamic properties of the Fermi-Hubbard model on a quantum computer. *Physical Review A*, 93(3):032303, March 2016. doi:10.1103/PhysRevA.93.032303.

[62] Pierre-Luc Dallaire-Demers and Frank K. Wilhelm. Quantum gates and architecture for the quantum simulation of the Fermi-Hubbard model. *Physical Review A*, 94(6):062304, December 2016. doi:10.1103/PhysRevA.94.062304.

[63] Bela Bauer et al. Hybrid Quantum-Classical Approach to Correlated Materials. *Physical Review X*, 6(3):031045, September 2016. doi:10.1103/PhysRevX.6.031045.

[64] Francesco Libbi et al. Effective calculation of the Green's function in the time domain on near-term quantum processors. *Physical Review Research*, 4(4):043038, October 2022. doi:10.1103/PhysRevResearch.4.043038.

[65] Jannes Nys and Giuseppe Carleo. Quantum circuits for solving local fermion-to-qubit mappings. *Quantum*, February 2023. arXiv:2208.07192.

[66] Kangle Li and Hoi Chun Po. Higher-dimensional Jordan-Wigner transformation and auxiliary Majorana fermions. *Physical Review B*, 106(11):115109, September 2022. doi:10.1103/PhysRevB.106.115109.

[67] Alexander Altland and Ben D. Simons. *Condensed Matter Field Theory*. Cambridge University Press, Cambridge, 2 edition, 2010. doi:10.1017/CBO9780511789984.

[68] C. V. Raman and K. S. Krishnan. A New Type of Secondary Radiation. *Nature*, 121(3048):501–502, March 1928. doi:10.1038/121501c0.

[69] D.J. Thouless. Electrons in disordered systems and the theory of localization. *Physics Reports*, 13(3):93–142, October 1974. doi:10.1016/0370-1573(74)90029-5.

[70] Jan-Michael Reiner et al. Finding the ground state of the Hubbard model by variational methods on a quantum computer with gate errors. *Quantum Science and Technology*, 4(3):035005, May 2019. doi:10.1088/2058-9565/ab1e85.

[71] Tomislav Piskor et al. Using gradient-based algorithms to determine ground-state energies on a quantum computer. *Physical Review A*, 105(6):062415, June 2022. doi:10.1103/PhysRevA.105.062415.

[72] M.A. Nielsen and I.L. Chuang. *Quantum Computation and Quantum Information: 10th Anniversary Edition*. Cambridge University Press, 2010.

[73] Suguru Endo, Iori Kurata, and Yuya O. Nakagawa. Calculation of the Green's function on near-term quantum computers. *Physical Review Research*, 2(3):033281, August 2020. doi:10.1103/PhysRevResearch.2.033281.

[74] G. C. Wick. The evaluation of the collision matrix. *Phys. Rev.*, 80:268–272, Oct 1950. URL: https://link.aps.org/doi/10.1103/PhysRev.80.268, doi:10.1103/PhysRev.80.268.

[75] Gino Bishop, Dmitry Bagrets, and Frank K. Wilhelm. Quantum algorithm for green's functions measurements in the fermi-hubbard model, 2023. arXiv:2310.10412.

[76] David Sénéchal. An introduction to quantum cluster methods. pages 1–26, 2008. arXiv:0806.2690.

[77] Robert Eder. *The Variational Cluster Approximation*, volume 3. Verlag des Forschungszentrum Jülich, 2013.

[78] Qiskit contributors. Qiskit: An open-source framework for quantum computing, 2023. doi:10.5281/zenodo.2573505.

[79] J. M. Luttinger and J. C. Ward. Ground-State Energy of a Many-Fermion System. II. *Physical Review*, 118(5):1417–1427, June 1960. doi:10.1103/PhysRev.118.1417.

[80] Yingfei Gu et al. Notes on the complex Sachdev-Ye-Kitaev model. *Journal of High Energy Physics*, 2020(2), 2020. doi:10.1007/jhep02(2020)157.

[81] Ekkehard Lange. Renormalized Versus Unrenormalized Perturbation-Theoretical Approaches to the Mott Transition. *Modern Physics Letters B*, 12(22):915–919, September 1998. doi:10.1142/S0217984998001050.

[82] Wolfgang Lechner, Philipp Hauke, and Peter Zoller. A quantum annealing architecture with all-to-all connectivity from local interactions. *Science Advances*, 1(9), October 2015. doi:10.1126/sciadv.1500838.

[83] A. W Glaetzle et al. A coherent quantum annealer with Rydberg atoms. *Nature Communications*, 8(1):15813, June 2017. doi:10.1038/ncomms15813.

[84] Andrea Rocchetto, Simon C. Benjamin, and Ying Li. Stabilizers as a design tool for new forms of the Lechner-Hauke-Zoller annealer. *Science Advances*, 2(10):e1601246, October 2016. doi:10.1126/sciadv.1601246.

[85] Tommaso Caneva et al. Speeding up critical system dynamics through optimized evolution. *Physical Review A*, 84(1), July 2011. arXiv:1011.6634, doi:10.1103/PhysRevA.84.012312.

[86] Tommaso Caneva, Tommaso Calarco, and Simone Montangero. Chopped random-basis quantum optimization. *Physical Review A*, 84(2):022326, August 2011. doi:10.1103/PhysRevA.84.022326.

[87] N. Rach et al. Dressing the chopped-random-basis optimization: A bandwidth-limited access to the trap-free landscape. *Physical Review A*, 92(6):1–8, December 2015. arXiv:1506.04601, doi:10.1103/PhysRevA.92.062343.

[88] Marco Rossignolo et al. QuOCS: The quantum optimal control suite. *Computer Physics Communications*, 291:108782, October 2023. doi:10.1016/j.cpc.2023.108782.

[89] E. J. Crosson and D. A. Lidar. Prospects for quantum enhancement with diabatic quantum annealing. *Nature Reviews Physics*, 3(7):466–489, May 2021. doi:10.1038/s42254-021-00313-6.

[90] James G. Morley et al. Quantum search with hybrid adiabatic–quantum-walk algorithms and realistic noise. *Physical Review A*, 99(2):022339, February 2019. doi:10.1103/PhysRevA.99.022339.

[91] Adam Callison et al. Energetic Perspective on Rapid Quenches in Quantum Annealing. *PRX Quantum*, 2(1):010338, March 2021. doi:10.1103/PRXQuantum.2.010338.

[92] Sebastian Schulz, Dennis Willsch, and Kristel Michielsen. Guided quantum walk. *Physical Review Research*, 6(1):013312, March 2024. doi:10.1103/PhysRevResearch.6.013312.

[93] F Tanaka and S F Edwards. Analytic theory of the ground state properties of a spin glass. I. Ising spin glass. *Journal of Physics F: Metal Physics*, 10(12):2769–2778, December 1980. doi:2011041301462400.

[94] Stefan Schnabel and Wolfhard Janke. Distribution of metastable states of Ising spin glasses. *Physical Review B*, 97(17):174204, May 2018. doi:10.1103/PhysRevB.97.174204.

[95] S.N. Shevchenko, S. Ashhab, and Franco Nori. Landau–Zener–Stückelberg interferometry. *Physics Reports*, 492(1):1–30, July 2010. doi:10.1016/j.physrep.2010.03.002.

[96] Steven J. Weber et al. Coherent Coupled Qubits for Quantum Annealing. *Physical Review Applied*, 8(1):014004, July 2017. doi:10.1103/PhysRevApplied.8.014004.

[97] Philipp Hauke et al. Perspectives of quantum annealing: Methods and implementations. *Reports on Progress in Physics*, 83(5):054401, May 2020. doi:10.1088/1361-6633/ab85b8.

A Appendix for Part I

A.1 Derivation of the Kubo formula

In this Appendix we summarize the basics of linear response theory and derive the generalized susceptibility (3.10). Consider the Hamiltonian of a system, $H'(t) = H + V(t)$, with a perturbation $V(t) = \sum_j \Phi_j(t) A_j$ acting at times $t > 0$ and given by the sum of hopping operators A_j defined in Eq. (3.8). Let also $\rho_0 = \rho(t = 0)$ be an initial density matrix. Presently, we have $\rho_0 = |\Psi(\alpha_*, \beta_*)\rangle\langle\Psi(\alpha_*, \beta_*)|$, with (α_*, β_*) being the optimal parameters of the VHA. However the exact form of ρ_0 is not important for what follows.

By introducing the Heisenberg operators, $\widetilde{A}_i(t) = e^{iH't} A_i e^{-iH't}$, we are aiming to find how their averages,

$$\langle \widetilde{A}_i(t) \rangle_\Phi = \mathrm{Tr}(\rho_0 A_i(t)), \tag{A.1}$$

change in time in response to the perturbation $V(t)$. Here, a subscript in the average, $\langle \dots \rangle_\Phi$, indicates that the latter is a functional of generalized forces $\Phi_j(t)$. To this end, we switch to the interaction picture by defining $A_i(t) = e^{iHt} A_i e^{-iHt}$ such that the average in Eq. A.1 becomes

$$\langle \widetilde{A}_i(t) \rangle_\Phi = \mathrm{Tr}\left[\rho_0 U^+(t) A_i(t) U(t)\right], \tag{A.2}$$

where

$$U(t) = e^{iHt} e^{-iH't} \equiv T_t \exp\left\{-i \int_0^t V_I(t')dt'\right\} \tag{A.3}$$

is an evolution operator in the interaction picture expressed via $V_I(t) = \sum_j \Phi_j(t) A_j(t)$. At this point we may expand $U(t)$ up to first order in perturbation $V_I(t)$ and obtain

$$\langle \widetilde{A}_i(t) \rangle_\Phi = \langle A_i(t) \rangle + i \int_0^t \mathrm{d}t' \langle [V_I(t'), A_i(t)] \rangle + \dots, \tag{A.4}$$

where $\langle \dots \rangle$ denotes an average with the initial density matrix ρ_0. For our choice of operators A_i the 0th order term in Eq. A.4 vanishes. On introducing the response function

$$\chi_{ij}(t, t') = -i\Theta(t - t') \langle [A_i(t), A_j(t')] \rangle, \tag{A.5}$$

we finally find the Kubo formula. It states that in linear order the response of a system to the perturbation $\Phi_j(t)$ is given by

$$\delta \langle \widetilde{A}_i(t) \rangle = \int_0^t \chi_{ij}(t - t') \Phi_j(t') dt'. \tag{A.6}$$

In particular, if the perturbation is localized in time at $t = 0$, i.e. $\Phi_j(t) = \Phi_j\,\delta(t)$, then Eq. A.6 yields

$$\delta\langle\widetilde{A}_i(t)\rangle = \sum_j \chi_{ij}(t)\Phi_j. \tag{A.7}$$

In this form it can be used to construct the corresponding quantum circuits as described in the main text.

B Appendix for Part II

B.1 Implementation details

We generated transverse-field Ising models according to $\tilde{H}_p$, cf. Eq. 8.4. Specifically, we varied the interaction matrix J in the uniform interval [-1,1]. Randomization was performed by a Mersenne-Twister python implementation. The constraints C are equal for all plaquettes p and ramped up linearly as $C(\tau) = \tau \cdot C$, i. e. decoupled from the problem Hamiltonian (Eq. 8.7). The strength was chosen according to analysis by LHZ for $N \in \{3, 4\}$. For five *logical* qubits we set $C \equiv C^{(p)} = 2.0$.

Transverse-field Ising problems, which exhibit a ground state degeneracy at or critically close to $t \approx T$ were discarded for simplification of ground state fidelity evaluations. If the degeneracy appears at $t = T - \delta$, and δ is in the scale of the smallest numerical time step, then the system has hardly time to emancipate from its degeneracy. Additionally, some instances did violate the constraints and thus prevent a one-to-one mapping between *logical* and *physical* qubits. Lastly, instances for which a fidelity $\mathcal{F} \geq 0.9$ can not be reached within a reasonably large simulation time $T = 1000$ were discarded.

The training set consists of $6 \cdot 400$ instances, whereas we start from in total $4 \cdot 10^4$ programmable problems. Constructing six groups leaves us with uneven numbers of instances per group. How many instances do we need to represent a specific group? LHZ used in total 400, and we find that a histogram over the distribution of ΔE is not harmed by carefully cutting off instances, such that we deem 400 instances per group sufficient to solve the stated goals.

B.2 Justification of goal fidelity

Fixing the annealing time according to a given coherence time of a quantum device is reasonable and intuitive. These simulations were carried out in B.3. Here, we want to make the case for minimizing the annealing time for reaching a target fidelity.

We start by pointing out two structural benefits. Firstly, a ground state fidelity of 0.9 arguably implies that one has found a good solution to a given problem within the first few repetitions. With this, we make sure that all problems we consider are being solved. The question becomes how we can solve such problems even faster. Secondly, after the fact it turns out that by setting the target fidelity, we are able to study the bulk transition from adiabatic to non-adiabatic dynamics. A goal fidelity of 0.9 has shown to open up possibilities for entering non-adiabatic regimes, particularly if the system is given little annealing time, Fig. 10.5.

The following is meant to additionally justify a goal fidelity of $\mathcal{F}(s_i, g) > 0.9$ on a numerical basis.

1. The required fidelity drastically depends on the annealing time T. Hence, as we fixate the goal fidelity to 0.9, we can perform the task of finding optimized schedules much quicker than if we were searching for fidelities close to unity.
2. Some instances in g_1 demand excessive computational resources to be treated in an adiabatic way. For those instances, we find the minimum gap ΔE to be close to zero and the emergence of the avoided crossing to be around $\tau \lesssim 1$. This might indicate an artifact of too small choice of $C^{(p)}$. Still, as such instances contribute to the average fidelity, this limits the upper bound of fidelity values that can be reached.
3. The protocols in $\{S\}$ are by design not optimal for any arbitrary single instance, but can be used as guess pulses for single-instance protocol optimizations. If we were to target group-specific average fidelities of $\mathcal{F}(s, g_i) > 0.99$, we might face the risk of over-optimizing protocols and thereby hamper the single-protocol optimization for arbitrary LHZ instances.

B.3 Fixed annealing times

While typical values for qubit coupling are on the order of $10-100$MHz and coherence times can be as low as tens of nanoseconds, coherence times of around 1μs with a coupling strength of $|J|= 1$GHz has been reportedly achieved [96, 97]. A dimensionless annealing time as a product of time and energy scale is estimated to span the ranges of $T \in [1, 10, 100, 1000]$, which is comparable to the annealing times found in the simulations, cf. Table 10.1. Results are shown in Fig. B.1.

Naturally, a small $T = 1$ leads to poor results in terms of ground state fidelity of at most 0.1. For $T = 100$ most of the instances even from the first group are above the 0.9 mark, and for $T = 1000$ the lowest ground state fidelity is still above 0.975. The most interesting case we find for $T = 10$. Here, the cross-section of fidelities span values from just below 0.2 to almost 1.0 and can well be used to gauge the hardness of a given problem. In this case, the fidelity gives information of potential groups with a fixed annealing time. Yet, one is advised to be careful, since for example a ground state value of ~ 0.7 can be found in each group. It is therefore useful as an additional cross-check to either as a first educated guess for a group in which the problem is likely to be found — or as an approval of such a guess based on different techniques, such as the response to a given, pre-optimized schedule s_i.

B.4 Optimized protocols from annealing experiments

Minimum gaps are not readily available in a real hardware environment, which means that the strategy proposed can not be applied directly. However, as proof of concept the work shows that in principle finding optimized protocols is possible that work well for a large class

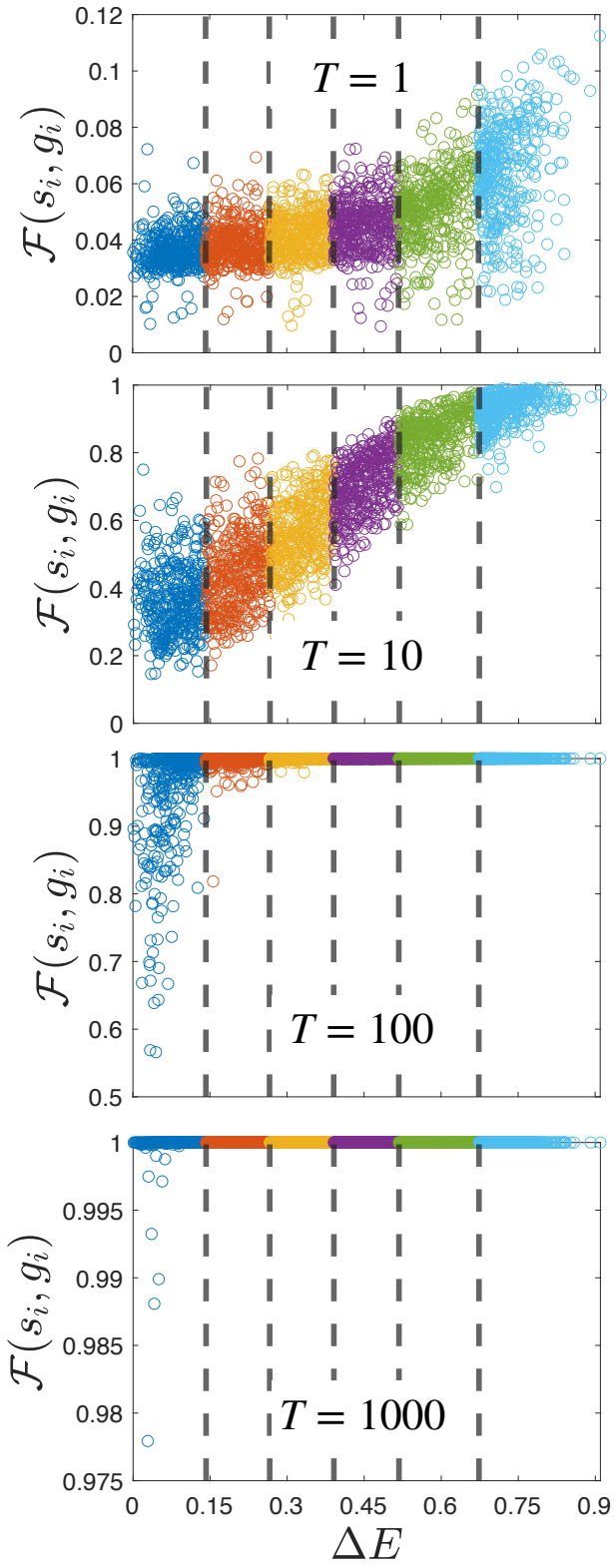

Figure B.1: Single-instance fidelities $\mathcal{F}(s_i, g_i)$ from optimization of the individual schedules for fixed annealing times $T \in [1, 10, 100, 1000]$ in accordance with typical coherence times of annealers.

of programmable LHZ problems. The following method not only can be readily applied on annealers. It also alleviates the problem of guessing the optimal number of groups as well as the optimal number of instances within these groups as these quantities are output as byproducts when executing the method. Most notably, a separative parameter (in our case the minimum energy gap) is not required as well.

The first step is to define two threshold probabilities that proxy ground state fidelities, e. g. $\mathcal{F}_- \equiv 0.66$ and $\mathcal{F}_+ \equiv 0.99$. Next, we sample a sufficiently large number of LHZ instances and draw from this sample the first instance to perform an energy optimization. Again, the annealing time needs to be varied until with large probability $\geq \mathcal{F}_+$ the minimum energy state of a final Hamiltonian is reached. Step two is to draw the second instance and apply the previously found protocol with corresponding annealing time. If we do not find with lower bound probability $\geq \mathcal{F}_-$ the minimum energy state, a single-protocol optimization is again performed until with probability $\geq \mathcal{F}_+$ we find the minimum energy state. In that case, we would have two schedules to be applied to the successive problem instances being drawn. Else, we simply draw the next instance.

This scheme is repeated until the number of protocols with corresponding annealing times saturates. As energy landscapes become increasingly complex with larger systems, diabatic evolution may become unique for each individual instance. The sample size and number of protocols are then difficult to anticipate — in the worst case the number of protocols scales linearly in the number of instances.

B.5 Visual overview

We provide the reader with the overview on the course of action taken to achieve average group-specific fidelities of $\overline{\mathcal{F}}_{g_i} \geq 0.9$ in Fig. B.2.

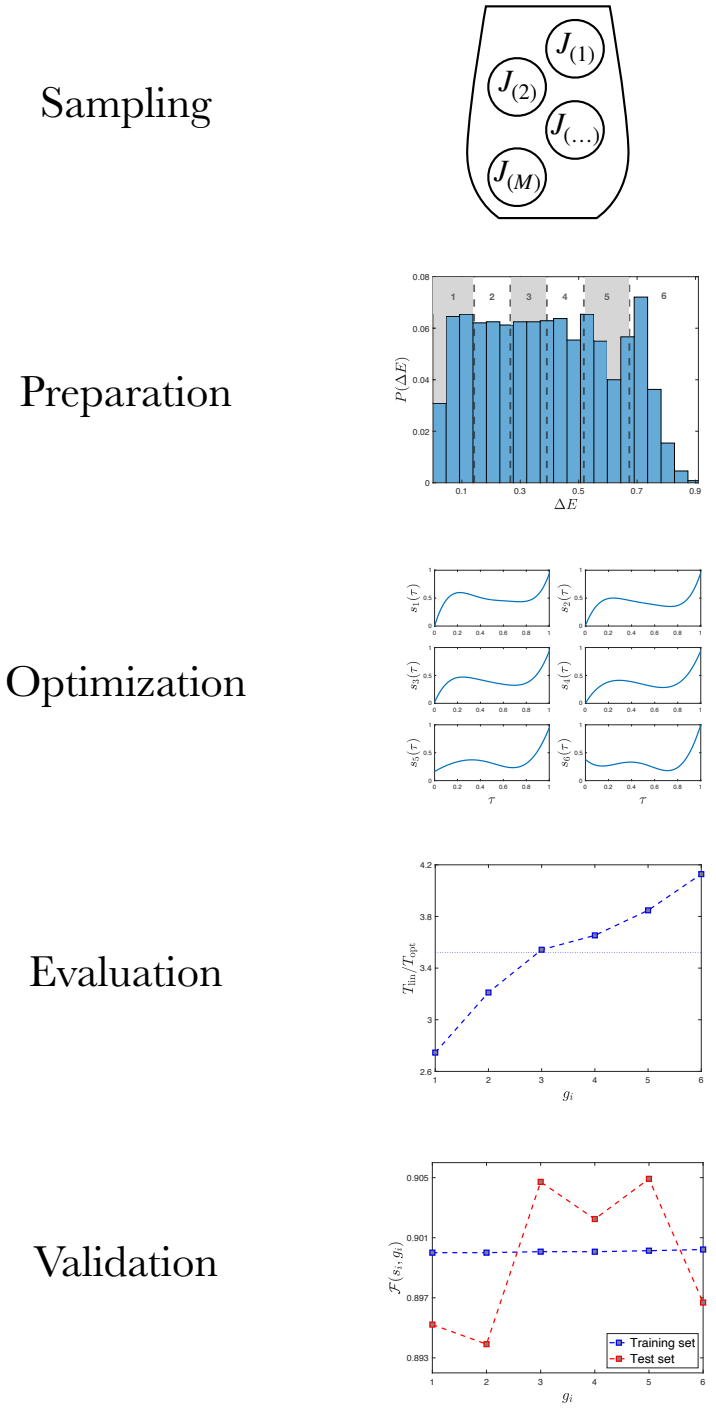

Figure B.2: Full process of finding effective schedules that lead to average group-specific fidelities of $\overline{\mathcal{F}}_{g_i} \geq 0.9$. *Sampling:* We sample $|M| = 4 \cdot 10^4$ problem instances constituted by their interaction matrices J. *Preparation:* Instances i from the large sample are ordered according to the amplitude of the minimum gaps $\Delta E_i < \Delta E_{i+1}$ and assigned to groups g_j, $j = 1, \cdots, 6$, that are comprised of 400 instances each. *Optimization:* Effective schedules are found by fidelity optimizations. *Evaluation:* Effective schedules are tested against linear ramps. An average reduction of factor ~3.5 in annealing time is achieved. *Validation:* Effective schedules are tested on a different sample. Similarity in fidelities indicates robustness of the schedules.